Integrated Master in Chemical Engineering

Carbon Dioxide Separation from Industrial Streams

Master's Dissertation

by

Rute Agostinha Gomes Seabra

Developed for the Dissertation course unit at:

LSRE - Laboratory of Separation and Reaction Engineering

SRE CM *ASSOCIATE LABORATORY*
LABORATORY OF SEPARATION AND REACTION ENGINEERING
LABORATORY OF CATALYSIS AND MATERIALS

Supervisor: **Doutora Ana Mafalda Ribeiro**

Supervisor: **Doutor Alexandre Ferreira**

U.PORTO
FEUP FACULDADE DE ENGENHARIA
UNIVERSIDADE DO PORTO

Chemical Engineering Department

July 2017

Acknowledgments

Nesta secção encontram-se notas de agradecimento a pessoas que contribuíram para a realização desta tarefa que começou muito antes da faculdade e que depende de muito mais que capacidade.

Começo por ti meu irmão, por me teres apoiado a todos os níveis e acreditares em mim. Obrigada por muitas vezes me teres citado Sun Tzu dizendo que *«Every battle is won before it's ever fought»,* para ter confiança e ir à luta!

Agradeço aos meus pais que sempre me deram tudo o que precisei e lutaram para eu ter as oportunidades que eles não tiveram. Obrigada não chega para descrever o tamanho da gratidão que tenho por aqueles que me deram vida e ajudam a crescer.

Agradeço à minha madrinha, exemplo de persistência, por todo o apoio e por ter exigido de mim responsabilidade e mérito desde o momento em que aprendi a segurar um lápis.

Ao meu amigo Ângelo por não demonstrar a menor dúvida de que eu vou conseguir tudo o que me propuser a fazer e que dentro de todas as peripécias e obstáculos, tudo se resolve, tudo se aprende e tudo se faz. Às minhas amigas que me acompanharam ao longo desta aprendizagem e que partilham comigo histórias que levamos para a vida. É quando a exigência é grande e o esforço e o cansaço atingem o máximo que damos mais valor àqueles que tornam a nossa vida mais feliz. Obrigada!

Agradeço ao Luís Carlos Matos por todos os ensinamentos e sobretudo amizade!

Todos os meus professores foram importantes, desde a primária à faculdade, desde os que ensinavam de forma exemplar aos que incentivavam o ensino autónomo. Contudo e desta casa destaco aqueles que me fizeram ver mais além e aos quais devo o gosto por aquilo que tenho feito e ao que farei: os meus orientadores Dra. Ana Mafalda Ribeiro e Dr. Alexandre Ferreira por todo o conhecimento, acompanhamento, dedicação e tempo, e aos professores José Miguel Loureiro, Adélio Mendes, João Campos, Fernando Martins, Romualdo Salcedo e Madalena Dias por representarem para mim exemplos a seguir.

Agradeço ao professor Alírio Rodrigues pela disponibilização das instalações para a realização da tese e ao LSRE pela oportunidade de desenvolvimento desta dissertação.

Finalmente, agradeço-te a ti, José Pedro Alves, por todo o amor, coragem, força e perseverança que partilhaste comigo e me fizeste aperceber que tinha. Obrigada por acreditares sempre em mim e seres a razão quando a emoção fala mais alto.

Este trabalho foi financiado por: Projeto POCI-01-0145-FEDER-006984 - Laboratório Associado LSRE-LCM - financiado pelo Fundo Europeu de Desenvolvimento Regional (FEDER), através do COMPETE2020 – Programa Operacional Competitividade e Internacionalização (POCI) e por fundos nacionais através da Fundação para a Ciência e a Tecnologia I.P.

FCT
Fundação para a Ciência e a Tecnologia

COMPETE
2020

PORTUGAL
2020

UNIÃO EUROPEIA
Fundo Europeu
de Desenvolvimento Regional

Resumo

De forma a limitar as emissões de CO_2 e a diminuir o seu conteúdo no gás natural, tecnologias de captura e armazenamento de dióxido de carbono tem sido desenvolvidas. Separação e purificação de misturas gasosas através de fenómenos de adsorção tem sido valorizadas pelas indústrias química e petroquímica devido ao baixo consumo energético e ao baixo investimento de capital exigido. A necessidade de capacidade de adsorção adequada restringe a escolha de adsorventes para processos de separação. Neste trabalho, zeolitos 4A e 13X serão estudados com o objetivo de avaliar as capacidades adsortivas para a captura de dióxido de carbono de correntes de gases de escape e tratamento do gás natural.

Em primeiro lugar, de forma a caracterizar os materiais e, por consequência obter informação útil para o equilíbrio de adsorção e propriedades cinéticas, propriedades como isotérmicas de adsorção de N_2 e de CO_2 a 77 K e 273 K, respetivamente, intrusão de mercúrio, microscopia eletrónica de varrimento, raios X de energia dispersiva e difração de raios X foram estudadas.

Isotérmicas de adsorção de gases puros (CO_2, CH_4 e N_2) foram determinadas a 303, 343 e 373 K. A isotérmica de *Dual site Langmuir* foi usada para ajustar os resultados experimentais da adsorção do CO_2 e a *One site Langmuir* para a adsorção do CH_4 e N_2. A capacidade de adsorção e o calor de adsorção para cada gás foi determinado. Dióxido de carbono foi o adsorvente com melhor afinidade tanto nos zeólitos 4A como nos 13X tendo atingido a maior capacidade de adsorção nos zeólitos 13X. Azoto foi o gás menos adsorvido em ambos os zeólitos tendo atingido a menor capacidade de adsorção nos zeólitos 4A. O calor isotérico de adsorção foi calculado segundo a equação de *Clausius-Clapeyron* e posteriormente comparado com valores descritos na literatura.

Estudos cinéticos foram efetuados a 308, 323, 343 e 373 K através da técnica de ZLC com análise da resposta a tempos longos e do modelo completo. Os resultados evidenciaram que o controlo de difusão se encontra nos microporos na adsorção de CO_2 nos zeólitos 4A BFK 2.5 – 5.0 mm, 4A BFK 1.6 – 2.5 mm, in 13X BFK 1.2 – 2.0 mm e 13X BFK 6x8 mesh, e na adsorção de CO_2 e CH_4 no zeólito 4A BFK 1.6 – 2.5 mm HSD. Em termos de difusão, o azoto apresenta o coeficiente de difusividade mais elevado e o dióxido de carbono o mais baixo.

Palavras Chave: adsorção, zeólito 4A, zeolito 13X, isotérmicas de adsorção, *zero length column*

Abstract

In order to limit the CO_2 emissions and to decrease its content in natural gas, technologies to capture and storage carbon dioxide have been developed. Separation and purification of gas mixtures by adsorption has gain interest to chemical and petrochemical industries due to the low energy requirements and low capital investment costs. The requirement for adequate adsorption capacity restricts the choice of adsorbents for practical separation processes. In this study, Zeolites 4A and 13X will be tested with the purpose of evaluating the adsorption properties for carbon dioxide capture from flue gas streams, and sweetening of natural gas.

First, to characterize the materials, and therefore obtain useful information to adsorption equilibrium and adsorption kinetics properties, several properties as the N_2 and CO_2 physisorption isotherms measured at 77 K and 273 K, respectively, mercury intrusion, Scanning Electron Micrograph (SEM), Energy Dispersive X-ray and X-ray Diffraction (XRD) were performed.

Adsorption isotherms of pure gases (CO_2, CH_4 and N_2) were determined at 303, 343 and 373 K. The Dual site Langmuir was used to fit the experimental results for adsorption of CO_2 and One site Langmuir for the adsorption of CH_4 and N_2. The adsorption capacity and the heat of adsorption for each gas was determined. The carbon dioxide was the adsorbate with best affinity for both 4A and 13X reaching greater adsorption capacity in 13X. The least adsorbed was nitrogen in both 4A and 13X reaching smallest adorption capacity in 4A. The isosteric heats of adsorption were calculated by the Clausius-Clapeyron equation and additionally compared with literature values.

The kinetics studies were performed at 308, 323, 343 and 373 K with the zero length technique analysing the long time response and the complete model. The results showed that the micropore diffusion is the controlling mechanism in the adsorption of CO_2 in 4A BFK 2.5 – 5.0 mm, 4A BFK 1.6 – 2.5 mm, in 13X BFK 1.2 – 2.0 mm and 13X BFK 6x8 mesh and in adsorption of CO_2 and CH_4 in 4A BFK 1.6 – 2.5 mm HSD. In terms of diffusion the N_2 has the highest diffusion coefficient and CO_2 the lowest.

Keywords: adsorption, zeolite 4A, zeolite 13X, adsorption equilibrium isotherm, zero length column

Declaração

Declara, sob compromisso de honra, que este trabalho é original e que todas as contribuições não originais foram devidamente referenciadas com identificação da fonte.

Assinar e datar

Rute Agostinha Gomes Seabra

3/7/2017

Table of Contents

1 Introduction 1

1.1 Motivation and Relevance 1

1.2 Outline 2

2 State of the art 3

2.1 Zeolites 3

2.2 Zero Length Column 4

3 Material and Methods 5

3.1 Materials used 5

3.1.1 Adsorbent 5

3.1.2 Gases 6

3.2 Methods 6

3.2.1 Adsorption equilibrium 6

3.2.2 Adsorption equilibrium experimental 7

3.2.3 Zero Length Column 9

4 Results and Discussion 13

4.1 Zeolites characterization 13

4.1.1 Zeolite 4A 13

4.1.2 Zeolite 13X 16

4.2 Adsorption equilibrium isotherms 19

4.3 Isosteric heat of adsorption 22

4.4 Adsorption kinetics 24

4.4.1 4A BFK 2.5-5.0 mm 25

4.4.2 4A BFK 1.6-2.5 mm 27

4.4.3 4A BFK 1.6-2.5 mm HSD 29

4.4.4 4A BFK Zeolites – Determination of the diffusional controlling mechanism and the difusivity coefficients 31

4.4.5 13X BFK 1.2-2.0 mm 36

4.4.6 13X BFK 6x8 mesh 38

4.4.7 13X BFK Zeolites – Determination of the diffusional controlling mechanism and the difusivity coefficients 40

5 Conclusions 45

6 Evaluation of the work done 47

6.1 Accomplished objectives 47

6.2 Limitations and future work 47

6.3 Final appreciation 47

References 49

Appendix 1 Helium pycnometries 51

Appendix 2 Liquid densities 53

Appendix 3 SEM 55

Appendix 4 Isotherms of 4A and 13X zeolites 61

Isotherms of zeolites 4A BFK 1.6-2.5 mm HSD, 4A BFK 2.5-5.0 mm 61

Isotherms of 13X BFK 6x8 mesh and 13X BFK 1.2 – 2.0 mm 62

Isotherms of CO_2, CH_4 and N_2 at 303, 343 and 373 K in 4A and 13X zeolite samples in terms of amount adsorved per volume of adsorbent. 64

Appendix 5 Calibration of the volumetric flow rate of the Gas Chromatographer 67

Appendix 6 ZLC columns 69

Appendix 7 ZLC results 71

Experimental results in each ZLC column 71

Comparison of experiments with the same flow rate and temperature but different zeolite 76

Appendix 8 Henry constant determination 81

List of Figures

Figure 1- Zero length column. 4

Figure 2- Zeolite: a) 4A BFK 2.5-5.0 mm; b) 4A BFK 1.6-2.5 mm; c) 4A BFK HSD 1.6-2.5 mm; d) 13X BFK 1.2-2.0 mm; e) 13X BFK 6x8 mesh. 5

Figure 3- (a) Crystal structure of type A zeolite. (b) Crystal structure of type X zeolite [17]. Silicon atoms are teal, red atoms are oxygen and the orange spheres fill the voids of the sodalite cages.......6

Figure 4- a) Magnetic suspension microbalance (Rubotherm, Germany); b) Acquisition system of the magnetic microbalance. 7

Figure 5- Schematic diagram of the experimental set-up for adsorption equilibrium measurements. ...8

Figure 6- Varian gas chromatography (Varian, Holland). 9

Figure 7- Zero length column experimental set-up. 10

Figure 8- SEM images of zeolites: a) 4A BFK 2.5-5.0 mm, b) 4A BFK 1.6-2.5 mm, c) 4A BFK HSD 1.6-2.5 mm. 13

Figure 9- Pore size distribution by mercury intrusion of zeolite 4A. 13

Figure 10- Adsorption isotherms in Zeolites 4A of Nitrogen at 77 K (a) and of Carbon Dioxide at 273 K (b). 14

Figure 11- X-Ray diffraction data of the 4A zeolite samples. 15

Figure 12- SEM images of zeolites: a) 13X BFK 1.2-2.0 mm, b) 13X BFK 6x8 mesh (2.36-3.35 mm). 16

Figure 13- Pore size distribution by mercury intrusion of zeolites: a) 13X BFK 1.2 - 2.0 mm, b) 13X BFK 6x8 mesh (2.36-3.35 mm). 16

Figure 14- Adsorption isotherms in Zeolite 13X BFK of Nitrogen at 77 K (a) and of Carbon Dioxide at 273 K (b). 17

Figure 15- X-Ray diffraction data of the 13X zeolite samples. 18

Figure 16- Amount of a) CO_2, b) CH_4 and c) N_2 adsorbed on 4A 1.6-2.5 mm zeolite: experimental points (closed adsorption, open desorption) at 303, 343, 373 K and Dual site Langmuir fiiting for CO_2 and One site Langmuir for CH_4 and N_2 (lines). 19

Figure 17- Comparison between the adsorption capacities per volume of adsorbent of CO_2 in 4A zeolites at 303 K. 20

Figure 18- Adsorption equilibrium isoterms of N_2 on 13X BFK 6x8 mesh zeolite: experimental points (closed adsorption, open desorption) at 303, 343, 373 K and One site Langmuir (lines). 21

Figure 19- Single-component isosteric heats of adsorption on 4A BFK 1.6-2.5 mm for CO_2, CH_4 and N_2 as function of the amount adsorbed in the temperature range of 303 – 373 K; Lines are the values obtained through the Langmuir fitting. 22

Figure 20- Single-component isosteric heat of adsorption on 13X BFK 6x8 mesh for N_2 as function of the amount adsorbed in the temperature range of 303 – 373 K; Lines are the values obtained through the Langmuir fitting. 23

Figure 21- ZLC curves for CO_2 in 4A BFK 2.5 – 5.0 mm zeolite at 308 - 373 K. Solid lines in (a) represent the results using the long time response and (b) the complete ZLC model results. 25

Figure 22- ZLC curves for CH_4 in 4A BFK 2.5 – 5.0 mm zeolite at 308, 323, 343 and 373 K. Solid lines in (a) represent the results using the long time response and (b) the complete ZLC model results. 26

Figure 23- ZLC curves for CO_2 in 4A BFK 1.6 – 2.5 mm zeolite at 308, 323, 343 and 373 K. Solid lines in (a) represent the results using the long time response and (b) the complete ZLC model results. 27

Figure 24- ZLC curves for CH_4 in 4A BFK 1.6 – 2.5 mm zeolite at 308, 323, 343 and 373 K. solid lines in (a) represent the results using the long time response and (b) the complete ZLC model results. 28

Figure 25- ZLC curves for CO_2 in 4A BFK 1.6 – 2.5 mm HSD zeolite at 308, 323, 343 and 373 K. Solid lines in (a) represent the results using the long time response and (b) the complete ZLC model results. 29

Figure 26- ZLC curves for CH_4 in 4A BFK 1.6 – 2.5 mm HSD zeolite at 308, 323, 343 and 373 K. Solid lines in (a) represent the results using the long time response and (b) the complete ZLC model results. 30

Figure 27- Dependence of the apparent diffusivity coeficient for CO_2 in 4A zeolites with temperature. 32

Figure 28- Dependency of the pore diffusivity in 4A BFK zeolites with $T3/2$. 33

Figure 29- Dependence of the apparent diffusivity coeficient for CH_4 in 4A zeolites with temperature. 34

Figure 30- Comparison of the blank test with the results of 4A zeolites for: a) 308 K, b) 343 K and c) 373 K and a flow rate of 5.83×10^{-7} m^3 s^{-1} in PTN conditions. 35

Figure 31- ZLC curves for CO_2 in 13X BFK 1.2 – 2.0 mm zeolite at 308, 323, 343 and 373 K. Solid lines in (a) represent the results using the long time response and (b) the complete ZLC model results. 36

Figure 32- ZLC curves for CH_4 in 13X BFK 1.2 – 2.0 mm zeolite at 308, 323, 343 and 373 K. Solid lines in (a) represent the results using the long time response and (b) the complete ZLC model results. 37

Figure 33- ZLC curves for CO_2 in 13X BFK 6x8 mesh zeolite at 308, 323, 343 and 373 K. Solid lines in (a) represent the results using the long time response and (b) the complete ZLC model results. 38

Figure 34- ZLC curves for CH_4 in 13X BFK 6x8 mesh zeolite at 308, 323, 343 and 373 K. Solid lines in (a) represent the results using the long time response and (b) the complete ZLC model results. 39

Figure 35- Dependence of the apparent diffusivity coeficient of CO_2 in 13X zeolites with temperature. 40

Figure 36- Dependency of the pore diffusivity in 13X BFK zeolites with $T3/2$ 41

Figure 37- Dependence of the apparent diffusivity coeficient for adsorption of CH_4 in 13X zeolites with temperature. 42

Figure 38- Dependency of the pore diffusivity in 13X BFK zeolites with $T3/2$.............................. 43

Figure 39- Comparison of the blank test with 13X zeolites for: a) 308 K, b) 343 K and c) 373 K and a 5.83 x 10^{-7} m^3 s^{-1} in PTN conditions. 44

List of Tables

Table 1- Total intrusion volume, surface area, average pore diameter, apparent and solid density obtained from mercury intrusion and solid density obtained form helium picnometry in the 4A zeolites. 14

Table 2- Surface area of zeolite 4A BFK 2.5-5.0 mm obtained from physisorption isotherms of Nitrogen at 77 K and Carbon Dioxide at 273 K. 15

Table 3- Total intrusion volume, surface area, average pore diameter, apparent and solid density obtained from mercury intrusion and solid density obtained form helium picnometry in the 13X zeolites. 17

Table 4- Surface area of zeolite 13X BFK of Nitrogen 77 K and Carbon Dioxide at 273 K. 17

Table 5- Fitting parameters of the Langmuir model for CO_2, CH_4 and N_2 adsorption equilibrium on 4A BFK 1.6-2.5 mm. 20

Table 6- Fitting parameters of the Langmuir model for N_2 adsorption equilibrium on 13X BFK 6x8 mesh. 21

Table 7- Flow rate of the experiments at different temperatures (at the experimental conditions). . 24

Table 8- Experimental conditions for the ZLC runs with 4A BFK 2.5 – 5.0 mm. 25

Table 9- Long time response and complete ZLC model parameters for CO_2 in 4A BFK 2.5 - 5.0 mm zeolite at 308, 323, 343 and 373 K. 25

Table 10- Long time response and the complete ZLC model parameters for CH_4 in 4A BFK 2.5 - 5.0 mm zeolite at 308, 323, 343 and 373 K. 26

Table 11- Experimental conditions for the ZLC runs with 4A BFK 1.6 – 2.5 mm. 27

Table 12- Long time response and the complete ZLC model for CO_2 in 4A BFK 1.6 – 2.5 mm zeolite at 303, 323, 343 and 373 K. 27

Table 13- Long time response and the complete ZLC model parameters for CH_4 in 4A BFK 1.6 – 2.5 mm zeolite at 308, 323, 343 and 373 K. 28

Table 14- Experimental conditions for the ZLC runs with 4A BFK 1.6 – 2.5 mm HSD. 29

Table 15- Long time response and the complete ZLC model parameters for CO_2 in 4A BFK 1.6 – 2.5 mm HSD zeolite at 303, 323, 343 and 373 K. 29

Table 16- Long time response and the complete ZLC model parameters for CH_4 in 4A BFK 1.6 – 2.5 mm HSD zeolite at 308, 323, 343 and 373 K. 30

Table 17- Diffusivity coeficient for CO_2 in zeolites: 4A BFK 2.5 - 5.0 mm, 4A BFK 1.6 – 2.5 mm and 4A BFK 1.6 – 2.5 mm HSD at different temperatures. 31

Table 18- Molecular and Knudsen diffusivity coefficients for the CO_2/He mixture. 32

Table 19- Henry's law constant and equilibrium constant for 4A zeolites. 33

Table 20- Diffusivity coeficient for CH_4 in zeolites: 4A BFK 2.5 – 5.0 mm, 4A BFK 1.6 – 2.5 mm and 4A BFK 1.6 – 2.5 mm HSD at different temperatures. 33

Table 21- Crystal diffusivity in 4A zeolites of CO_2 and CH_4. 35

Table 22- Experimental conditions for the ZLC runs with 13X BFK 1.2 – 2.0 mm. 36

Table 23- Long time response and the complete ZLC model parameters for CO_2 adsorption in 13X BFK 1.2 – 2.0 mm zeolite at 308, 323, 343 and 373 K. 36

Table 24- Long time response and the complete ZLC model parameters for CH_4 adsorption in 13X BFK 1.2 – 2.0 mm zeolite at 308, 323, 343 and 373 K. 37

Table 25- Experimental conditions for the ZLC runs with 13X BFK 6x8 mesh. 38

Table 26- Long time response and the complete ZLC model parameters for CO_2 adsorption in 13X BFK 6x8 mesh zeolite at 308, 323, 343 and 373 K. 39

Table 27- Long time response and the complete ZLC model parameters for CH_4 adsorption in 13X BFK 6x8 mesh zeolite at 308, 323, 343 and 373 K. 39

Table 28- Diffusivity coeficient for CO_2 in zeolites: 13X BFK 1.2 – 2.0 mm, 13X BFK 6x8 mesh at different temperatures. 40

Table 29- Molecular and Knudsen diffusivity coefficients for the CO_2/He mixture. 40

Table 30- Henry's law constant and equilibrium constant for 13X zeolites. 41

Table 31- Diffusivity coeficient for adsorption of CH_4 in zeolites: 13X BFK 1.2 – 2.0 mm, 13X BFK 6x8 mesh at different temperatures. 42

Table 32- Molecular and Knudsen diffusivity coefficients for the CH_4/He mixture......................... 42

Table 33- Henry's law constant and equilibrium constant for 13X zeolites. 43

Notation and Glossary

C	instantaneous concentration	mol m^{-3}
C_0	initial gas phase concentration	mol m^{-3}
D_{ap}	apparent diffusivity	cm^2 s^{-1}
D_c	crystal diffusivity	cm^2 s^{-1}
D_c^0	limiting diffusivity at infinite temperature	cm^2 s^{-1}
D_{ij}	binary molecular diffusivity of component i and j	cm^2 s^{-1}
D_m	molecular diffusivity	m^2 s^{-1}
D_p	pore diffusivity	cm^2 s^{-1}
D_K	Knudsen diffusivity	m^2 s^{-1}
E_a	activation energy of micropore/crystal diffusivity	kJ mol^{-1}
H	Henry's constant	mol kg^{-1} Pa^{-1}
J_0, J_1	Bessel functions	
K_{eq}	dimensionless equilibrium constant	
K_i	adsorption constant or Langmuir constant of component i	bar^{-1}
K_i^0	adsorption constant at infinite temperature	bar^{-1}
l	representative spatial dimension of the pellet	m
L	zero length column parameter	
m_s	adsorbent mass	kg
M_w	adsorbate molecular weight	kg mol^{-1}
n	ZLC geometrical factor of the adsorbent	
P	pressure	bar
q_i	adsorbed amount of component i	mol kg^{-1}
$q_{m,i}$	maximum adsorption capacity of component i in the adsorbent	mol kg^{-1}
Q_p	purge flowrate	m^3 s^{-1}
r_c	crystal representative spatial dimension	m
R_g	universal gas constant	J mol^{-1} K^{-1}
r_p	pore spatial dimension	m
T	temperature	K
V_c	volume of the permanent magnet, of the sample basket and the glass wool used to hold the sample	m^3
V_s	volume of the solid adsorbent	m^3
y_i	molar fraction of component i	

Greek letters

β_j	ZLC roots dependent of the adsorbent shape	
$(-\Delta H)$	heat of adsorption	kJ mol^{-1}
$(-\Delta H)_i$	isosteric heat of adsorption of component i	kJ mol^{-1}
Δm	difference in weight between two measurements	kg
e	bed porosity	
e_p	porosity of the pellet	
ρ_{ap}	apparent density	kg m^{-3}
ρ_g	density of the gas phase at the measuring conditions (T,P)	kg m^{-3}
ρ_L	density of the adsorbed liquid phase	kg m^{-3}
$\rho_{s,Hg}$	density of the solid measured by mercury intrusion	kg m^{-3}
$\rho_{s,He}$	adsorbent density measured by helium pycnometry	kg m^{-3}
σ	collision molecular diameter	
τ_p	tortuosity	
Ω_{Dij}	dimensionless collision integral of the diffusivity	

List of Acronyms

BFK	Binder-Free molecular sieves
EDS	Energy Dispersive X-Ray
FID	Flame Ionization Detector
GC	Gas Chromatographer
MFC	Mass Flow Controller
SEM	Scanning Electron Micrograph
PT	Pressure Transducer
TCD	Thermal Condutivity Detector
TT	Temperature Transducer
XRD	X-Ray Diffraction
ZLC	Zero Length Column

1 Introduction

1.1 Motivation and Relevance

Due to the increase of world population, industrialization and technology advancement the use of fossil fuel has released considerable amounts of greenhouse gases such as carbon dioxide which contributes up to 60% of the global warming effects [1]. In order to limit the CO_2 emissions and to decrease its content in natural gas, which is an energy source with expected consumption growth of 50% over the next 20 years [2], technologies to capture and storage carbon dioxide have been developed.

The existing techniques for CO_2 separation from gas streams include advanced technologies such as wet scrubber, membranes, cryogenics, pressure and temperature swing adsorption [3]. Separation and purification of gas mixtures by adsorption has gain interest to chemical and petrochemical industries due to the low energy requirements and low capital investment costs [2].

The requirement for adequate adsorption capacity restricts the choice of adsorbents for practical separation processes. Zeolites, porous crystalline aluminosilicates, have different frameworks which allows the tailoring of adsorptive properties to achieve an aimed selectivity. In this study, Zeolites 4A and 13X will be tested with the purpose of evaluating the adsorption properties for carbon dioxide capture from flue gas streams, and sweetening of natural gas.

In order to study the adsorbents, adsorption equilibrium and kinetic measurements ought to be made. Traditionally, these studies have been carried out by straightforward and accurate gravimetric or volumetric techniques. However, for kinetic measurements these may not be the most adequate methods [4]. As different transport mechanisms may occur in adsorbents, the interpretation of kinetic data can be difficult, therefore, in 1988, Eic and Ruthven, with the aim of measuring the micropore diffusion of zeolite crystals, developed the zero length column (ZLC) [5]. This chromatographic technique has been widely used for diffusivity measurements in zeolites and for measuring the diffusion in bimodal porous materials [6]. This method uses a small amount of adsorbent and low adsorbate concentrations.

To test the adsorbents, adsorption equilibrium data of CO_2, CH_4 and N_2 was measured in a gravimetric suspension balance and adsorption kinetics of the same pure gases were measured by the zero length column technique.

1.2 Outline

The present work is divided in five chapters.

In Chapter 1 the relevance of the study of carbon dioxide separation from industrial streams is described. In order to perform such separation, the selected sieves are introduced in Chapter 2, with a brief history, description of the materials and some applications. Along with zeolites, in Chapter 2 is presented the zero length column technique used to perform kinetic studies, that has been developed by Brandani and by Silva and Rodrigues.

Chapter 3 describes the materials and methods. The theory and matematical aproach behind the adsorption equilibrium and the kinetics studied are presented and the experimental set-ups and procedures described.

Chapter 4 consists in experimental results which starts with the zeolites characterization, shows the adsorption equilibrium isotherms of each adsorbent, the diffusional coefficient and the diffusion controlling mechanism determination.

Chapter 5 presents the conclusions of this work.

2 State of the art

2.1 Zeolites

The history of zeolites began in 1756 when Cronstedt, a mineralogist, discovered the first zeolite mineral, stilbite. He called it a ''zeolite'' which derived from two Greek words, *zeo* (to boil) and *lithos* (a stone). In 1940s, Milton developed a method to synthesize zeolites through hydrothermal crystallization of reactive alkali metal aluminosilicates gels at high pH and low temperatures and pressures. Since the late 1940s the Milton's concept has been followed by several addictions and modifications [7].

Although there is no systematic nomenclature, the early synthetic materials discovered by Milton, Breck and coworkers at Union Carbide used the modern Latin alphabet, such as zeolites A, B, X, Y, to name the materials. Nowadays, the International Zeolite Association publishes and frequently updates the Atlas of Zeolite Structure Types where it assigns a three letter code to be used for a known framework topology irrespective of composition [7].

These molecular sieves are crystalline inorganic polymers based on an infinitely extending three-dimensional framework, four-connected framework of AlO_4 and SiO_4 tetrahedra linked by the oxygen ions. The framework bears a negative charge which is neutralised by an extra-framework cation from elements of group I or II such as sodium, potassium and calcium. The structure of the framework allows intracrystalline channels to be occupied by cations, which are mobile and may undergo ion exchange, and by water molecules [7]. Commercial molecular sieve zeolite crystals have typically 1 to 10 µm, and in order to prepare a practically useful adsorbent these crystals are converted into shaped materials, such as pellets or beads [5].

In the past decades, applications of zeolites showed a particularly growth in petroleum refining with emphasis on resid cracking and octane enhancement. The use of these molecular sieves in detergents as a replacement for phosphates became the single largest volume use for synthetic zeolites worldwide. In terms of ion exchange products, zeolites were used widely in nuclear waste clean-up after the Three Mile Island and Chernobyl nuclear accidents. Applications in adsorption and separation have been having a major growth in pressure swing adsorption processes such as in purification of hydrogen [8], purifications of biogas [9], CO_2 sequestration [10] and propylene/propane separation [11], and more recently, application in removal of and recovery of volatile organic compounds [7].

2.2 Zero Length Column

The zero length column (ZLC) was introduced in 1988 by Eic and Ruthven with the objective of measuring diffusivities of hydrocarbons in zeolites. Prior to this invention, the Wicke-Kallenbach method was used to measure intracrystalline and macropore diffusivities, it depended on a steady-state measurement and it was not affected by finite heat transfer [12]. However, for micropore diffusivity calculation this method demanded a single crystal with regular large size, which was not feasible. Inverse chromatography was also an alternative that allowed a dynamic response of a packed column to a change in adsorbate concentration, with the disadvantage of being difficult to separate the effect of diffusion and axial dispersion by a single experiment [12].

The ZLC technique has the advantage of elimination of external mass and heat transfer resistances by the use of low adsorbate concentration, small amount of adsorbent sample and the use of high carrier flow rates during desorption.

In 1993, this study was extended to the measurement of diffusivities in pellets by Ruthven and Xu [13]. In 1996, a complete model which includes macropore and micropore diffusion in pellets applied to ZLC technique has been developed by Brandani [14], and by Silva and Rodrigues [15] who also suggested logarithms for data treatment.

Figure 1- Zero length column.

3 Material and Methods

3.1 Materials used

3.1.1 Adsorbent

The adsorbents studied were 4A BFK zeolites with two particle diameters 1.6 - 2.5 mm and 2.5 -5.0 mm and a 4A BFK zeolite denominated high density with 1.6 - 2.5 mm diameter range, and 13X BFK zeolite also with two particle diameters 1.2 - 2.0 mm and 6x8 mesh which corresponds to 2.36 - 3.35 mm, in form of granulates, provided by Köstrolith.

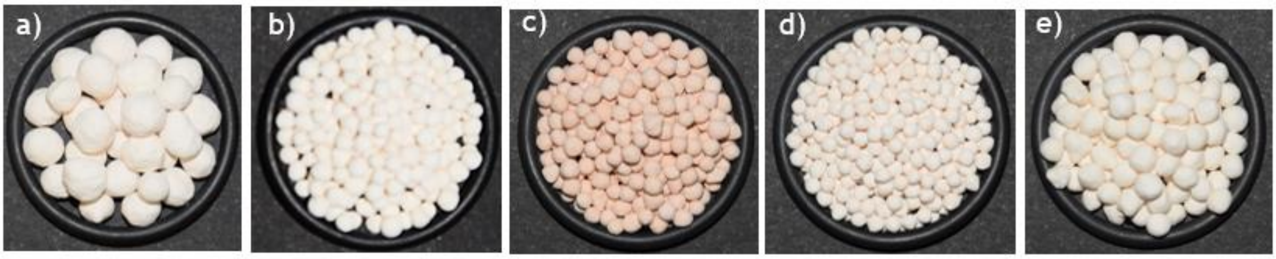

Figure 2- Zeolite: a) 4A BFK 2.5-5.0 mm; b) 4A BFK 1.6-2.5 mm; c) 4A BFK HSD 1.6-2.5 mm; d) 13X BFK 1.2-2.0 mm; e) 13X BFK 6x8 mesh.

All the studied adsorbents are classified as binder-free molecular sieves (*BFK*) as a result of a new synthesis pathway that has been developed to compensate the fact that in the synthesis of shaped LTA (A) and FAU (X) type zeolites is normally used 80-82 wt % of a zeolite powder and 20-18 wt % of binders that despite providing a specific shape and mechanical strength, reduces the adsorption capacity of the material. Therefore, it is expected that the tested molecular sieves have an adsorption capacity comparable to pure zeolites of the same structural types [16].

The structure of zeolite LTA (A) is shown in Figure 3 (a) and reveals eight cages located in the corners of a cube connected through four-membered oxygen rings. Each pseudo cell contains 24 tetrahedral units and since the Si/Al ratio in this zeolite is always close to 1.0 there are 12 univalent exchangeable cations per cell. As the tested zeolite is a 4A, there are 12 sodium cations per cage [12].

The structure of zeolite FAU (X) is also shown in Figure 3 (b) and the crystallographic unit cell consists of an array with eight cages containing a total of 192 tetrahedral units. The Si/Al ratio is within the range of 1-1.5 and the exchangeable univalent cations varies, being between 10-12 per cage [12].

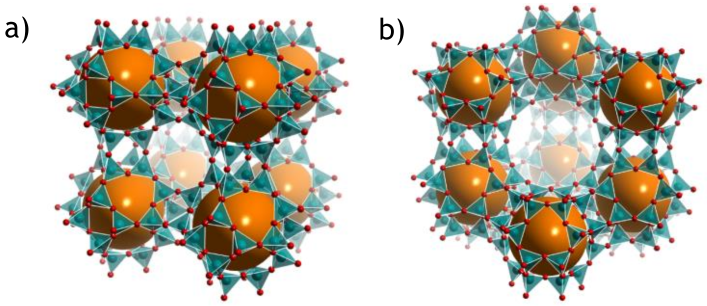

Figure 3- (a) Crystal structure of type A zeolite. (b) Crystal structure of type X zeolite [17]. Silicon atoms are teal, red atoms are oxygen and the orange spheres fill the voids of the sodalite cages

The materials were characterized by mercury porosimetry and nitrogen adsorption isotherms at 77 K as well as carbon dioxide adsorption isotherms at 273 K performed at Málaga University, scanning electron micrograph (SEM) at the *Centro de Materiais da Univerdade do Porto* (CEMUP) and X-ray Diffraction (XRD) was performed in *Universidade de Aveiro*.

3.1.2 Gases

The adsorption properties of carbon dioxide (CO_2), methane (CH_4) and nitrogen (N_2) in the different zeolite samples were determined using gases provided by Air Liquide with the following specifications: carbon dioxide N48, methane N35 and nitrogen N45, which means purity greater than 99.998, 99.95 and 99.995%, respectively.

For adsorbent activation and regeneration, it was used Helium (He) with 99.999% purity, also provided by Air liquid.

3.2 Methods

3.2.1 Adsorption equilibrium

For separation processes it is necessary to know the interactions between adsorbates (fluid) and the adsorbent (solid) since different bonds involve different energies. For processes where adsorption and desorption are involved, the main focus is in the reversibility achieved by a change of operating conditions as temperature or pressure. As a spontaneous phenomenon, adsorption equilibrium releases heat and despite being a dynamic process after a certain amount of time it achieves equilibrium state.

In 1918, Langmuir gave the first coherent theory of adsorption as a dynamic equilibrium with equal rates of adsorption and desorption. This model assumes that the surface is energetically homogeneous, that there’s no interaction between adsorbed molecules and that each site has the same probability of adsorbing, being able to accommodate only one molecule.

The Langmuir equation is:

$$q_i = q_{m,i} \frac{K_i P}{1+K_i P} \qquad \text{(Equation 1)}$$

where q_i is the adsorbed amount of the component i, $q_{m,i}$ is the maximum adsorption capacity of the adsorbent (only considering monolayer adsorption) of component i, K_i is the adsorption constant for component i and P is the pressure. The adsorption constant also known as the Langmuir constant is expressed by the Van´t Hoff equation:

$$K_i = K_i^0 e^{\left(-\frac{\Delta H}{R_g T}\right)} \qquad \text{(Equation 2)}$$

where K_i^0 is the adsorption constant at infinite temperature, $(-\Delta H)$ is the heat of adsorption on the homogeneous surface, R_g is the universal gas constant and T is the temperature of the system.

Under high values of pressure the term $K_i P \gg 1$ and so the Langmuir isotherm reduces to $q_i = q_{m,i}$, which means the capacity saturation of the adsorbent is complete. For low values of pressure the term $K_i P \ll 1$ reducing the equation to the linear isotherm: $\frac{q_i}{q_{m,i}} = K_i P$.

3.2.2 Adsorption equilibrium experimental

In order to measure the adsorption equilibrium isotherms of CO_2, CH_4 and N_2 a magnetic suspension microbalance (Rubotherm, Germany), with a precision of 0.01 mg, was used (Figure 4). The schematic diagram of the experimental set-up is shown in Figure 5. The balance is connected to a three port valve, a thermocouple for temperature monitoring, one pressure transducer to measure the pressure inside the cell and a vacuum pump used for sample activation and cell depressurization. To control the temperature, an electric resistence was used. The system control and data acquisition is done by a Rubotherm software.

Figure 4- a) Magnetic suspension microbalance (Rubotherm, Germany); b) Acquisition system of the magnetic microbalance.

The adsorbent sample is weighed and placed in a basket linked to a permanent magnet. The permanent magnet interacts with the electromagnet (magnetic suspension coupling) allowing the measurement of the weight variations inside the cell which is recorded in a computer. Before the experiments with the gases under study, the adsorbent was activated at 573 K under vacuum until no mass loss was observed. To achieve the activation temperature a heating rate of 1 K/min was used.

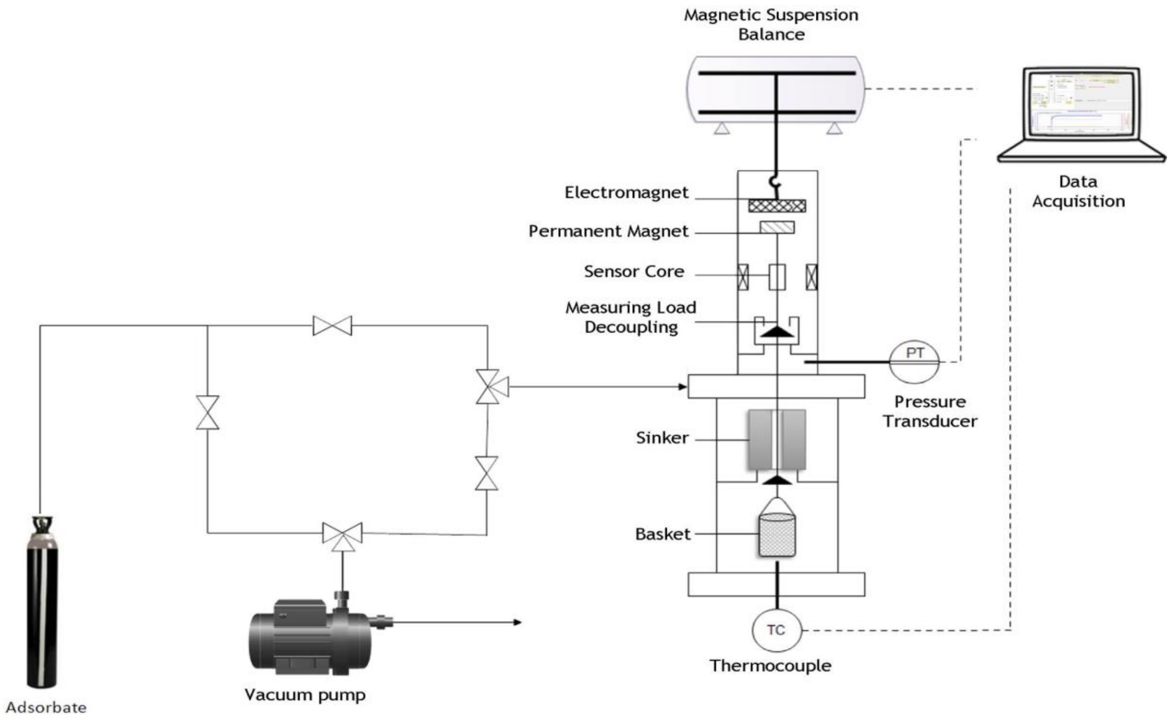

Figure 5- Schematic diagram of the experimental set-up for adsorption equilibrium measurements.

The measurements were performed for CO_2, CH_4 and N_2 at 303, 343 and 373 K up to 9 bar.

In all experiments, the values obtained corresponded to the excess adsorbed phase concentration and in order to correct the buoyancy effect two helium pycnometries were made assuming that helium is not adsorbed, one with the adsorbent and the other without (Appendix 1). Employing the buoyancy correction, the final equation to calculate the absolute amount adsorbed from the experimental data is:

$$q = \frac{\Delta m + \rho_G(V_S + V_C)}{m_S M_W} \frac{\rho_L}{\rho_L - \rho_G} \qquad \text{(Equation 3)}$$

where Δm is the difference of weight between measurements, ρ_G is the density of the gas phase at the measuring conditions (T,P), V_S is the volume of the solid adsorbent, V_C is the volume of the permanent magnet, the sample basket and the glass wool used to hold the sample, m_S is the adsorbent mass, M_w the adsorbate molecular weight and ρ_L the density of the adsorbed phase obtained as shown in Appendix 2.

The system monitories the pressure, the temperature and the weight variations. In order to obtain one experimental point of the adsorption isotherm, a small amount of gas is added to the cell containing the adsorbent sample and when the change in weight is approximately zero equilibrium has been reached. Then, another small amount of gas is added to the cell and another point is determined. This procedure is repeated until the highest desired pressure is achieved. After that, desorption points of the isotherm are obtained with progressive depressurization.

3.2.3 Zero Length Column

In order to obtain the diffusion coefficients of carbon dioxide, methane and nitrogen, zero length column tests were performed with the experimental set-up shown in Figure 6 and shematically represented in Figure 7.

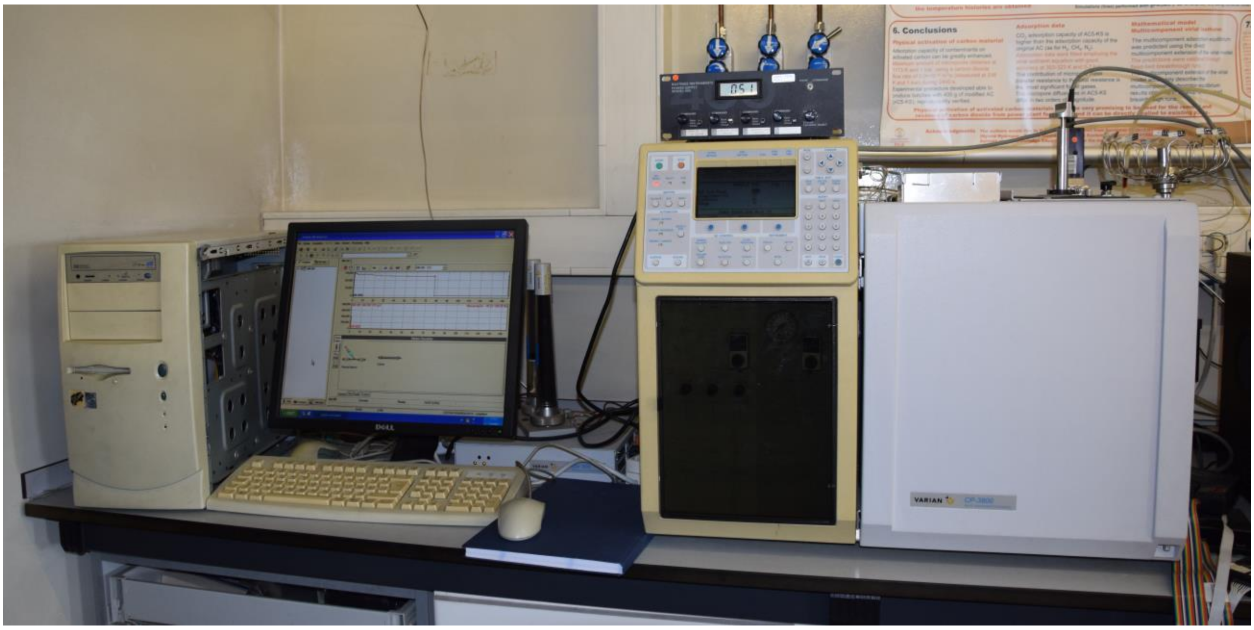

Figure 6- Varian gas chromatography (Varian, Holland).

The adsorbate was prepared by diluting a determined amount of pure gas in helium. For that, a mixture bottle was first cleaned. Using a vacuum pump, the bottle was initially cleaned by removing any existing gas. Then helium was injected and vacuum was again applied to remove any remaining impurities. A sampling tank of known volume was connected to the pure adsorbate bottle and filled up to a desired pressure. Then, the sampling tank was connected to the mixture bottle and the pure gas was pushed into the mixing bottle by passing helium until a total desired pressure was achieved.

The adsorbent was placed in the ZLC cell inside the gas chromatograph which allows experiments up to 673 K. The outlet stream was connected to a thermal conductivity detector (TCD) where the concentration of the gas was measured and then to a flame ionization detector (FID), which also ensures that emissions to the laboratory environment are avoided. Prior to the ZLC cell exists a multiport valve to switch the inlet stream from mixture (helium plus adsorbate) for saturation and pure helium for desorption. After the saturation of the column the run started by switching to a pure helium stream at time zero. The concentration of the adsorbate is followed continuously for enough time to ensure complete desorption of the sample.

ZLC experiments of CO_2, CH_4 and N_2 were performed at 308, 323, 343 and 373 K.

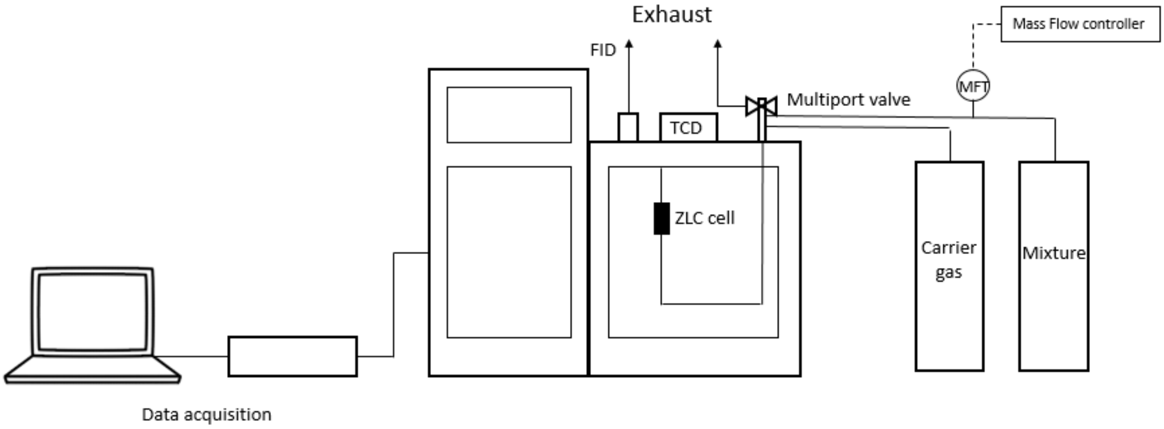

Figure 7- Zero length column experimental set-up.

In all experiments the mixture had 0.5% of the adsorbate diluted in helium so that the velocity variations within the column were reduced, the processed occurred under isothermal conditions and, above all, the measurements are carried out in the linear zone of the adsorption isotherm. The activation of the adsorbents was performed at 573 K at a heating rate of 1 K/min under a flow of Helium.

Therefore, considering that the homogeneous equation and the Fick’s law of diffusion can be applied to the kinetic measurements of a sorbate in an extrudate, the mass transfer control is limited either by macropore or micropore diffusion, and that the used sorbate concentration is low enough to describe adsorption equilibrium by Henry law, solution for infinite slabs, infinite cylinders and spheres were obtained [5]:

$$\frac{C}{C_0} = 2L \sum_{j=1}^{\infty} \frac{\exp(-\frac{D_{ap}\beta_j^2 t}{l^2})}{\beta_j^2 + L(L+1-n)} \qquad \text{(Equation 4)}$$

Where n is equal to 0, 1 or 2 for slabs, cylinders and spheres respectively, C and C_0 are the instantaneous and initial gas phase concentration respectively, D_{ap} is the apparent diffusivity, l is the representative spatial dimension of the pellet (radius for spheres and infinite cylinders and half length for infinite slabs), L is the ZLC parameter (Equation 5) and β_j the roots obtained from the transcendental equations (Equation 6).

$$L = \frac{Q_p l^2}{(n+1)K^* V_s D_{ap}} \qquad \text{(Equation 5)}$$

where Q_p is the purge flowrate, V_s is the volume of the adsorbent in the cell, $K^* = \varepsilon_p + (1 - \varepsilon_p)K_{eq}$ where ε_p is the porosity of the pellet and $K_{eq} = \rho_s H R_g T$ where ρ_s is the density of the solid and H the Henry constant.

Slabs	Cylinder	Spheres	
$\beta_j \tan(\beta_j) - L = 0$	$\beta_n J_1(\beta_n) - L J_0(\beta_n) = 0$	$\beta_j \cot(\beta_j) + L - 1 = 0$	(Equation 6)

where J_0 and J_1 are Bessel functions of first kind of order zero and one respectively.

For the case of micropore control the D_{ap}/l^2 has to be replaced by the crystal diffusivity and the spatial coordinate is the crystal representative spatial dimension (D_c/r_c^2). For the case of macropore control the pore diffusivity (D_p) is calculated throught Equation 7.

$$D_{ap} = \frac{\varepsilon_p D_p}{\varepsilon_p + (1-\varepsilon_p)K_{eq}} \qquad \text{(Equation 7)}$$

The long time response (LTR) for spherical pellets assuming linear adsorption equilibrium model is:

$$\ln\left(\frac{C}{C_0}\right) \cong ln\left(\frac{2L}{\beta_1^2 + L(L+1-n)}\right) - \frac{\beta_1^2 D_{ap} t}{l^2} \qquad \text{(Equation 8)}$$

The pore diffusivity (D_p) is related with the interaction of the adsorbate molecules with the pore walls (D_k) and the interaction between molecules (D_m). The Equation of Bosanquet (Equation 9) translates this relation, where τ_p is the tortuosity.

$$\frac{1}{D_p} = \tau_p\left(\frac{1}{D_m} + \frac{1}{D_k}\right) \qquad \text{(Equation 9)}$$

4 Results and Discussion

4.1 Zeolites characterization

To characterize the materials, and therefore obtain useful information for adsorption equilibrium and adsorption kinetics properties, several properties must be known. The N_2 and CO_2 physisorption isotherms measured at 77 K and 273 K, respectively, and mercury intrusion were performed at the *Universidad de Málaga*. Additionally, Scanning Electron Micrograph (SEM) and Energy Dispersive X-ray were performed at the *Centro de Materiais da Universidade do Porto;* and X-ray Diffraction (XRD) was performed in *Universidade de Aveiro*.

4.1.1 Zeolite 4A

SEM images of the 4A zeolite samples are presented in Figure 8 and in Appendix 3. Crystals with an average size of 1 µm can be observed. The characteristic cubic shape of the 4A zeolite crystals is observed for the three samples. However, some intergrowth of the crystals is also visible for the three samples. From the EDS spectra the expected elements were found (O, Na, Al, Si).

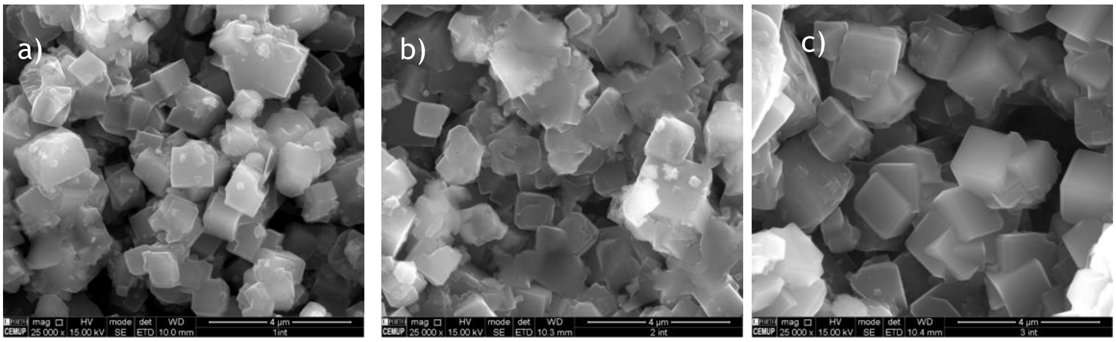

Figure 8- SEM images of zeolites: a) 4A BFK 2.5-5.0 mm, b) 4A BFK 1.6-2.5 mm, c) 4A BFK HSD 1.6-2.5 mm.

The pore size distribution obtained by mercury intrusion in the studied zeolite samples are presented in Figure 9.

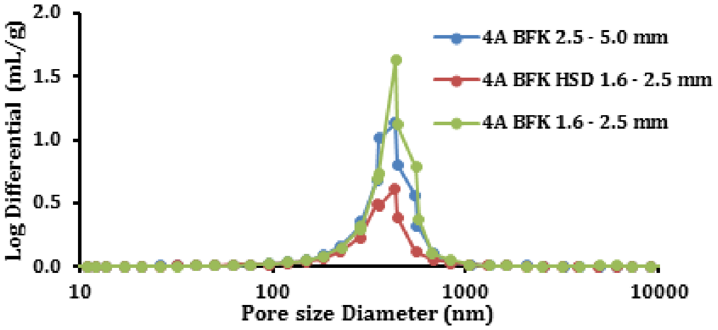

Figure 9- Pore size distribution by mercury intrusion of zeolite 4A.

From the mercury intrusion it can be concluded that all the samples have similar pore distribution and average pore diameter. The high density sample has the higher apparent and bulk density at 0.035 mPa standing out in Figure 9 due to the lower volume of pores.

A summary of the main measured properties assessed by mercury intrusion is presented in Table 1. The pellet density (apparent density, $\rho_{ap} = mass/pellet\ volume$) and the apparent solid density ($\rho_{s,Hg} = mass/(pellet\ volume - macro/meso\ pore\ volume)$) obtained by mercury intrusion are given as well as the solid density ($\rho_{s,He} = \mathrm{mass/solid\ volume}$) obtained by helium picnometry (Appendix 1).

Table 1- Total intrusion volume, surface area, average pore diameter, apparent and solid density obtained from mercury intrusion and solid density obtained form helium picnometry in the 4A zeolites.

		4A BFK 2.5-5.0 mm	4A BFK 1.6-2.5 mm	4A BFK HSD 1.6-2.5 mm
Total Intrusion Volume	$cm^3\ g^{-1}$	0.3012	0.3147	0.1606
Surface Area	$m^2\ g^{-1}$	3.837	3.491	2.004
Average Pore Diameter	nm	314.0	360.5	320.0
Pellet Density	$kg\ m^{-3}$	1091	1109	1406
Apparent Solid Density	$kg\ m^{-3}$	1624	1707	1819
Solid Density	$kg\ m^{-3}$	2063	2429	1667

The adsorption isotherm of Nitrogen at 77 K and of Carbon Dioxide at 273 K are presented in Figure 10 and the surface area data is summarized in the Table 2.

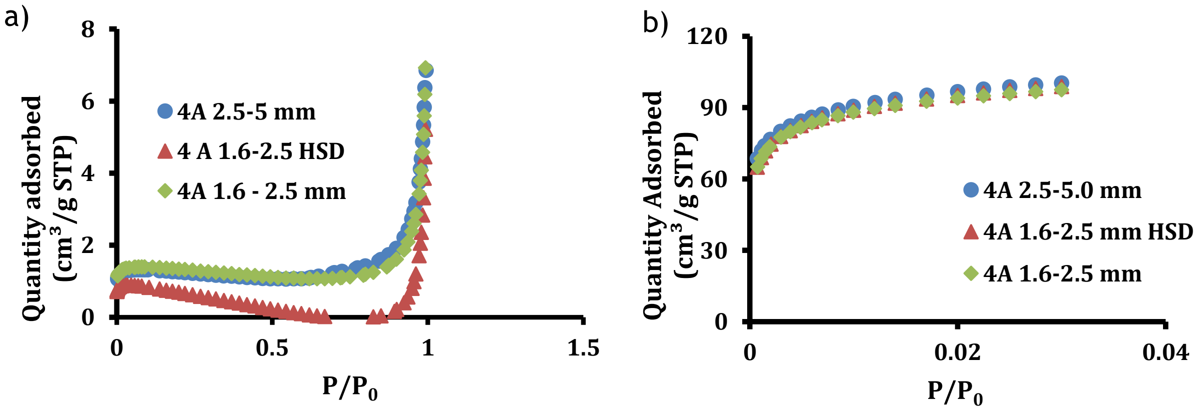

Figure 10- Adsorption isotherms in Zeolites 4A of Nitrogen at 77 K (a) and of Carbon Dioxide at 273 K (b).

As the diffusion of Nitrogen at 77 K in zeolite 4A is kinetically restricted, it is not possible to obtain meaningful physical values through this procedure. From the adsorption of Carbon Dioxide at 273 K, as the temperature is higher and therefore the kinetic energy of the molecules is greater, the diffusion into the narrow pores is speeded up allowing the determination of the surface area presented in Table 2. As the quantity adsorbed reaches a maximum for relative pressures below 0.04 it can be concluded that the adsorption only happens in the crystals.

Table 2- Surface area of zeolite 4A BFK 2.5-5.0 mm obtained from physisorption isotherms of Nitrogen at 77 K and Carbon Dioxide at 273 K.

	4A BFK 2.5-5.0 mm	**4A BFK 1.6-2.5 mm**	**4A BFK HSD 1.6-2.5 mm**
Surface Area m^2 g^{-1}	510.4	501.4	509.8

The X-Ray diffraction results of the 4A zeolites studied as well as the one obtained from the International Zeolite Association (IZA) [18] is represented in Figure 11. A good match can be found.

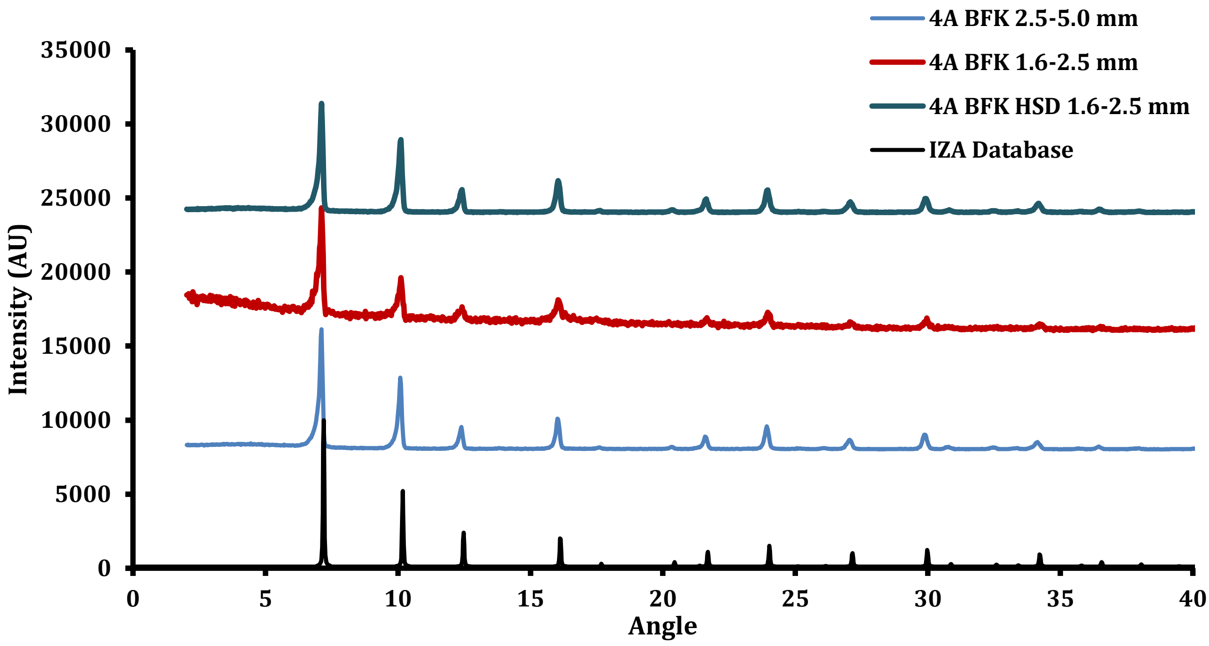

Figure 11- X-Ray diffraction data of the 4A zeolite samples.

4.1.2 Zeolite 13X

SEM images of the zeolite are presented in Figure 12 and in Appendix 3. The shape of the crystals is not regular. From the EDS spectra the expected elements were found (O, Na, Al, Si).

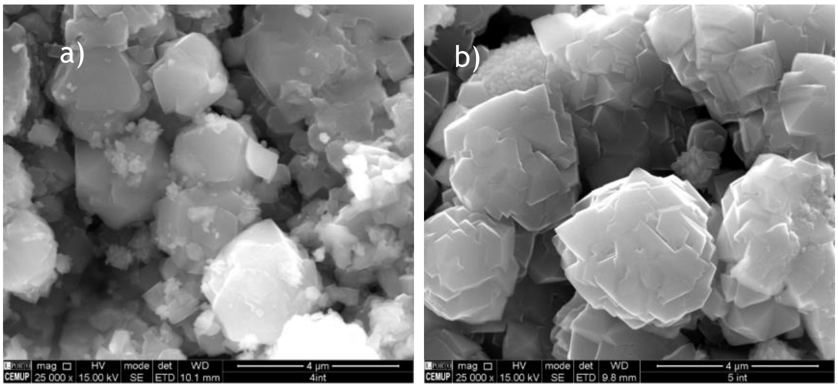

Figure 12- SEM images of zeolites: a) 13X BFK 1.2-2.0 mm, b) 13X BFK 6x8 mesh (2.36-3.35 mm).

The results of the pore size distribution are presented in Figure 13.

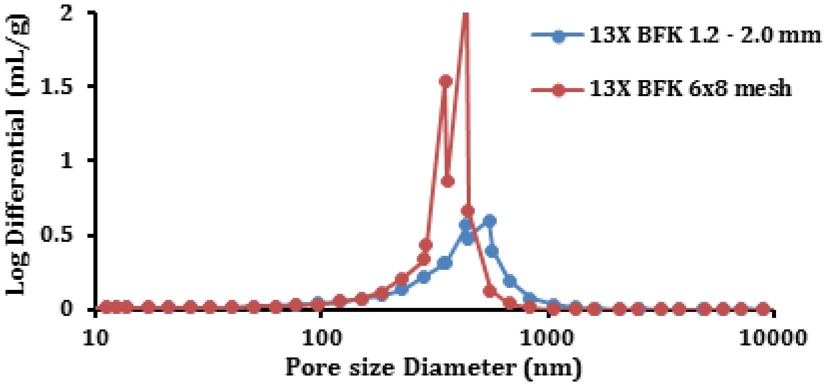

Figure 13- Pore size distribution by mercury intrusion of zeolites: a) 13X BFK 1.2 - 2.0 mm, b) 13X BFK 6x8 mesh (2.36-3.35 mm).

From the Figure 13 it can be concluded that both samples have similar average pore diameter. The sample with smaller pellets stands out due to the lower volume of pores.

The results from mercury intrusion are presented in Table 3. The pellet density (apparent density, $\rho_{ap} = mass/pellet\ volume$) and the apparent solid density ($\rho_{s,Hg} = mass/(pellet\ volume - macro/meso\ pore\ volume)$) obtained by mercury intrusion are given as well as the solid density ($\rho_{s,He} = \mathrm{mass/solid\ volume}$) obtained by helium picnometry (Appendix 1).

Table 3- Total intrusion volume, surface area, average pore diameter, apparent and solid density obtained from mercury intrusion and solid density obtained form helium picnometry in the 13X zeolites.

		13X BFK	***13X BFK***
		1.2 - 2.0 mm	***6x8 mesh* (2.36-3.35 mm)**
Total Intrusion Volume	cm^3 g^{-1}	0.2295	0.2964
Surface Area	m^2 g^{-1}	6.509	9.099
Average Pore Diameter	nm	141.0	130.3
Pellet Density	kg m^{-3}	1117	1036
Apparent Solid Density	kg m^{-3}	1502	1495
Solid Density	kg m^{-3}	-	2025

The 13X zeolites show higher surface areas and lower densities in comparison to 4A zeolites.

The adsorption isotherm of Nitrogen at 77 K and of Carbon Dioxide at 273 K are presented in Figure 14 and the obtained properties are sumarized in the Table 4.

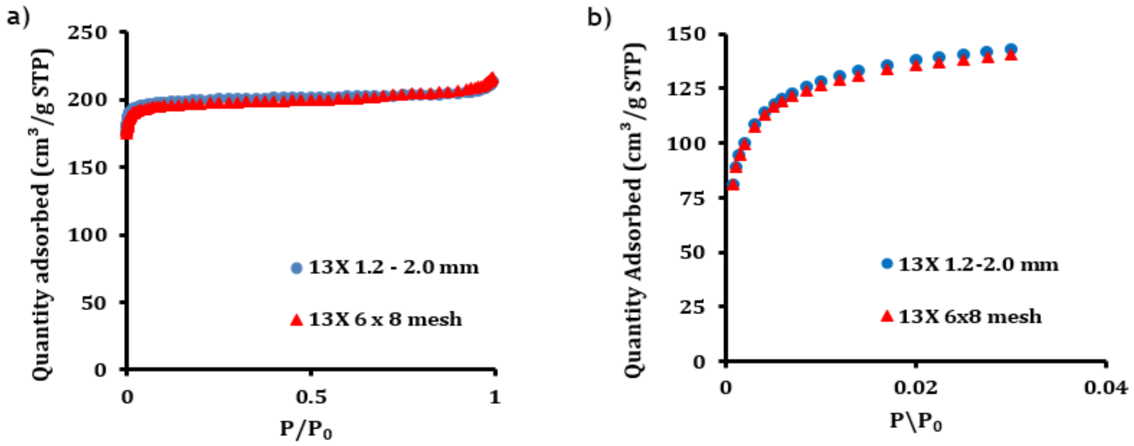

Figure 14- Adsorption isotherms in Zeolite 13X BFK of Nitrogen at 77 K (a) and of Carbon Dioxide at 273 K (b).

Table 4- Surface area of zeolite 13X BFK of Nitrogen 77 K and Carbon Dioxide at 273 K.

Surface Area m^2 g^{-1}	**13X BFK 1.2-2.0 mm**	**13X BFK 6x8 mesh (2.36-3.35 mm)**
N_2 at 77 K	875.2 ± 0.5	864.4 ± 0.6
CO_2 at 273 K	784.9	765.5

From both Nitrogen at 77 K and Carbon Dioxide at 273 K adsorption isotherms it can be concluded that the 13X zeolite samples have similar surface areas and, as the 4A samples, the quantity adsorbed reaches a maximum for relative pressures below 0.04 which allows to reach the conclusion that the adsorption also happens only in the crystals.

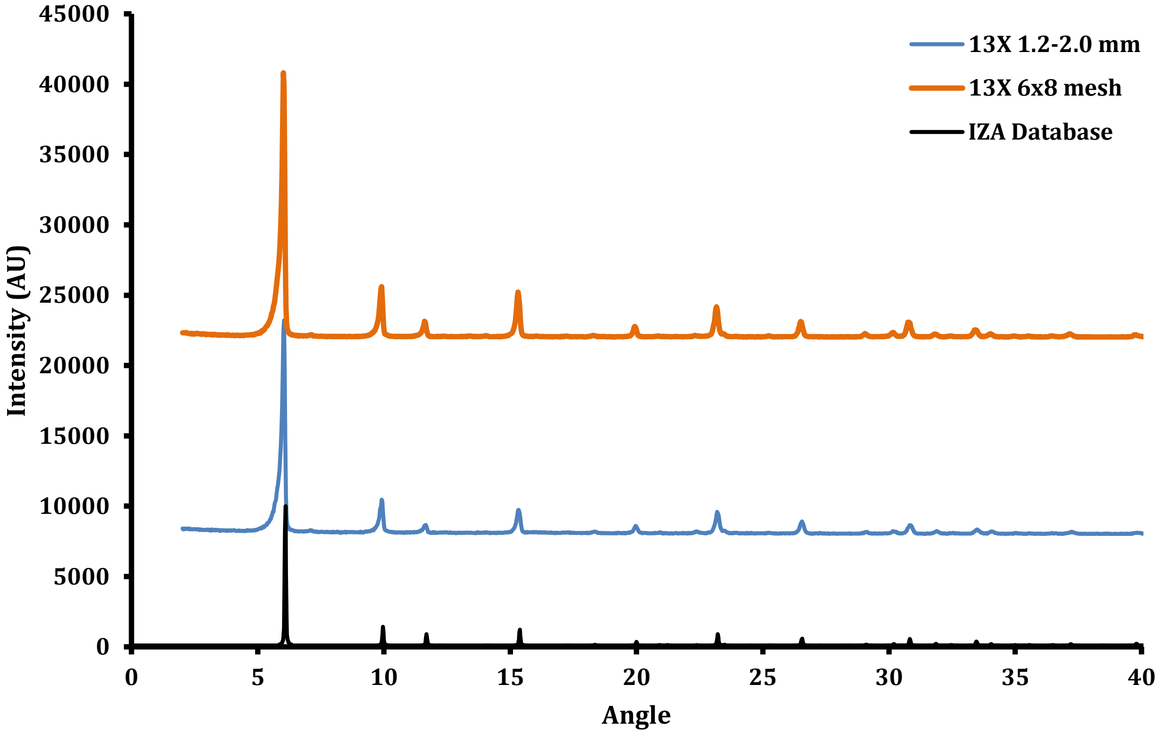

Figure 15- X-Ray diffraction data of the 13X zeolite samples.

The X-Ray diffraction of the 13X zeolites, represented in Figure 15, matches the one provided by the International Zeolite Association.

4.2 Adsorption equilibrium isotherms

Adsorption equilibrium of CO_2, CH_4 and N_2 on zeolite 4A BFK 1.6-2.5 mm was determined at 303, 343 and 373 K in the pressure range of 0 to 9 bar. Some points were also measured for the other 4A samples. The experimental results as well as adsorption isotherm model fittings (as described below) are presented in Figure 16. The 4A BFK 2.5-5.0 mm and 4A BFK 1.6-2.5 mm zeolites interactions with the adsorbate were equally well described by the model determined for the 4A BFK 1.6-2.5mm zeolite which was expected since the three samples have the same type of crystals. In Appendix 4 the isotherms of the different samples in terms of the amount adsorbed per mass and volume are presented in more detail. Figure 17 shows a comparison of the adsorption isotherms of amount adsorbed per volume of adsorbent for CO_2 where it can be clearly seen that in terms of capacity by volume the 4A BFK HSD is significantly better. A gain of 29% is observed. The advantagens of this material in terms of adsortion capacity are evident, significantly smaller equipement can be used.

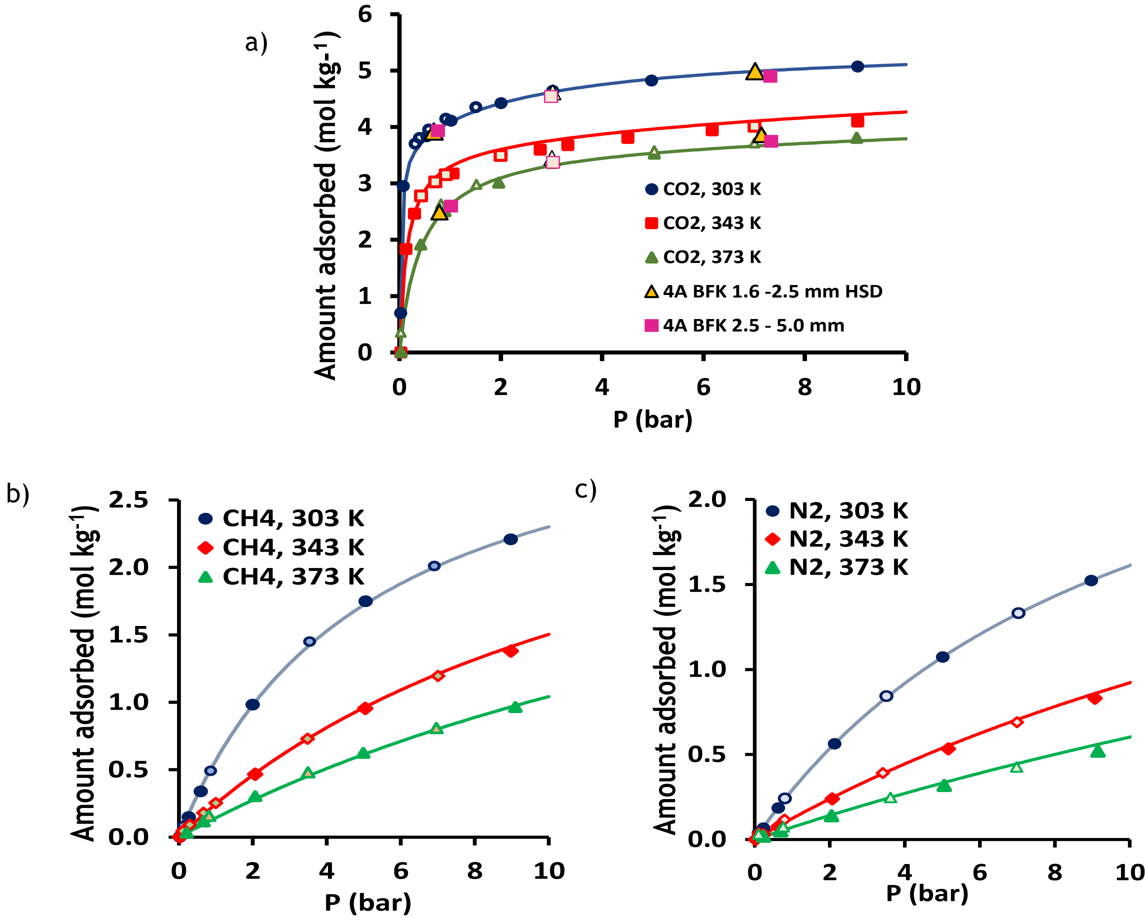

Figure 16- Amount of a) CO_2, b) CH_4 and c) N_2 adsorbed on 4A 1.6-2.5 mm zeolite: experimental points (closed adsorption, open desorption) at 303, 343, 373 K and Dual site Langmuir fiiting for CO_2 and One site Langmuir for CH_4 and N_2 (lines).

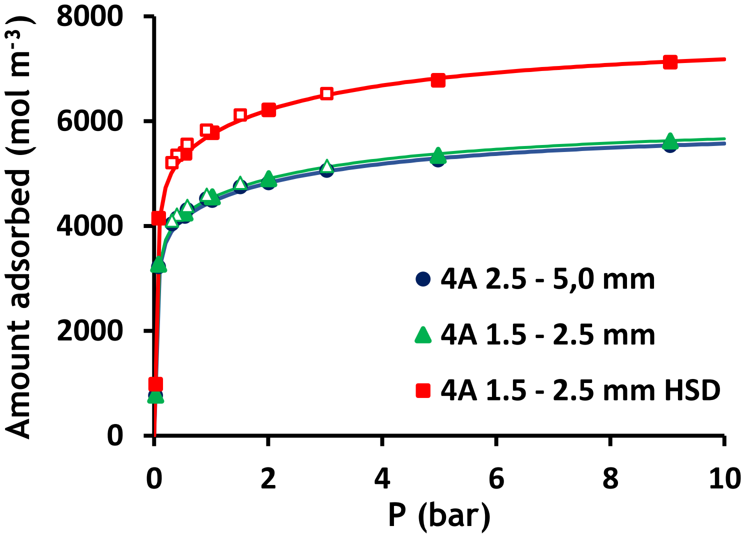

Figure 17- Comparison between the adsorption capacities per volume of adsorbent of CO_2 in 4A zeolites at 303 K.

As some equilibrium points were determined in adsorption (closed symbols) and others with desorption (open symbols) it was possible to conclued that inside the experimental error the sample has not shown hysteresis for any adsorbate at the three different temperatures.

$$q_i = q_{m1,i}\frac{K_{1,i}P}{1+K_{1,i}P} + q_{m2,i}\frac{K_{2,i}P}{1+K_{2,i}P} \qquad \text{(Equation 10)}$$

The carbon dioxide results were fitted with Equation 10 (Dual-site Langmuir). The parameters $q_{m1,i}$, $q_{m2,i}$, $K_{1,i}^0$, $K_{2,i}^0$, $(-\Delta H)_1$ and $(-\Delta H)_2$ for the carbon dioxide fitting and the $q_{m,i}$, K_i^0 and the $(-\Delta H)$ for methane and nitrogen were obtained by minimizing the sum of the absolute error between the experimental and calculated values. For the other adsorbates a Single site Langmuir proved to be sufficient. A good fitting was achieved.

The isotherm parameters are given in Table 5.

Table 5- Fitting parameters of the Langmuir model for CO_2, CH_4 and N_2 adsorption equilibrium on 4A BFK 1.6-2.5 mm.

Species	q_m (mol kg^{-1})		K_i^0 (bar^{-1})		$(-\Delta H)$ (kJ mol^{-1})	
CO_2	q_{m1}	q_{m2}	$K_{1,i}^0$	$K_{2,i}^0$	$(-\Delta H)_1$	$(-\Delta H)_2$
	1.81	3.68	2.01 x 10^{-8}	1.7581 x 10^{-5}	42.3	36.6
CH_4	3.47		5.88 x 10^{-5}		20.5	
N_2	3.24		3.98 x 10^{-5}		19.7	

In terms of amount adsorbed, CO_2 is the most adsorbed gas in the 4A zeolites studied and N_2 the less adsorbed. The value of the heat of adsorption is higher for CO_2 and smaller for N_2.

In a previous study [19] performed in LSRE, adsorption isotherms of CO_2 and CH_4 on the binderless 13X zeolite 1.2 – 2.0 mm had already been measured. In this work, some equilibrium points were measured on the other sample under study in order to compare the results. In Appendix 4, a comparison between the fitted model of the previous work and the poinst determined in this study is made. It can be seen that a good agreement is obtained. The adsorption equilibrium isotherms of N_2 in 13X BFK 6x8 mesh was then determined at 303, 343 and 373 K in the pressure range of 0 to 9 bar. The results are presented in Figure 18.

The nitrogen results were fitted with Equation 1 (Langmuir One-site). The $q_{m,i}$, K_i^0 and the $(-\Delta H)$ were obtained by minimizing the sum of the absolute error between the experimental and calculated values.

The isoterm parameters are given in Table 6.

Table 6- Fitting parameters of the Langmuir model for N_2 adsorption equilibrium on 13X BFK 6x8 mesh.

Species	q_m (mol kg^{-1})	K_i^0 (bar^{-1})	$(-\Delta H)$ (kJ mol^{-1})
N_2	4.10	8.61×10^{-5}	17.7

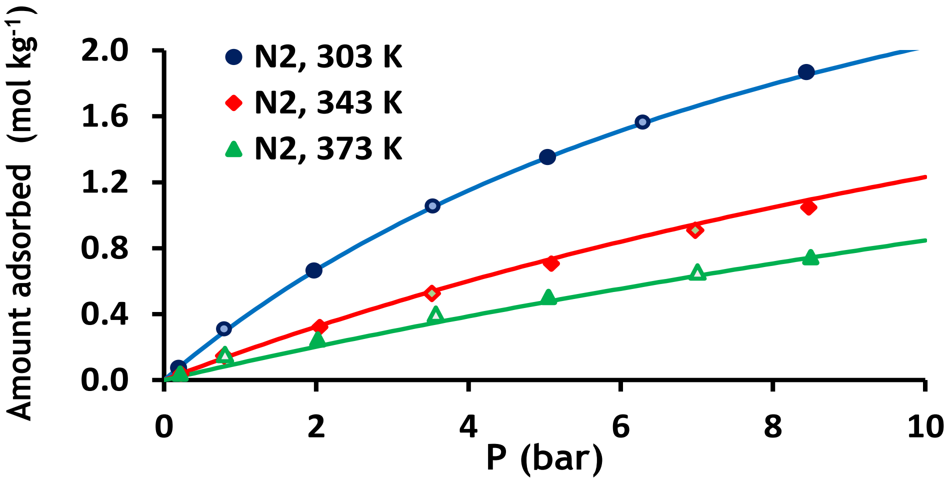

Figure 18- Adsorption equilibrium isoterms of N_2 on 13X BFK 6x8 mesh zeolite: experimental points (closed adsorption, open desorption) at 303, 343, 373 K and One site Langmuir (lines).

A good fitting was achieved. In terms of amount adsorbed, CO_2 is the most adsorbed gas in the 13X zeolites studied and N_2 the less adsorbed. The heat of adsorption is also higher for the CO_2 and smaller for N_2.

4.3 Isosteric heat of adsorption

The isosteric heat of adsorption determines the extent of adsorbent temperature changes within the adsorber during the adsorption and desorption steps of the processes [20]. It can be estimated by the Clausius-Clapeyron equation:

$$(-\Delta H_i) = R_g T^2 \left(\frac{\partial ln P_i}{\partial T}\right)_q \qquad \text{(Equation 11)}$$

where ΔH_i is the isosteric heat of adsorption of componente i, R_g is the universal gas constant and T is the temperature of the system. The derivative is evaluated at constant amount adsorbed, q. From the slope of the plot of $ln P_i$ as a function of $1/T$ the isosteric heat of adsorption can be estimated.

Figure 19 shows the single component isosteric heats of adsorption on 4A BFK 1.6-2.5 mm zeolite as a function of the amount adsorbed as well as the heat of adsorption obtained from the Langmuir isotherm model.

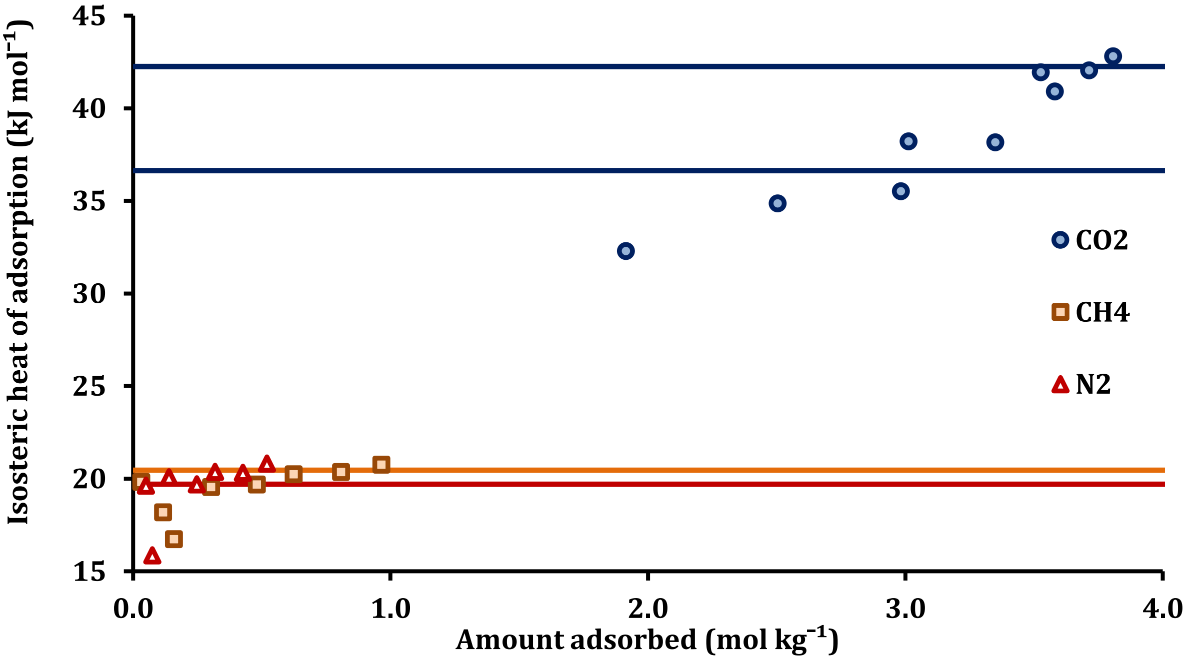

Figure 19- Single-component isosteric heats of adsorption on 4A BFK 1.6-2.5 mm for CO_2, CH_4 and N_2 as function of the amount adsorbed in the temperature range of 303 - 373 K; Lines are the values obtained through the Langmuir fitting.

In the literature, values of the isosteric heat of adsorption in 4A zeolite of 47.8 kJ mol^{-1} for the adsorption of CO_2 [21], 23.8 kJ mol^{-1} for N_2 and 16.72 kJ mol^{-1} for CH_4 [22] were found. Comparing the heats of adsorption of this material with the values reported in literature it can be concluded that in the case of CO_2 and N_2 the values in the present work are slightly lower and slightly higher for CH_4.

Figure 20 shows the single component isosteric heats of adsorption on 13X BFK 6x8 mesh zeolite as a function of the amount adsorbed as well as the heat of adsorption obtained from the Langmuir isotherm model.

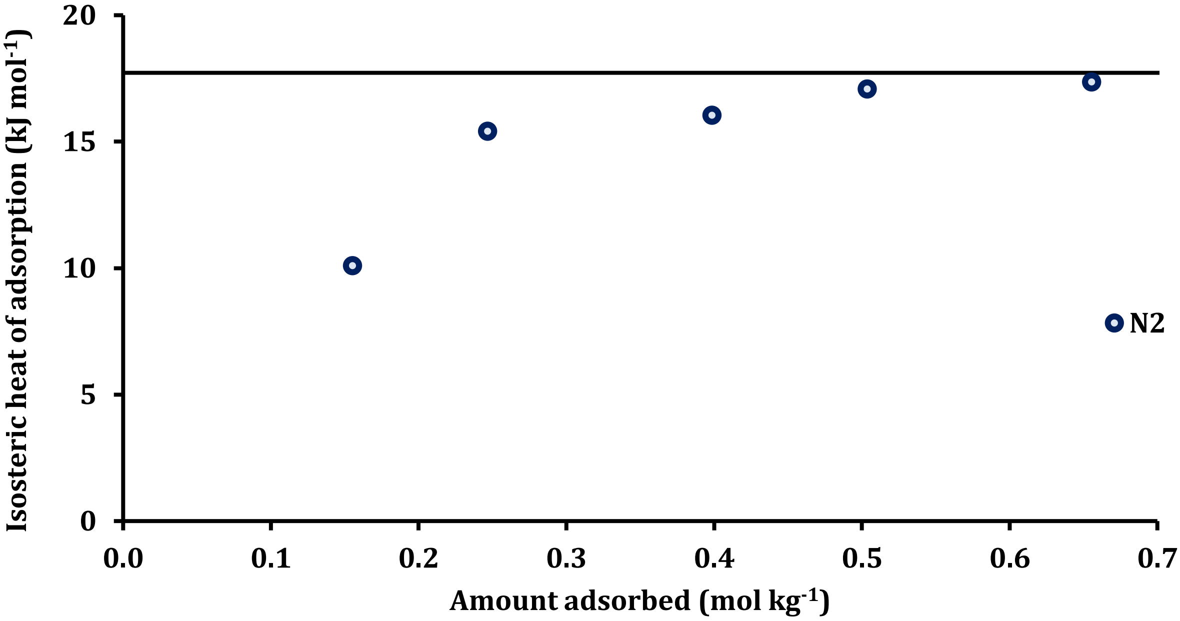

Figure 20- Single-component isosteric heat of adsorption on 13X BFK 6x8 mesh for N_2 as function of the amount adsorbed in the temperature range of 303 – 373 K; Lines are the values obtained through the Langmuir fitting.

Comparing the heats of adsorption of N_2 in this material with values reported in literature (15.7 kJ mol^{-1}) it can be concluded that the values in the present work are higher which indicates a stronger adsorption of this gas [2].

4.4 Adsorption kinetics

In order to determine the diffusion control mechanism and the diffusivity coefficients, of carbon dioxide, methane and nitrogen in 4A and 13X zeolites, several experiments with different flow rates and at different temperatures were performed. A thermal condutivity detector was used to detect CO_2 and N_2 and a flame ionization detector was used to detect CH_4, due to the highest sensitivity offered. The temperatures studied were 308, 323, 343 and 373 K.

Nitrogen desorption could not be analysed by this technique because the decrease in concentration dropped from the saturation value to zero almost instantaneously.

In order to determine the diffusivity coefficient of the adsorption of CO_2 and CH_4, the parameters D_{ap}/l^2, K^* and β were calculated through the long time response (LTR) using the fact that β should be approximatly equal to π for spheres and, analysing the fitting to the complete model (TS). Using the long time response results, as a first estimate for the complete model, another set of parameters were determinated.

The calibration of the flow rates and the caracteristics of the ZLC columns are presented in Appendix 5 and 6, respectively.

Table 7- Flow rate of the experiments at different temperatures (at the experimental conditions).

Temperature (K)	**Flow rate x 10^7 (m^3 s^{-1})**	
	CO_2	**CH_4**
308	5.28	6.58
323	5.54	6.90
343	5.88	9.84
373	6.39	10.70

The ZLC results are presented in the next sections and in Appendix 7.

4.4.1 4A BFK 2.5-5.0 mm

The experimental conditions used in the ZLC measurements of CO_2 and CH_4 in 4A BFK 2.5-5.0 mm are reported in Table 8. The ZLC results for CO_2 at each temperature and at 4.68 x 10^{-7} m^3 s^{-1} flow rate (PTN conditions) are shown in Figure 21. The ZLC results for CH_4 at 5.83 x 10^{-7} m^3 s^{-1} (PTN conditions) for experiments at 308 and 323 K and 7.83 x 10^{-7} m^3 s^{-1} (PTN conditions) for experiments at 343 and 373 K are shown in Figure 22. The flow rate at the conditions of the experiment can be found in Table 7.

Table 8- Experimental conditions for the ZLC runs with 4A BFK 2.5 – 5.0 mm.

Adsorbate	CO_2	CH_4
Adsorbate partial pressure (bar)	0.005	
Mass of adsorbent x 10^3 (kg)	0.0685	
Cell height x 10^2 (m)	0.89	
Cell volume x 10^7 (m^3)	1.18	
Cell porosity, ε	0.43	

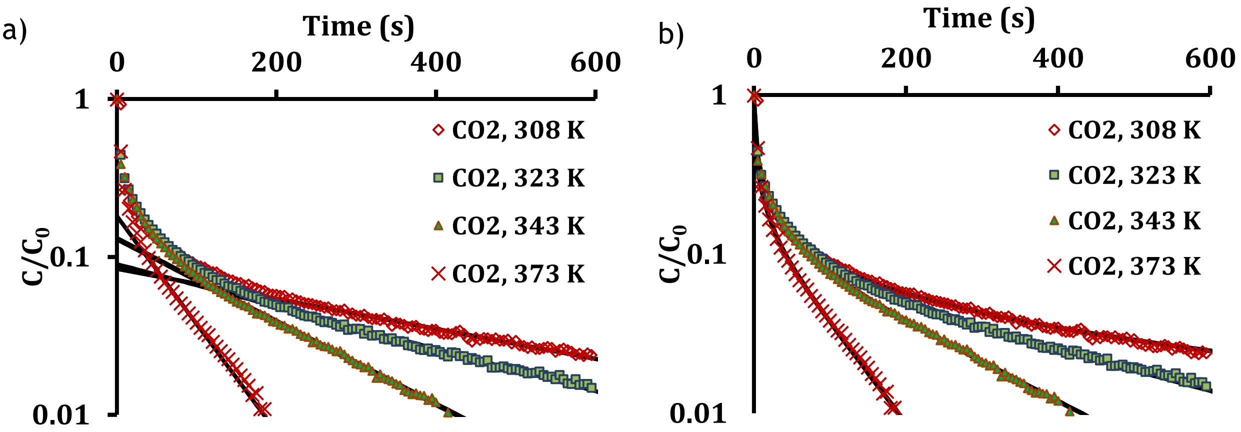

Figure 21- ZLC curves for CO_2 in 4A BFK 2.5 – 5.0 mm zeolite at 308 - 373 K. Solid lines in (a) represent the results using the long time response and (b) the complete ZLC model results.

The results from the determination of the parameters D_{ap}/l^2, K^*, L and β for carbon dioxide and methane are summed up in Tables 9 and 10.

Table 9- Long time response and complete ZLC model parameters for CO_2 in 4A BFK 2.5 - 5.0 mm zeolite at 308, 323, 343 and 373 K.

T **(K)**	***Q*** **x 10^7 (m^3 s^{-1})**	***Dap*** ***l^{-2}*** **x 10^4 (s^{-1})**		***K^****		***L***		***β***
		LTR	**TS**	**LTR**	**TS**	**LTR**	**TS**	**LTR**
308	5.28	2.41	1.07	446	470	24	52	3.03

323	5.54	3.42	3.17	353	332	23	26	3.00
343	5.88	6.96	6.47	266	255	16	18	2.95
373	6.39	19.1	17.3	147	143	11	13	2.87

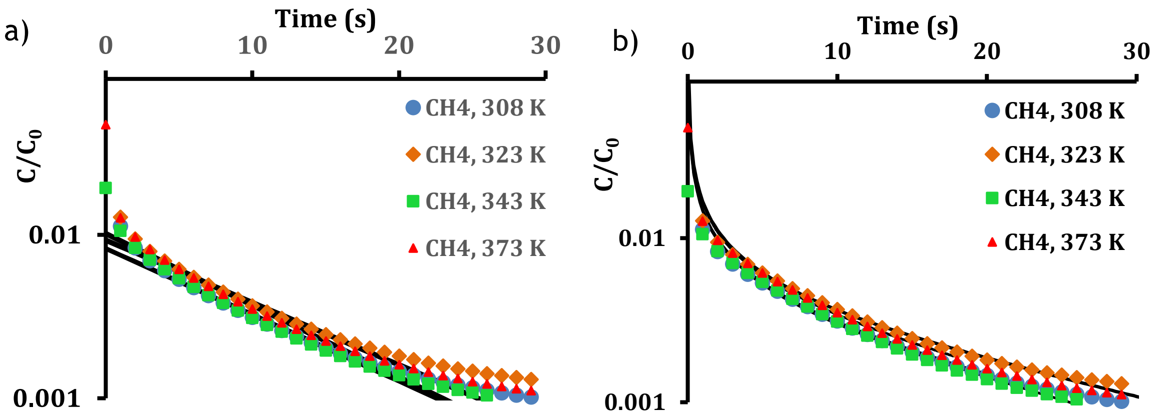

Figure 22- ZLC curves for CH_4 in 4A BFK 2.5 - 5.0 mm zeolite at 308, 323, 343 and 373 K. Solid lines in (a) represent the results using the long time response and (b) the complete ZLC model results.

Table 10- Long time response and the complete ZLC model parameters for CH_4 in 4A BFK 2.5 - 5.0 mm zeolite at 308, 323, 343 and 373 K.

T (K)	*Q* x 10^7 (m^3 s^{-1})	*Dap* l^{-2} x 10^3 (s^{-1})		K^*		*L*		*β*
		LTR	TS	LTR	TS	LTR	TS	LTR
308	6.58	9.50	6.14	1.4	1.3	242	416	3.13
323	9.26	9.64	5.00	2.5	2.2	195	413	3.13
343	7.33	9.77	5.94	1.4	1.3	261	487	3.13
373	10.70	10.3	6.06	2.6	2.3	197	380	3.13

4.4.2 4A BFK 1.6-2.5 mm

The experimental conditions used in the ZLC measurements of CO_2 and CH_4 in 4A BFK 1.6-2.5 mm are reported in Table 11. The ZLC results for CO_2 at each temperature and at 4.68 x 10^{-7} m^3 s^{-1} flow rate (PTN conditions) are shown in Figure 23. The ZLC results for CH_4 at 5.83 x 10^{-7} m^3 s^{-1} (PTN conditions) for experiments at 308 and 323 K and 7.83 x 10^{-7} m^3 s^{-1} (PTN conditions) for experiments at 343 and 373 K are shown in Figure 24 (CH_4). The flow rate at the conditions of the experiment can be found at Table 7.

Table 11- Experimental conditions for the ZLC runs with 4A BFK 1.6 – 2.5 mm.

Adsorbate	CO_2	CH_4
Adsorbate partial pressure (bar)	0.005	
Mass adsorbent x 10^3 (kg)	0.0442	
Cell height x 10^2 (m)	0.86	
Cell volume x 10^7 (m^3)	1.14	
Cell porosity, ε	0.67	

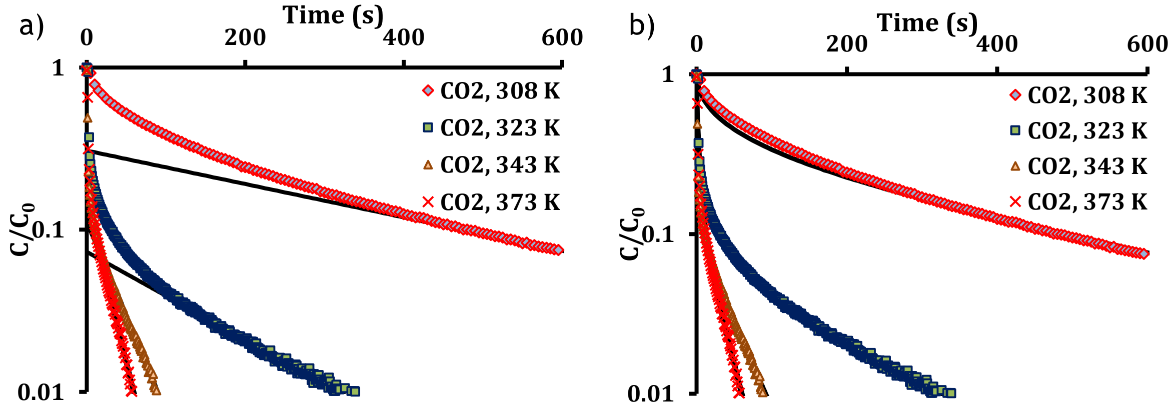

Figure 23- ZLC curves for CO_2 in 4A BFK 1.6 – 2.5 mm zeolite at 308, 323, 343 and 373 K. Solid lines in (a) represent the results using the long time response and (b) the complete ZLC model results.

The results from the determination of the parameters D_{ap}/l^2, K^*, L and β for carbon dioxide and methane are given in Tables 12 and 13.

Table 12- Long time response and the complete ZLC model for CO_2 in 4A BFK 1.6 – 2.5 mm zeolite at 303, 323, 343 and 373 K.

T (K)	Q x 10^7 (m^3 s^{-1})	Dap l^{-2} x 10^4 (s^{-1})		K^*		L		β
		LTR	TS	LTR	TS	LTR	TS	LTR

308	5.28	3.30	3.37	2222	2256	6	6	2.68
323	5.54	6.81	6.24	257	244	28	32	3.03
343	5.88	31.0	27.2	93	87	18	22	2.97
373	6.39	54.3	49.8	78	74	13	15	2.91

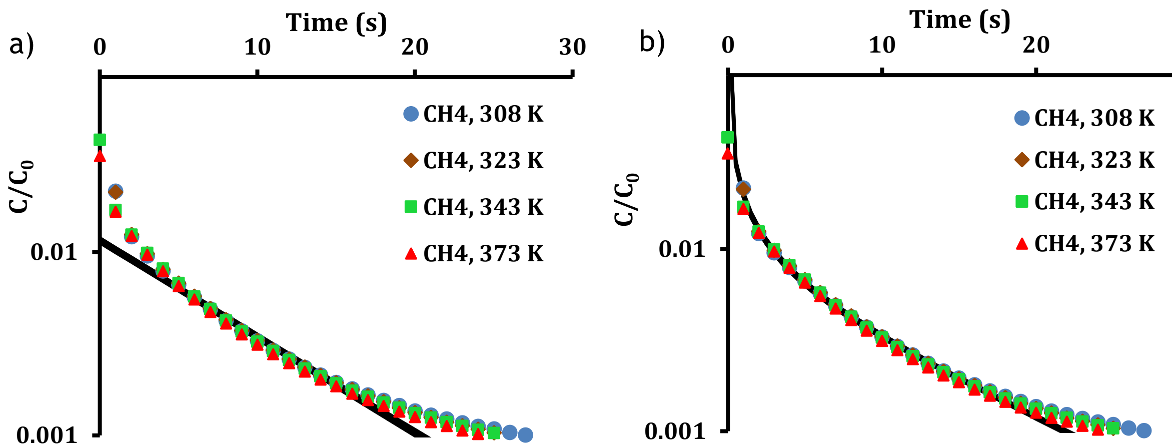

Figure 24- ZLC curves for CH_4 in 4A BFK 1.6 - 2.5 mm zeolite at 308, 323, 343 and 373 K. solid lines in (a) represent the results using the long time response and (b) the complete ZLC model results.

Table 13- Long time response and the complete ZLC model parameters for CH_4 in 4A BFK 1.6 - 2.5 mm zeolite at 308, 323, 343 and 373 K.

T (K)	Q x 10^7 (m^3 s^{-1})	Dap l^{-2} x 10^2 (s^{-1})		K^*		L		β
		LTR	TS	LTR	TS	LTR	TS	LTR
308	6.58	1.21	1.01	2.8	2.5	174	232	3.12
323	5.54	1.20	0.995	2.1	1.8	198	269	3.13
343	9.84	1.24	0.971	4.1	3.6	169	247	3.12
373	10.70	1.24	0.994	4.3	3.9	176	248	3.12

4.4.3 4A BFK 1.6-2.5 mm HSD

The experimental conditions used in the ZLC measurements of CO_2 and CH_4 in 4A BFK 1.6-2.5 mm HSD are reported in Table 14. The ZLC results for CO_2 at each temperature and at 4.68 x 10^{-7} m^3 s^{-1} flow rate (PTN conditions) are shown in Figure 25. The ZLC results for CH_4 at 5.83 x 10^{-7} m^3 s^{-1} (PTN conditions) for experiments at 308 and 323 K and 7.83 x 10^{-7} m^3 s^{-1} (PTN conditions) for experiments at 343 and 373 K are shown in Figure 26 (CH_4). The flow rate at the conditions of the experiment can be found at Table 7.

Table 14- Experimental conditions for the ZLC runs with 4A BFK 1.6 – 2.5 mm HSD.

Adsorbate	CO_2	CH_4
Adsorbate partial pressure (bar)	0.005	
Mass adsorbent x 10^3 (kg)	0.0510	
Cell height x 10^2 (m)	0.70	
Cell volume x 10^7 (m^3)	0.92	
Cell porosity, ε	0.59	

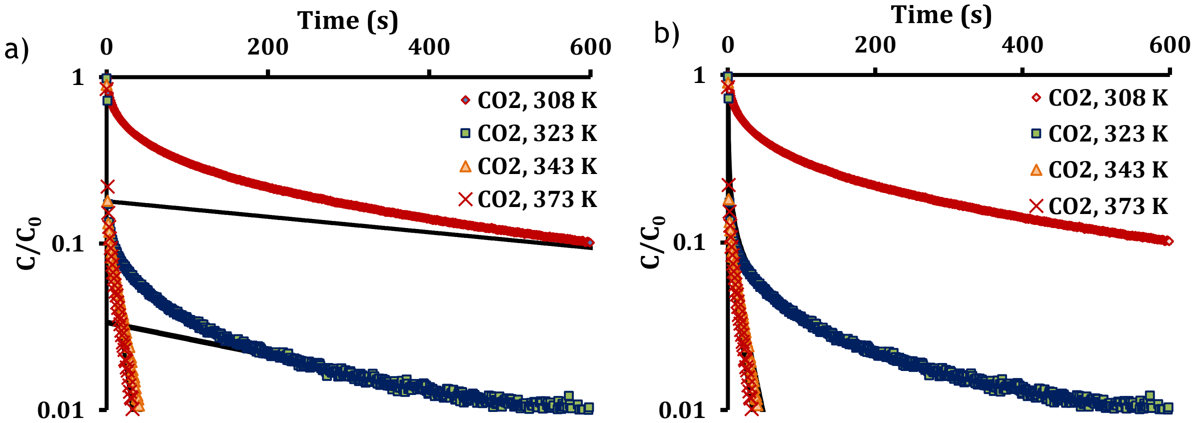

Figure 25- ZLC curves for CO_2 in 4A BFK 1.6 – 2.5 mm HSD zeolite at 308, 323, 343 and 373 K. Solid lines in (a) represent the results using the long time response and (b) the complete ZLC model results.

The results from the determination of the parameters D_{ap}/l^2, K^*, L and β for the adorption of carbon dioxide and methane are reported in Table 15 and 16.

Table 15- Long time response and the complete ZLC model parameters for CO_2 in 4A BFK 1.6 - 2.5 mm HSD zeolite at 303, 323, 343 and 373 K.

T (K)	Q x 10^7 (m^3 s^{-1})	*Dap* l^{-2} x 10^4 (s^{-1})		*K**		*L*		*β*
		LTR	TS	LTR	TS	LTR	TS	LTR

308	5.28	1.30	1.19	3144	3067	11	13	2.87
323	6.90	2.51	0.80	342	387	71	197	3.10
343	7.33	4.74	35.3	50	46	27	40	3.03
373	7.97	14.9	12.7	129	119	37	47	3.06

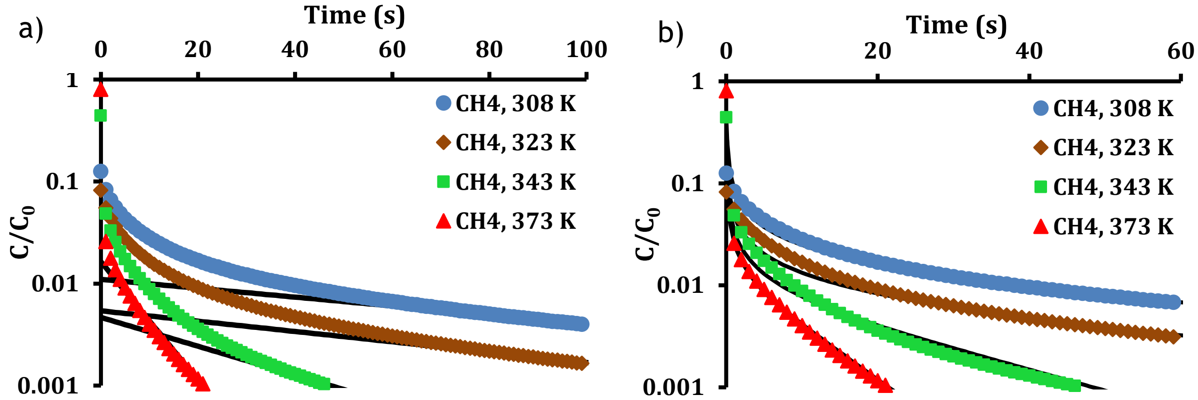

Figure 26- ZLC curves for CH_4 in 4A BFK 1.6 - 2.5 mm HSD zeolite at 308, 323, 343 and 373 K. Solid lines in (a) represent the results using the long time response and (b) the complete ZLC model results.

Table 16- Long time response and the complete ZLC model parameters for CH_4 in 4A BFK 1.6 - 2.5 mm HSD zeolite at 308, 323, 343 and 373 K.

T (K)	**Q x 10^7 (m^3 s^{-1})**	***Dap l*$^{-2}$ x 10^3 (s^{-1})**		***K****		***L***		***B***
		LTR	**TS**	**LTR**	**TS**	**LTR**	**TS**	**LTR**
308	6.58	1.03	1.11	31.0	29.6	183	178	3.12
323	6.90	1.19	1.53	44.9	43.6	371	270	3.13
343	9.84	3.32	4.83	13.8	14.8	430	204	3.13
373	7.97	13.2	11.8	10.0	10.4	195	245	3.13

4.4.4 4A BFK Zeolites – Determination of the diffusional controlling mechanism and the difusivity coefficients

To discriminate correctly between the importance of macropore or micropore diffusion, it is necessary to carry out experiments in pellets with different sizes but the same crystal size or pellets with the same size but different crystal size [5]. In the present study the three 4A BFK zeolites have different pellet sizes, and from Figure 8 it can be seen that 4A BFK 1.6-2.5 mm HSD has bigger crystals.

The apparent CO_2 diffusivity coefficient for each zeolite is shown in Table 17.

Table 17- Diffusivity coeficient for CO_2 in zeolites: 4A BFK 2.5 – 5.0 mm, 4A BFK 1.6 – 2.5 mm and 4A BFK 1.6 – 2.5 mm HSD at different temperatures.

$D_{ap}/l^2 \times 10^4$ (s^{-1})	Pellet size (R_p)	308 K	323 K	343 K	373 K
4A BFK 2.5 - 5.0 mm	0.2	1.1	3.4	6.5	17.3
4A BFK 1.6 - 2.5 mm	0.1	3.3	6.2	27.2	49.8
4A BFK 1.6 - 2.5 mm HSD	0.1	1.3	2.5	41.3	14.9

As can be seen from Table 17, beside the results at 343 K, which do not follow the trend of the remaining temperatures, the D_{ap}/l^2 is similar for 4A BFK 2.5-5.0 mm and 4A BFK 1.6-2.5mm HSD zeolites (within experimental error) which is an indication of micropore diffusion control since the pellets have different sizes but the crystal size is similar. The comparison between 4A BFK 2.5 -5.0 mm and 4A BFK 1.6 -2.5 mm (pellets with different size and similar crystal size) shows that the D_{ap}/l^2 results are different, suggesting macropore diffusion control. Therefore, a more detailed evaluation of the temperature dependency of the diffusivity values will be made below.

It is known that the micropore diffusion is an activated process with exponential dependence in temperature, according to Equation 12, and that the pore diffusivity (macropore diffusion control) varies as a polinomial function of temperature, Equations 13 – 15.

$$\frac{D_c}{r_c^2} = \frac{D_c^0}{r_c^2}\, exp\left(-\frac{E_a}{R_g T}\right) \qquad \text{(Equation 12)}$$

$$D_k = 0.97\, r_p\sqrt{\frac{T}{M_w}} \qquad \text{(Equation 13)}$$

$$D_m = \frac{1-y_i}{\sum_{\substack{j=1\\ j\neq 1}}^{n}\frac{y_i}{D_{ij}}} \qquad \text{(Equation 14)}$$

$$D_{ij} = \frac{2.66\times 10^{-2}T^{3/2}}{PM_{ij}^{1/2}\sigma_{ij}^2\Omega_{D_{ij}}} \qquad \text{(Equation 15)}$$

where D_c^0 is the limiting diffusivity at infinite temperature, r_c the crystal representative spatial dimension (crystal radius), E_a the activation energy of micropore/crystal diffusion, M_w the adsorbate molecular weight, r_p the pore radius (in cm and Dk in $m^2\ s^{-1}$), y_i the molar fraction of component i, D_{ij} the binary molecular diffusivity of component i and j, σ_{ij} is the average of the collision molecular diameters of components i and j and Ω_{Dij} the dimensionless collision integral of diffusivity.

In order to evaluate the apparent diffusivity coefficient dependence with temperature, the relations discribed in Equations 12 to 15 were applied and Figure 27 was obtained.

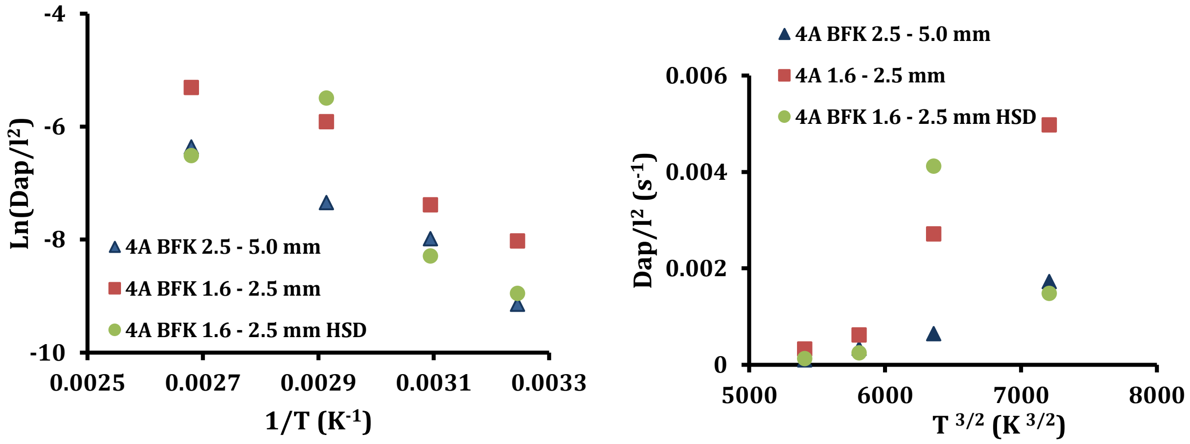

Figure 27- Dependence of the apparent diffusivity coeficient for CO_2 in 4A zeolites with temperature.

From Figure 27, it can be seen that the representation of $\ln(\frac{D_{ap}}{l^2})$ as function of $1/T$ shows a linear trend, which is an indication of micropore diffusion control for CO_2 in 4A zeolites. However, this trend is not seen in the representation of $\frac{D_{ap}}{l^2}$ as function of $T^{3/2}$, except for the 4A BFK 1.6 – 2.5 mm HSD, if the experiment at 343 K is not taken into account, which indicates that macropore diffusion control can also be possible.

Assuming macropore diffusion control, the pore diffusivity can be calculated by Equation 9 using the he molecular and Knudsen diffusivity coefficients shown in Table 18. The pore radius indicated in the table is the average pore radius obtained from mercury intrusion.

Table 18- Molecular and Knudsen diffusivity coefficients for the CO_2/He mixture.

	308 K	323 K	343 K	373 K
$D_{m\ He/CO_2}$ $(m^2\ s^{-1}) \times 10^5$	6.37	6.90	7.63	8.79
$D_{k\ (rp=1.6 \times 10^{-5} cm)}$ $(m^2\ s^{-1}) \times 10^5$	4.11	4.20	4.33	4.52

Aplying a logarithm scale to the isotherm (Appendix 8) the Henry's region can be identified, the Henry's constant (H) calculated, and the equilibrium constant ($K_{eq} = \rho_s H R_g T$) obtained (Table 19).

Table 19- Henry's law constant and equilibrium constant for 4A zeolites.

Temperature (K)	**308**	**323**	**343**	**373**
Henry's law constant, H (mol kg^{-1} Pa^{-1})	1.03 x 10^{-3}	4.77 x 10^{-4}	2.26 x 10^{-4}	8.21 x 10^{-5}
$K_{eq\,4A\,BFK\,1.6-2.5\,mm}$	4429.79	2186.23	1100.81	434.61
$K_{eq\,4A\,BFK\,1.6-2.5\,mm\,HSD}$	4720.92	2329.91	1173.16	463.18
$K_{eq\,4A\,BFK\,2.5-5.0\,mm}$	4214.68	2080.07	1047.35	413.51

Assuming that the diffusion mechanism control is in the macropores, the pore diffusivity D_p can be calculated by Equation 7 using the Dap obtained in the ZLC tests. Figure 28 shows the dependency of the pore diffusivity values with $T^{3/2}$.

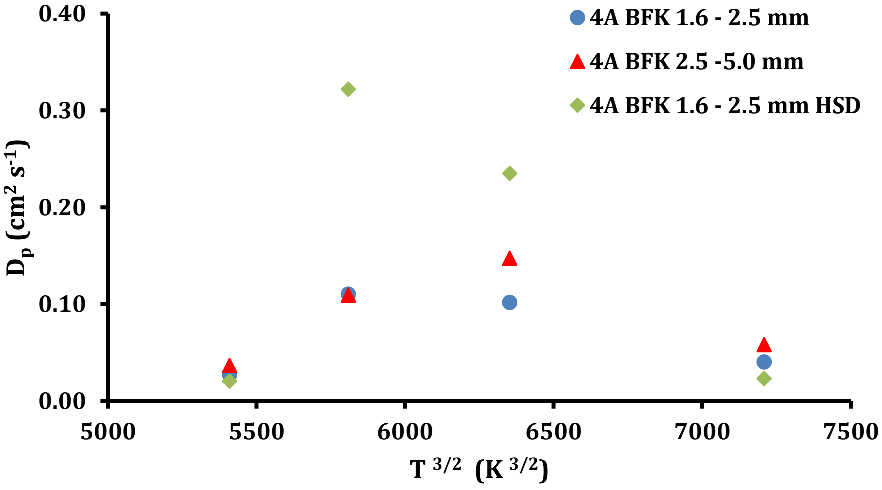

Figure 28- Dependency of the pore diffusivity in 4A BFK zeolites with $T^{3/2}$.

Analysing Figure 28 it can be seen that the pore diffusivity values do not follow a linear dependence with $T^{3/2}$, therefore the micropore diffusion is the controlling mechanism for all 4A samples.

For the adsorption of CH_4 the same procedure was applied. Table 20 shows the apparent diffusivities for the three 4A zeolites.

Table 20- Diffusivity coeficient for CH_4 in zeolites: 4A BFK 2.5 - 5.0 mm, 4A BFK 1.6 - 2.5 mm and 4A BFK 1.6 - 2.5 mm HSD at different temperatures.

D_{ap}/l^2 x 10^2 (s^{-1})	**Pellet size (R_p)**	**308 K**	**323 K**	**343 K**	**373 K**
4A BFK 2.5 - 5.0 mm	0.2	1.0	1.0	1.0	1.0

4A BFK 1.6 - 2.5 mm	0.1	1.2	1.2	1.2	1.0
4A BFK 1.6 -2.5 mm HSD	0.1	0.1	0.2	0.3	1.2

From Table 20 it can be seen that the D_{ap}/l^2 is the same for the 4A BFK 2.5 -5.0 mm and 4A BFK 1.6 – 2.5 mm which suggests micropore diffusion control.

In order to determine the apparent diffusivity coefficient dependence with temperature, the relations discribed in Equations 12 to 15 were also applied and Figure 29 was obtained.

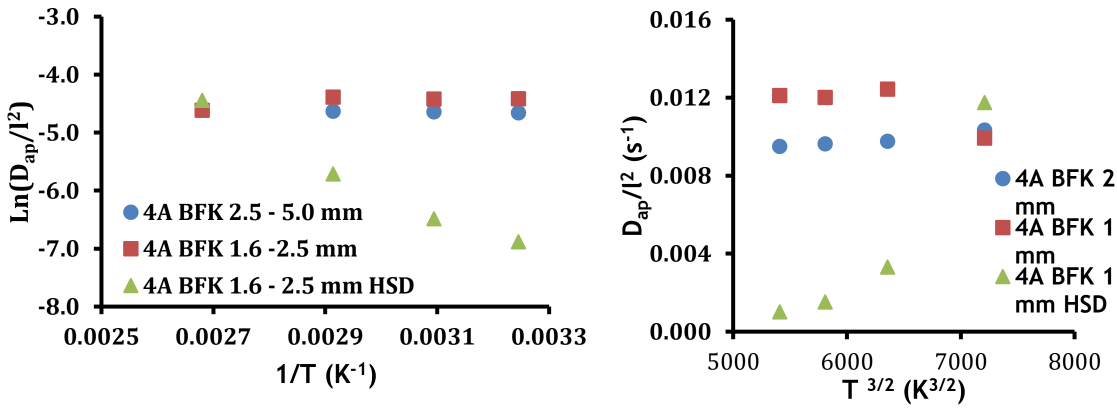

Figure 29- Dependence of the apparent diffusivity coeficient for CH_4 in 4A zeolites with temperature.

It can be seen that, except for the HSD material, the results showed no temperature dependence. In order to understand this results blank tests with ZLC columns filled with glass spheres were performed. The results are shown in Figure 30 and it can be concluded that the diffusion of CH_4 in 4A BFK 2.5 – 5.0 mm and 4A BFK 1.6 - 2.5 mm zeolites is faster than the system response and cannot be measured. In the case of 4A BFK 1.6 – 2.5 mm HSD zeolite, the diffusivity coefficient can be measured but not for the highest temperature, 373 K, in this case the experimental points only show the systems's behavior.

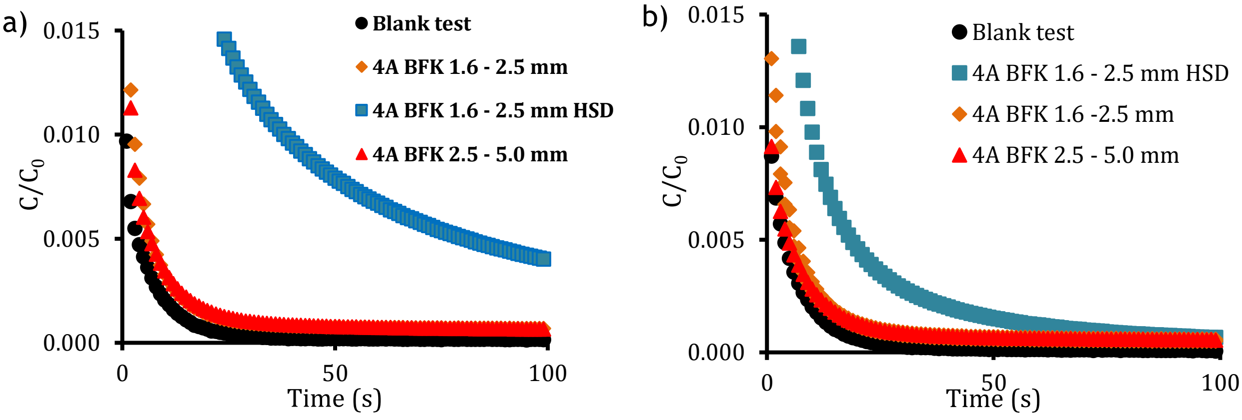

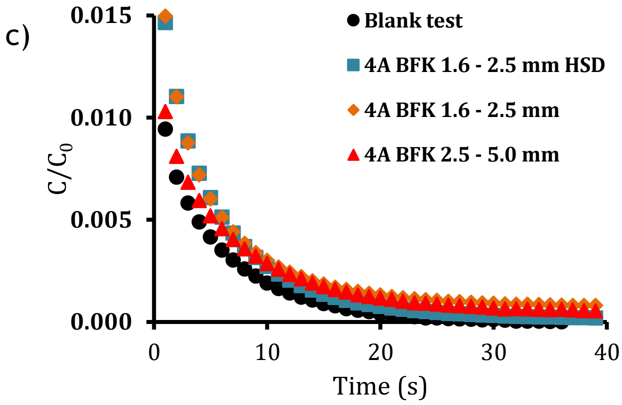

Figure 30- Comparison of the blank test with the results of 4A zeolites for: a) 308 K, b) 343 K and c) 373 K and a flow rate of 5.83 x 10^{-7} *m*^{3} *s*$^{-1}$ *in PTN conditions.*

From Figure 29 an exponential dependency of temperature of the D_{ap}/l^2 can be seen for 4A BFK 1.6 – 2.5 mm HSD zeolite, therefore the micropore diffusion is the controlling mechanism for CH_4.

Summarizing, it can be concluded that the crystal diffusivity is the controlling mechanism for CO_2 in all the 4A samples and for CH_4 in the high density sample. The values of D_c/r_c^2 were then calculated from the apparent diffusion obtained in the ZLC experiments (Table 21).

Table 21- Crystal diffusivity in 4A zeolites of CO_2 *and* CH_4.

$\boldsymbol{D_c/r_c^2}$ (s^{-1})		**308 K**	**323 K**	**343 K**	**373 K**
4A BFK 2.5 - 5.0 mm	CO_2	1.1 x 10^{-4}	3.4 x 10^{-4}	6.5 x 10^{-4}	17.3 x 10^{-4}
4A BFK 1.6 - 2.5 mm	CO_2	3.3 x 10^{-4}	6.2 x 10^{-4}	27.2 x 10^{4}	49.8 x 10^{-4}
4A BFK 1.6 -2.5 mm HSD	CO_2	1.3 x 10^{-4}	2.5 x 10^{-4}	41.3 x 10^{-4}	14.9 x 10^{-4}
	CH_4	0.1 x 10^{-2}	0.2 x 10^{-2}	0.3 x 10^{-2}	-

4.4.5 13X BFK 1.2-2.0 mm

The experimental conditions used in the ZLC measurements of CO_2 and CH_4 in 13X BFK 1.2-2.0 mm are reported in Table 22. The ZLC results for CO_2 at each temperature at 4.68 x 10^{-7} m^3 s^{-1} (PTN conditions) are shown in Figure 31, and for CH_4 at 4.18 x 10^{-7} m^3 s^{-1} (PTN conditions) for experiments at 303 K and 6.83 x 10^{-7} m^3 s^{-1} (PTN conditions) for experiments at 323, 343 and 373 K are shown in Figure 32. The flow rate at the conditions of the experiment can be found at Table 7.

Table 22- Experimental conditions for the ZLC runs with 13X BFK 1.2 – 2.0 mm.

Adsorbate	CO_2	CH_4
Adsorbate partial pressure (bar)	0.005	
Mass adsorbent x 10^3 (kg)	0.0338	
Cell height x 10^2 (m)	0.60	
Cell volume x 10^7 (m^3)	0.79	
Cell porosity, ε	0.47	

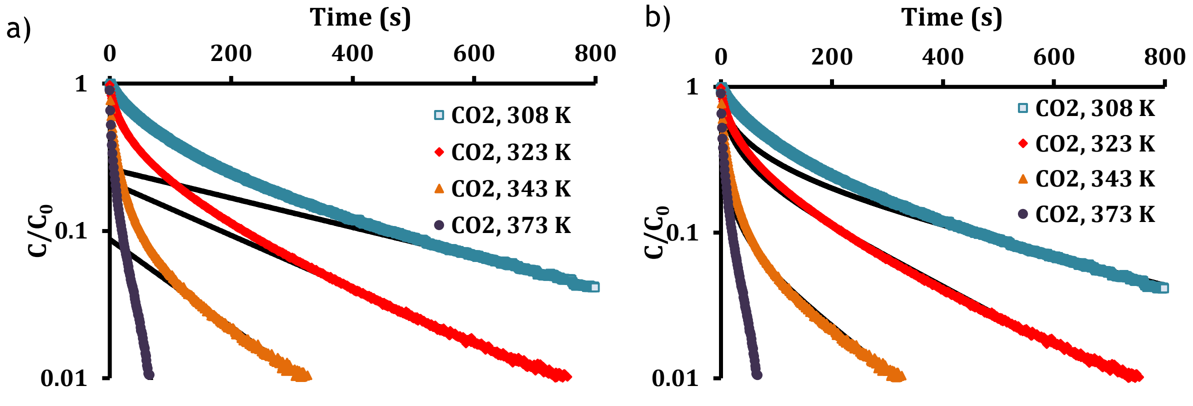

Figure 31- ZLC curves for CO_2 in 13X BFK 1.2 - 2.0 mm zeolite at 308, 323, 343 and 373 K. Solid lines in (a) represent the results using the long time response and (b) the complete ZLC model results.

The results from the determination of the parameters D_{ap}/l^2, K^*, L and β for carbon dioxide and methane are summed up in Tables 23 and 24.

Table 23- Long time response and the complete ZLC model parameters for CO_2 adsorption in 13X BFK 1.2 - 2.0 mm zeolite at 308, 323, 343 and 373 K.

T (K)	Q x 10^7 (m^3 s^{-1})	*Dap l^{-2}* x 10^{-4} (s^{-1})		K^*		L		β
		LTR	TS	LTR	TS	LTR	TS	LTR
308	6.58	3.04	3.07	2268	2317	8	7	2.75

323	6.90	5.24	6.27	1102	1210	9	7	2.82
343	7.33	7.55	7.75	328	334	23	22	3.01
373	7.97	68.4	66.5	133	131	7	7	2.71

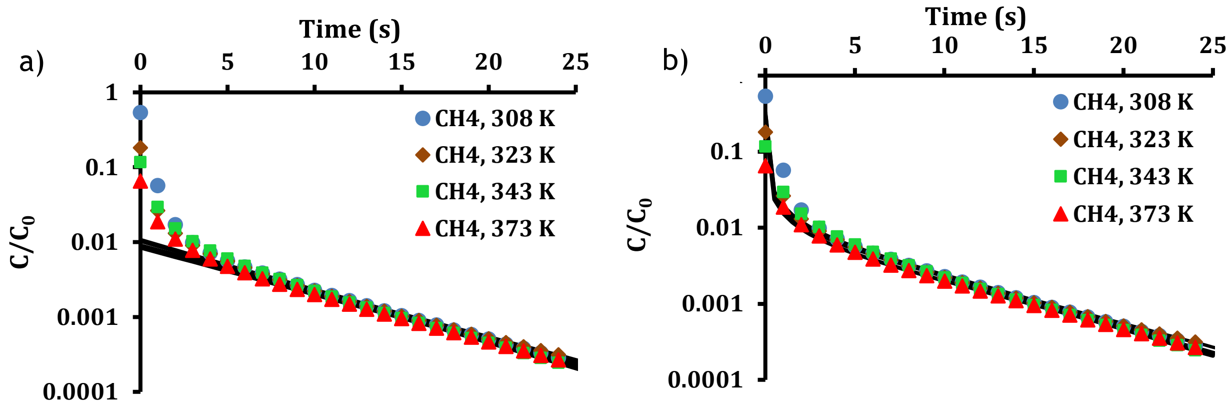

Figure 32- ZLC curves for CH_4 in 13X BFK 1.2 - 2.0 mm zeolite at 308, 323, 343 and 373 K. Solid lines in (a) represent the results using the long time response and (b) the complete ZLC model results.

Table 24- Long time response and the complete ZLC model parameters for CH_4 adsorption in 13X BFK 1.2 - 2.0 mm zeolite at 308, 323, 343 and 373 K.

T (K)	Q x 10^7 (m^3 s^{-1})	*Dap* l^{-2} x 10^{-2} (s^{-1})		*K**		*L*		*β*
		LTR	TS	LTR	TS	LTR	TS	LTR
308	7.71	1.40	1.57	1.3	1.3	213	160	3.13
323	8.08	1.44	1.45	1.6	1.6	223	214	3.13
343	8.58	1.62	1.64	2.0	2.4	188	179	3.12
373	10.70	1.48	1.47	1.7	1.8	238	240	3.13

4.4.6 13X BFK 6x8 mesh

The experimental conditions used in the ZLC measurements of CO_2 and CH_4 in 13X BFK 6x8 mesh are reported in Table 25. The ZLC results for CO_2 at each temperature at 4.68 x 10^{-7} m^3 s^{-1} (PTN conditions) are shown in Figure 33 and, for CH_4 at 4.18 x 10^{-7} m^3 s^{-1} (PTN conditions) for experiments at 308 K and 6.83 x 10^{-7} m^3 s^{-1} (PTN conditions) for experiments at 323, 343 and 373 K are shown in Figure 34. The flow rate at the conditions of the experiment can be found at Table 7.

Table 25- Experimental conditions for the ZLC runs with 13X BFK 6x8 mesh.

Adsorbate	CO_2	CH_4
Adsorbate partial pressure (bar)	0.005	
Mass adsorbent x 10^3 (kg)	0.0353	
Cell height x 10^2 (m)	0.72	
Cell volume x 10^7 (m^3)	0.95	
Cell porosity, ε	0.55	

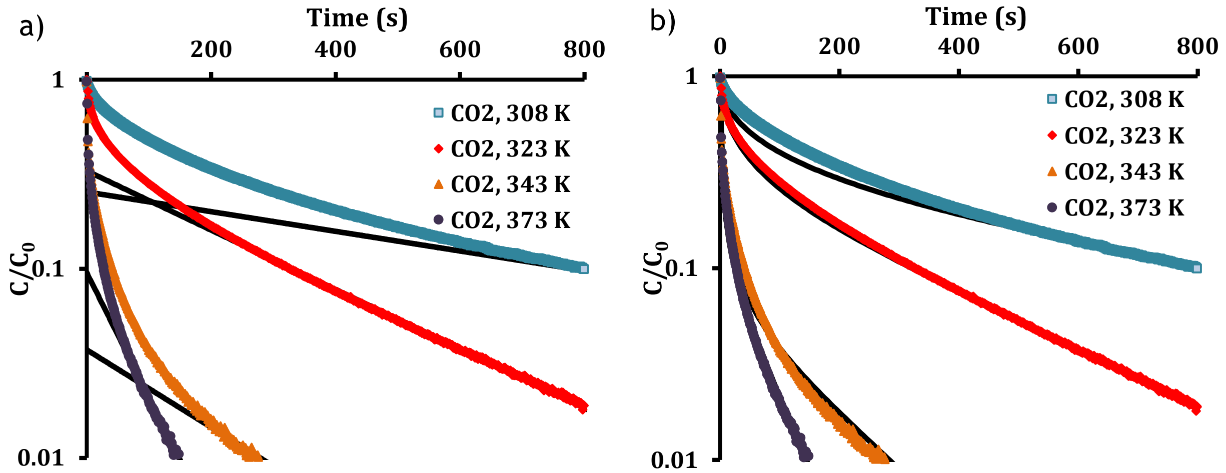

Figure 33- ZLC curves for CO_2 in 13X BFK 6x8 mesh zeolite at 308, 323, 343 and 373 K. Solid lines in (a) represent the results using the long time response and (b) the complete ZLC model results.

The results from the determination of the parameters D_{ap}/l^2, K^*, L and β for carbon dioxide and methane are summed up in Tables 26 and 27.

Table 26- Long time response and the complete ZLC model parameters for CO_2 adsorption in 13X BFK 6x8 mesh zeolite at 308, 323, 343 and 373 K.

T (K)	$Q \times 10^7$ ($m^3\ s^{-1}$)	$Dap\ l^{-2} \times 10^{-4}$ (s^{-1})		K^*		L		B
		LTR	TS	LTR	TS	LTR	TS	LTR
308	7.71	2.06	2.14	3059	3544	10	9	2.82
323	8.08	5.15	4.65	1629	1744	8	9	2.75
343	9.84	7.50	10.3	211	291	49	29	3.08
373	10.70	13.6	15.5	171	209	36	29	3.06

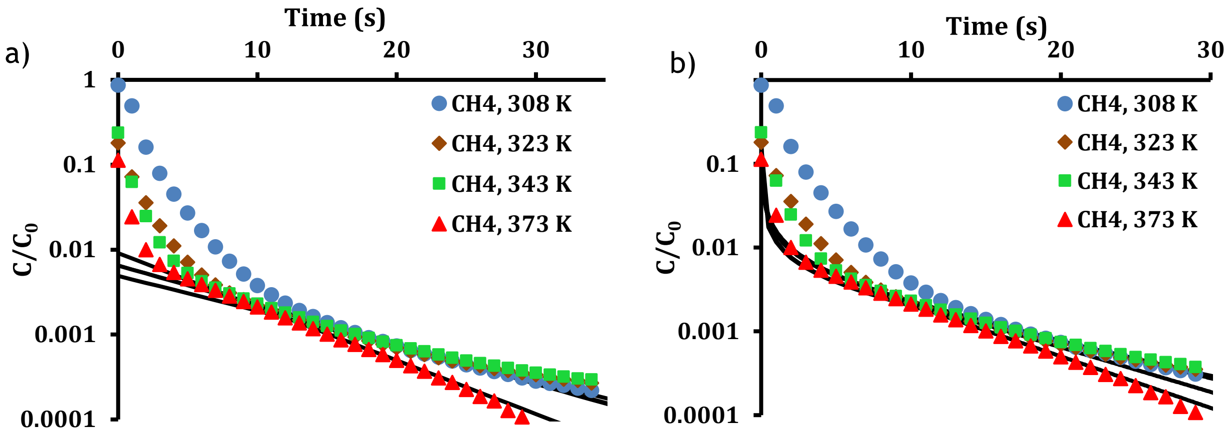

Figure 34- ZLC curves for CH_4 in 13X BFK 6x8 mesh zeolite at 308, 323, 343 and 373 K. Solid lines in (a) represent the results using the long time response and (b) the complete ZLC model results.

Table 27- Long time response and the complete ZLC model parameters for CH_4 adsorption in 13X BFK 6x8 mesh zeolite at 308, 323, 343 and 373 K.

T (K)	$Q \times 10^7$ ($m^3\ s^{-1}$)	$Dap\ l^{-2} \times 10^{-2}$ (s^{-1})		K^*		L		B
		LTR	TS	LTR	TS	LTR	TS	LTR
308	9.96	1.01	1.01	1.1	1.1	335	306	3.13
323	9.26	1.00	1.14	2.1	2.2	376	303	3.13
343	9.84	1.06	1.22	2.3	2.3	303	253	3.13
373	10.70	1.49	1.45	2.0	2.4	221	235	3.13

4.4.7 13X BFK Zeolites – Determination of the diffusional controlling mechanism and the difusivity coefficients

In the present study two 13X BFK zeolites with the different pellet sizes were analysed.

The apparent diffusivity coefficient for each zeolite is shown in Table 28.

Table 28- Diffusivity coeficient for CO_2 in zeolites: 13X BFK 1.2 - 2.0 mm, 13X BFK 6x8 mesh at different temperatures.

D_{ap}/l^2 x 10^4 (s^{-1})	**Pellet size (R_p)**	**308 K**	**323 K**	**343 K**	**373 K**
13X BFK 1.2 - 2.0 mm	0.10	3.1	6.3	16.4	66.5
13X BFK 6x8 mesh	0.15	2.1	4.7	7.3	15.5

The same analysis done for the 4A zeolite is going to be made for 13X zeolite. Figure 35 shows the values of ln (D_{ap}/l^2) as function of 1/T and of D_{ap}/l^2 as function of $T^{3/2}$. The analysis of these graphics suggests that the micropore diffusion is the controlling mechanism.

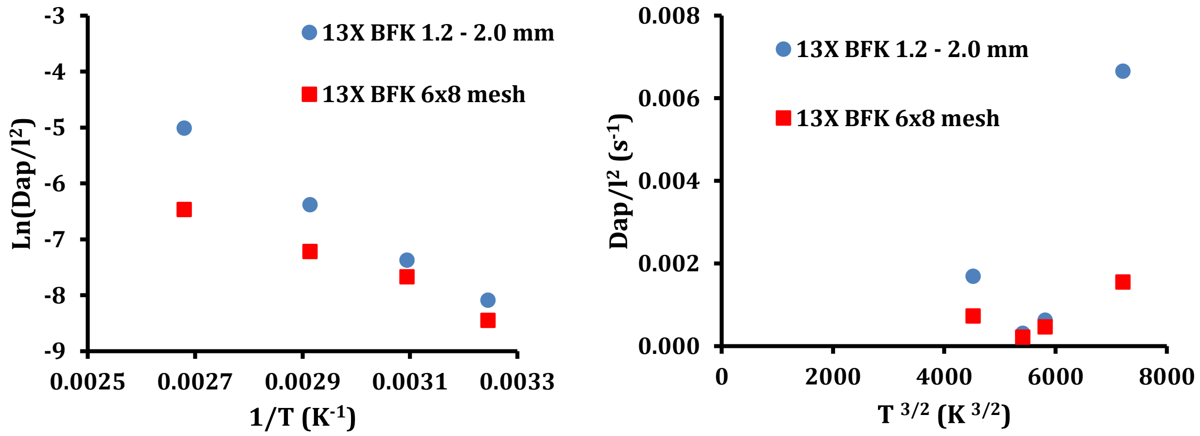

Figure 35- Dependence of the apparent diffusivity coeficient of CO_2 in 13X zeolites with temperature.

A more detailed evaluation of the temperature dependency of the diffusivity values will be made below.

Assuming macropore control, the pore diffusivity can be again calculated by Equation 9 using the molecular and Knudsen diffusivity coefficient shown in Table 29.

Table 29- Molecular and Knudsen diffusivity coefficients for the CO_2/He mixture.

	308 K	**323 K**	**343 K**	**373 K**
$D_{m\ He/CO2}$ (m^2 s^{-1}) x 10^5	6.37	6.90	7.63	8.79

D_k $_{(rp=7 \times 10^{-6} cm)}$ (m^2 s^{-1}) x 10^5	1.80	1.84	1.90	2.00

The Henry constant is defined as the limiting value [23] given by:

$$H = \lim_{P \to 0} \frac{q}{P}\bigg|_T \qquad \text{(Equation 16)}$$

In Appendix 6 the adsorption equilibrium for CO_2 and CH_4 in 13X BFK zeolites can be seen. For the Dual site Langmuir the Henry's constant can be expressed as $H = q_{sat,1}b_1 + q_{sat,2}b_2$. Applying this relation, the Henry's constant can be calculated and the equilibrium constant ($K_{eq} = \rho_s H R_g T$) obtained (Table 30).

Table 30- Henry's law constant and equilibrium constant for 13X zeolites.

Temperature (K)	**308**	**323**	**343**	**373**
Henry's law constante, H (mol kg^{-1} Pa^{-1})	2.63 x 10^{-3}	1.47 x 10^{-4}	8.69 x 10^{-4}	4.40 x 10^{-5}
$K_{eq\ 13X\ BFK\ 1.2-2.0\ mm}$	995.11	592.60	372.14	204.85
$K_{eq\ 13X\ BFK\ 6x8\ mesh}$	990.60	589.91	370.45	203.92

Assuming the diffusion mechanism control is in the macropores the pore diffusivity D_p can be calculated by Equation 7 using the Dap values obtained in the ZLC tests. Figure 36 shows the dependency of the pore diffusivity with $T^{3/2}$.

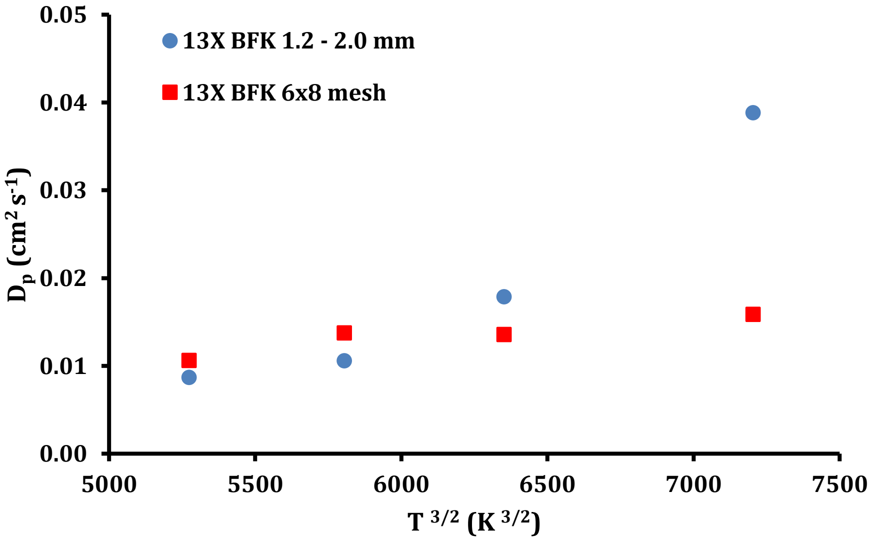

Figure 36- Dependency of the pore diffusivity in 13X BFK zeolites with $T^{3/2}$.

Analysing Figure 36 it can be seen that the pore diffusivity does not follow a polinomial dependence indicating that the micropore diffusion is the controlling mechanism.

For the CH_4 the same procedure was applied and Table 31 shows the apparent diffusivities for the two 13X zeolites.

Table 31- Diffusivity coeficient for adsorption of CH_4 in zeolites: 13X BFK 1.2 - 2.0 mm, 13X BFK 6x8 mesh at different temperatures.

$D_{ap}/l^2 \times 10^{-2}$ (s^{-1})	Pellet size (R_p)	308 K	323 K	343 K	373 K
13X BFK 1.2 - 2.0 mm	0.10	1.4	1.4	1.5	1.5
13X BFK 6x8 mesh	0.15	1.0	1.1	1.2	1.4

As can be seen from Table 31, within the experimental error. the D_{ap}/l^2 is similar for all zeolites which is an indication of micropore diffusion control. Analysing Figure 37, both exponential and polinomial dependence of the apparent diffusivity coefficient with temperature can be seen, therefore the temperature dependence analysis is inconclusive.

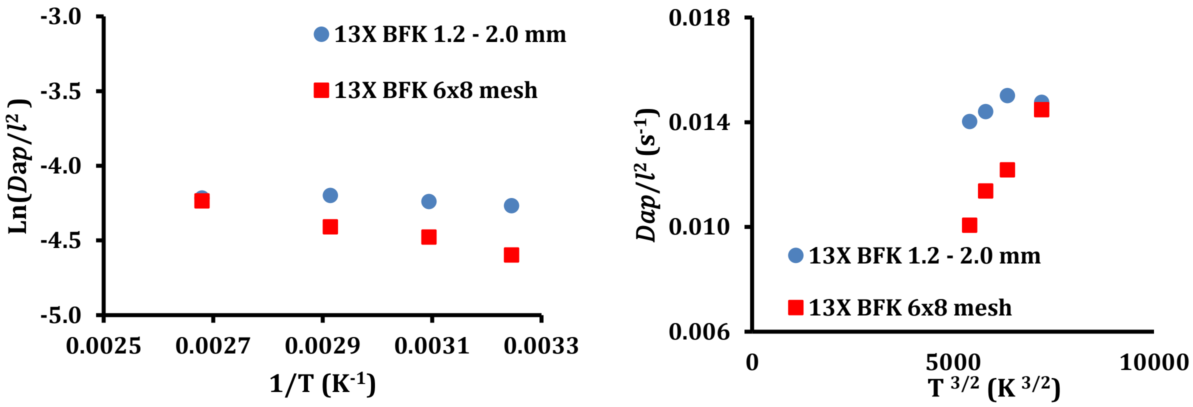

Figure 37- Dependence of the apparent diffusivity coeficient for adsorption of CH_4 in 13X zeolites with temperature.

Assuming macropore control, the pore diffusivity can be calculated by Equation 9 using the molecular and Knudsen diffusivity coefficient shown in Table 32.

Table 32- Molecular and Knudsen diffusivity coefficients for the CH_4/He mixture.

	308 K	323 K	343 K	373 K
$D_{m\ He/CH4}$ $(m^2\ s^{-1}) \times 10^5$	7.40	8.01	8.86	10.2
$D_{k\ \rho\pi=7 \times 10\text{-}6cm}$ $(m^2\ s^{-1}) \times 10^5$	2.98	3.05	3.14	3.27

Aplying Equation 16, the Henry's constant can be calculated and the equilibrium constant obtained (Table 33).

Table 33- Henry's law constant and equilibrium constant for 13X zeolites.

Temperature (K)	**308**	**323**	**343**	**373**
Henry's law constante, *H* (mol kg^{-1} Pa^{-1})	7.37 x 10^{-6}	4.81 x 10^{-6}	3.29 x 10^{-6}	1.99 x 10^{-6}
$K_{eq\ 13X\ BFK\ 1.2-2.0\ mm}$	27.89	19.41	14.09	9.28
$K_{eq\ 13X\ BFK\ 6x8\ mesh}$	27.76	19.32	14.02	9.23

Assuming that the diffusion mechanism control is in the macropores the pore diffusivity D_p can be calculated by Equation 7 using the Dap values obtained from the ZLC tests. Figure 37 shows the dependency of the pore diffusivity with $T^{3/2}$.

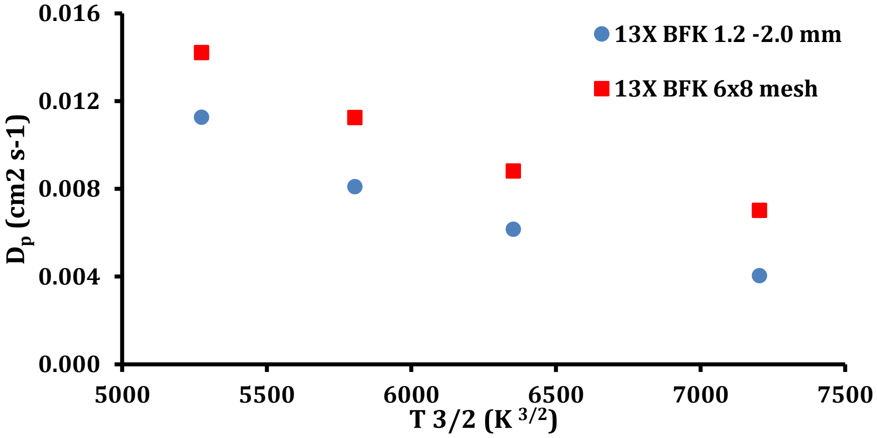

Figure 38- Dependency of the pore diffusivity in 13X BFK zeolites with $T^{3/2}$.

It can be seen that the values of D_p change with temperature in a trend opposite to the expected one. The blank tests (presented above) were also compared with the results obtained with these materials (Figure 39). The experimental curves, especially for higher temperatures overlap with the blank test, and the diffusivity coefficient can not be determined.

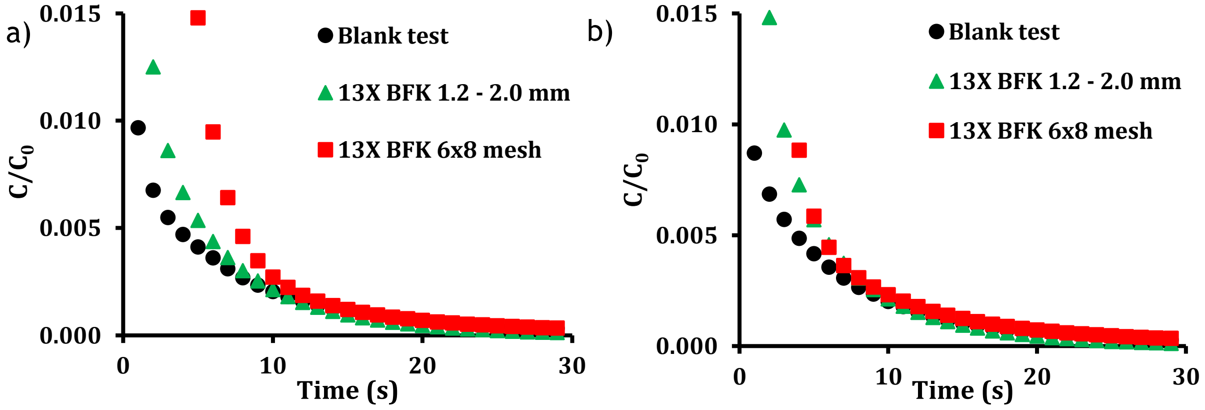

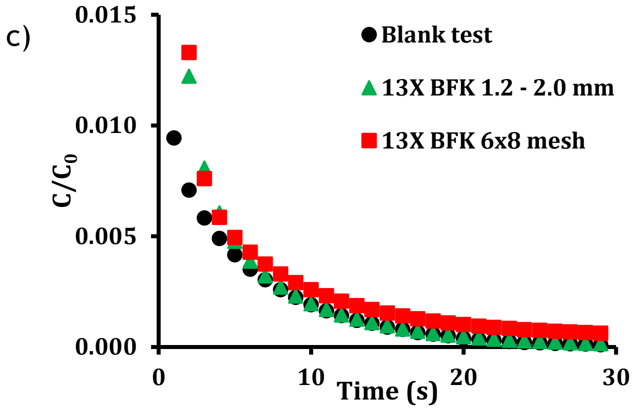

Figure 39- Comparison of the blank test with 13X zeolites for: a) 308 K, b) 343 K and c) 373 K and a 5.83 x 10^{-7} m^3 s^{-1} *in PTN conditions.*

5 Conclusions

In this work the adsorption of CO_2, CH_4 and N_2 in 4A BFK 2.5-5.0 mm, 4A BFK 1.6 – 2.5 mm, 4A BFK 1.6-2.5 mm HSD, 13X BFK 1.2-2.0 mm and 13X 6x8 mesh was studied. In order to characterize the materials, and therefore obtain useful information for adsorption equilibrium and adsorption kinetics properties, several properties were studied: the N_2 and CO_2 physisorption isotherms measured at 77 K and 273 K, respectively, mercury intrusion, Scanning Electron Micrograph (SEM), Energy Dispersive X-ray, and X-ray Diffraction (XRD).

The adsorption equilibrium isotherms were measured using a gravimetric method at 303, 343 and 373 K. The results show that the equilibrium of all 4A zeolites samples were equally well described by the same model which was expected since the three samples have the same type of crystals. From equilibrium results in terms of amount adsorbed per volume, due to the high density of the sample 4A BFK 1.6 – 2.5 mm HSD, less volume is necessary to have the same adsorption capacity of the other 4A samples. Also for 13X zeolites, the two samples presented the same adsorption equilibrium isotherms. In terms of affinity, CO_2 was the most adsorbed gas for both type of zeolites being the capacity of 13X higher. The least adsorbed gas was N_2 in 4A and 13X zeolites, being more adsorbed by the 13X zeolite. The experimental data was fitted using the Dual site Langmuir for the adsorption of CO_2 in 4A and One site Langmuir for the adsorption of CH_4 and N_2.

The kinetic study was done by the zero length column technique. The results showed that the micropore diffusion controls the mass transfer of CO_2 in 4A BFK 2.5 – 5.0 mm, 4A BFK 1.6 – 2.5 mm, in 13X BFK 1.2 – 2.0 mm and 13X BFK 6x8 mesh and also in of the case of CO_2 and CH_4 in 4A BFK 1.6 – 2.5 mm HSD. In terms of diffusion coefficient the N_2 has the highest value and CO_2 the lowest.

The use of the long time response to model the experimental ZLC results is justified by the direct calculation of the long time asymptote slope, which has the information of the adsorption kinetics. The initial part of the desorption curve may be affected by the washing of the cell and by dead volume effects that may hide the real diffusivity values. On the other hand, one of the main problems of the long time response is the dificulty in the determination of the range of points to be included [24]. Such a problem can lead to large differences in the value of the intercept resulting in low reproducibility of the method. [25]. In this study, the two approaches were used and it was concluded that the total solution was more reliable for the adsorption of CO_2 and CH_4 in 4A zeolite samples while the long time response provided the best fitting for 13X zeolite samples. The 4A BFK 1.6 -2.5 mm HSD was best fitted by the total solution for CO_2 and the long time response for the adsorption of CH_4.

It must be taken into attention that in order to avoid heat effects in ZLC experiments, the adsorbate concentration must be kept as small as possible [26]. However, at very high purge flow rates the effluent concentration can be very diluted for accurate measurement. Yet, one must keep in mind that the purge flow rate cannot be too much decreased, as the desorption equilibrium can became the controlling phenomenum [25]. According to Ruthven and Brandani, in order to properly apply this method it is necessary to allow the system to reach full equilibrium. When the L values is large (>10) the interpretation of an experimental ZLC desorption curve is trustworthy providing reliable values for diffusion [27]. In the experimental results ontained in this work, the average value of L for the CO_2 was 10^2 and for CH_4 10^1 indicating that difusivity results could be obtained for CO_2.

Concluding, 13X provides the highest loading capacity and the lowest isosteric heat of adsorption for CH_4, CO_2 and N_2 when compared to 4A zeolites.

6 Evaluation of the work done

6.1 Accomplished objectives

The objectives described in the introduction were accomplished however, due to the number of samples and the extent of the experiments the breakthrough curves could not be performed and therefore the diffusion coefficient of nitrogen in the zeolites could not be determined.

6.2 Limitations and future work

The main limitations of this work were the performance of the computer connected to the gas chromatographer and the control in the gravimetric balance of the lowest temperature (303 K) which required long periods of time to achieve isothermal conditions.

In terms of the procedure for the determination of the diffusion control, experiments with different pellet sizes were made. However, in future work, experiments with different inert gases and with different temperature range may also be an option to complement this evaluation. The blank tests should also be made at different temperatures.

6.3 Final appreciation

Adsorption plays an important and growing role in separation processes increasing the interest in studies in this field. In terms of experimental work it allowed enough contact time with the equipment to dominate the experimental procedure and fully understand how it works.

References

1. Saha, D., Z.B. Bao, F. Jia, and S.G. Deng, *Adsorption of CO2, CH4, N2O, and N-2 on MOF-5, MOF-177, and Zeolite 5A*. Environmental Science & Technology, 2010. **44**(5): p. 1820-1826.
2. Cavenati, S., C.A. Grande, and A.E. Rodrigues, *Adsorption Equilibrium of Methane, Carbon Dioxide, and Nitrogen on Zeolite 13X at High Pressures*. Journal of Chemical & Engineering Data, 2004. **49**(4): p. 1095-1101.
3. Leung, D.Y.C., G. Caramanna, and M.M. Maroto-Valer, *An overview of current status of carbon dioxide capture and storage technologies*. Renewable and Sustainable Energy Reviews, 2014. **39**: p. 426-443.
4. Brandani, F., D. Ruthven, and C.G. Coe, *Measurement of Adsorption Equilibrium by the Zero Length Column (ZLC) Technique Part 1: Single-Component Systems*. Industrial & Engineering Chemistry Research, 2003. **42**(7): p. 1451-1461.
5. Silva, J.A.C., Separation of n/iso-Paraffins by Adsorption Processes. Ph.D. Thesis, Universidade do Porto, 1998.
6. Hu, X., S. Brandani, A.I. Benin, and R.R. Willis, *Development of a Semiautomated Zero Length Column Technique for Carbon Capture Applications: Study of Diffusion Behavior of CO2in MOFs*. Industrial & Engineering Chemistry Research, 2015. **54**(21): p. 5777-5783.
7. Kulprathipanja, S., *Zeolites in industrial separation and catalysis*. 2010: John Wiley & Sons.
8. Sircar, S. and T.C. Golden, *Purification of Hydrogen by Pressure Swing Adsorption*. Separation Science and Technology, 2000. **35**(5): p. 667-687.
9. Alonso-Vicario, A., J.R. Ochoa-Gómez, S. Gil-Río, O. Gómez-Jiménez-Aberasturi, C.A. Ramírez-López, J. Torrecilla-Soria, and A. Domínguez, *Purification and upgrading of biogas by pressure swing adsorption on synthetic and natural zeolites*. Microporous and Mesoporous Materials, 2010. **134**(1-3): p. 100-107.
10. Ko, D., R. Siriwardane, and L.T. Biegler, *Optimization of a pressure-swing adsorption process using zeolite 13X for CO2 sequestration*. Industrial & Engineering Chemistry Research, 2003. **42**(2): p. 339-348.
11. Silva, F.A.D. and A.E. Rodrigues, *Propylene/propane separation by vacuum swing adsorption using 13X zeolite*. AIChE journal, 2001. **47**(2): p. 341-357.
12. Ruthven, D.M., *Principles of adsorption and adsorption processes*. 1984: John Wiley & Sons.
13. Ruthven, D.M. and Z. Xu, *Diffusion of oxygen and nitrogen in 5A zeolite crystals and commercial 5A pellets*. Chemical engineering science, 1993. **48**(18): p. 3307-3312.
14. Brandani, S., *Analytical solution for ZLC desorption curves with bi-porous adsorbent particles*. Chemical engineering science, 1996. **51**(12): p. 3283-3288.
15. Silva, J.C. and A.E. Rodrigues, *Analysis of ZLC technique for diffusivity measurements in bidisperse porous adsorbent pellets*. Gas separation & purification, 1996. **10**(4): p. 207-224.
16. Pavlov, M.L., O.S. Travkina, and B.I. Kutepov, *Grained binder-free zeolites: Synthesis and properties*. Catalysis in Industry, 2012. **4**(1): p. 11-18.

17. *Chemical structure*. Available from: chemicalstructure.net.

18. Association, S.C.o.t.I.Z., *Database of Zeolite Structures*. 2017.

19. Moreira, M.A., A.M. Ribeiro, A.F.P. Ferreira, and A.E. Rodrigues, *Cryogenic pressure temperature swing adsorption process for natural gas upgrade*. Separation and Purification Technology, 2017. **173**: p. 339-356.

20. Sircar, S., R. Mohr, C. Ristic, and M. Rao, *Isosteric heat of adsorption: theory and experiment*. The Journal of Physical Chemistry B, 1999. **103**(31): p. 6539-6546.

21. Romero-Pérez, A. and G. Aguilar-Armenta, *Adsorption kinetics and equilibria of carbon dioxide, ethylene, and ethane on 4A (CECA) zeolite*. Journal of Chemical & Engineering Data, 2010. **55**(9): p. 3625-3630.

22. Harper, R., G. Stifel, and R. Anderson, *Adsorption of gases on 4A synthetic zeolite*. Canadian Journal of Chemistry, 1969. **47**(24): p. 4661-4670.

23. Freitas, F.A.d.S., Cyclic Adsorption Processes: Application to Propane/Propylene Separation. Ph. D. Thesis, University of Porto, 1999.

24. Grande, C.A., Propane/Propylene Separation by Adsorption Processes. Ph.D. Thesis, University of Porto, 2004.

25. Loos, J.-B.W.P., P.J.T. Verheijen, and J.A. Moulijn, *Improved estimation of zeolite diffusion coefficients from zero-length column experiments*. Chemical Engineering Science, 2000. **55**(1): p. 51-65.

26. Brandani, S., C. Cavalcante, A. Guimarães, and D. Ruthven, *Heat effects in ZLC experiments*. Adsorption, 1998. **4**(3-4): p. 275-285.

27. Brandani, S. and D.M. Ruthven, *Analysis of ZLC desorption curves for gaseous systems*. Adsorption, 1996. **2**(2): p. 133-143.

28. Dubinin, M.M., *Theory of the physical adsorption of gases and vapors and adsorption properties of adsorbents of various natures and porous structures*. Bulletin of the Academy of Sciences of the USSR, Division of chemical science, 1960. **9**(7): p. 1072-1078.

29. Al-Baghli, N.A. and K.F. Loughlin, *Adsorption of methane, ethane, and ethylene on titanosilicate ETS-10 zeolite*. Journal of Chemical & Engineering Data, 2005. **50**(3): p. 843-848.

Appendix 1 Helium pycnometries

One helium pycnometry was performed for the system constituted by the basket, the permanent magnet and the suspension shaft, and four helium pycnometries were performed with the same system but also with the activated zeolite samples in study. They are represented in Figures A1.1 and A1.2.

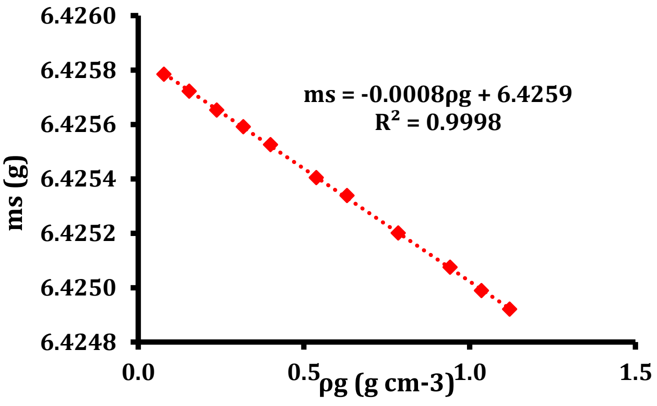

Figure A1.1- Helium pycnometry for the system with the basket, permanent magnet and suspension shaft.

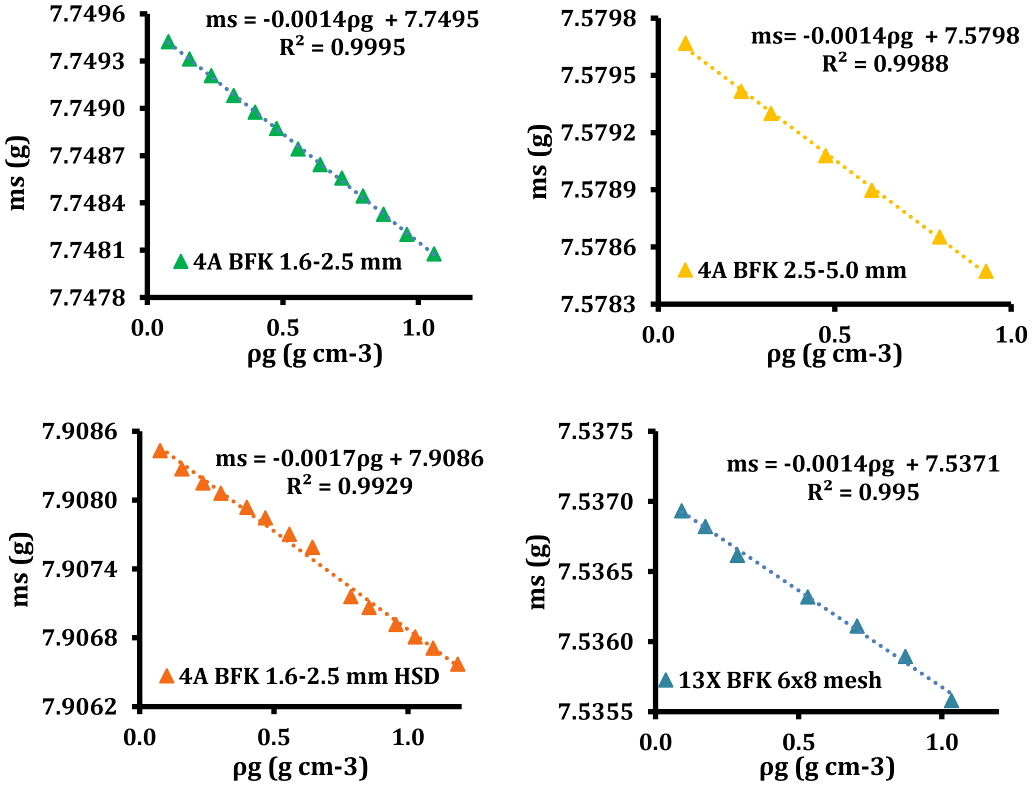

Figure A1.2- Helium pycnometry of the system with the basket, permanente magnet, suspension shaft and adsorbents.

Appendix 2 Liquid densities

According to Dubinin [28], for relatively low temperatures, the molar volume of the substance in the adsorbed state, v^*, may be taken as the molar volume of the substance in the bulk liquid phase..

Over the range of temperatures from the boiling point to the critical temperature, there is a considerable decrease in the liquid phase density as the critical temperature is approached (Figure A2.1). However, there's also a sharp increase in the compressibility of the liquid and since an adsorbed substance in micropores is in a strongly compressed state, its density is considerable greater than the liquid density and can be expressed as linear (line BD).

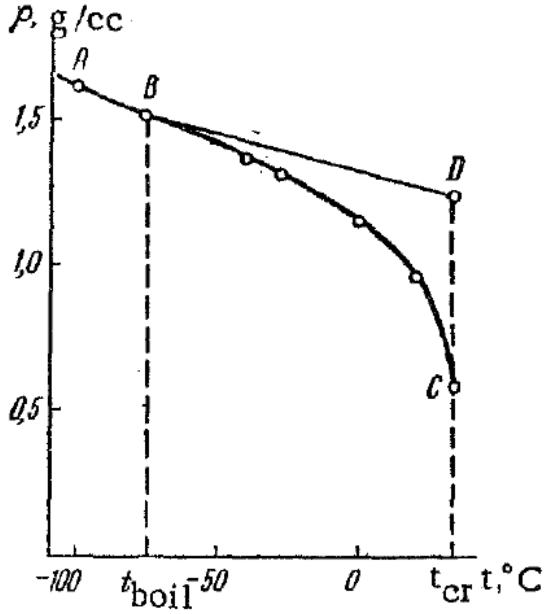

Figure A2. 1- Temperature dependence of the density of liquid tetrafluoroethylene REF.

Therefore, above boiling point temperature and under the critical temperature, the molar volume is calculated throught Equation A1.1 [29].

$$v^* = v_b + \left[\frac{T-T_b}{T_c-T_b}\right](b - v_b) \qquad \text{(Equation A1.1)}$$

where v_b is the molar volume at the boiling temperature, T_b, and T_c the critical temperature.

For temperatures above the critical temperature, the molar volume is equal to the Van der Waal's volume:

$$v^* = b \qquad \text{(Equation A1.2)}$$

where b is the Van der Waal's volume.

A vba code for the calculation of the molar volume was used as follows:

```
Function calcVMOL2(COMP As String, T As Double) As Double
        Dim TC As Double, Vb As Double, Tb As Double, b As Double
Select Case (UCase(COMP))
        Case ("CH4")
                ' METHANE - Prausnitz
                Tb = 111.66 'YAWS
                 b = 43.01 'YAWS
                 Vb = 38.47 'Yaws
        Case ("CO2")
                ' CO2 - Prausnitz
                Tb = 194.67 'Yaws
                 b = 42.86   'Yaws
                 Vb = 37.68 'Yaws
        Case ("N2")
                ' N2 - Prausnitz
                 Tb = 77.35 'Yaws
                b = 38.7 'Yaws
                Vb = 34.78 'Yaws
        Case Default
                A = MsgBox("Erro@getTDdata - gás inválido")
        End
End Select
        TC = getTC(COMP)
        PC = getPC(COMP)

                If T > TC Then
                        calcVMOL2 = b
                ElseIf T < TC Then
                        calcVMOL2 = Vb + ((T - Tb) / (TC - Tb)) * (b - Vb)
                End If
End Function

Function LiqDensity2(COMP As String, T As Double) As Double
'g/cm3
        LiqDensity2 = MM(COMP) / calcVMOL2(COMP, T)
End Function
```

Appendix 3 SEM

4A BFK 2.5-5.0 mm

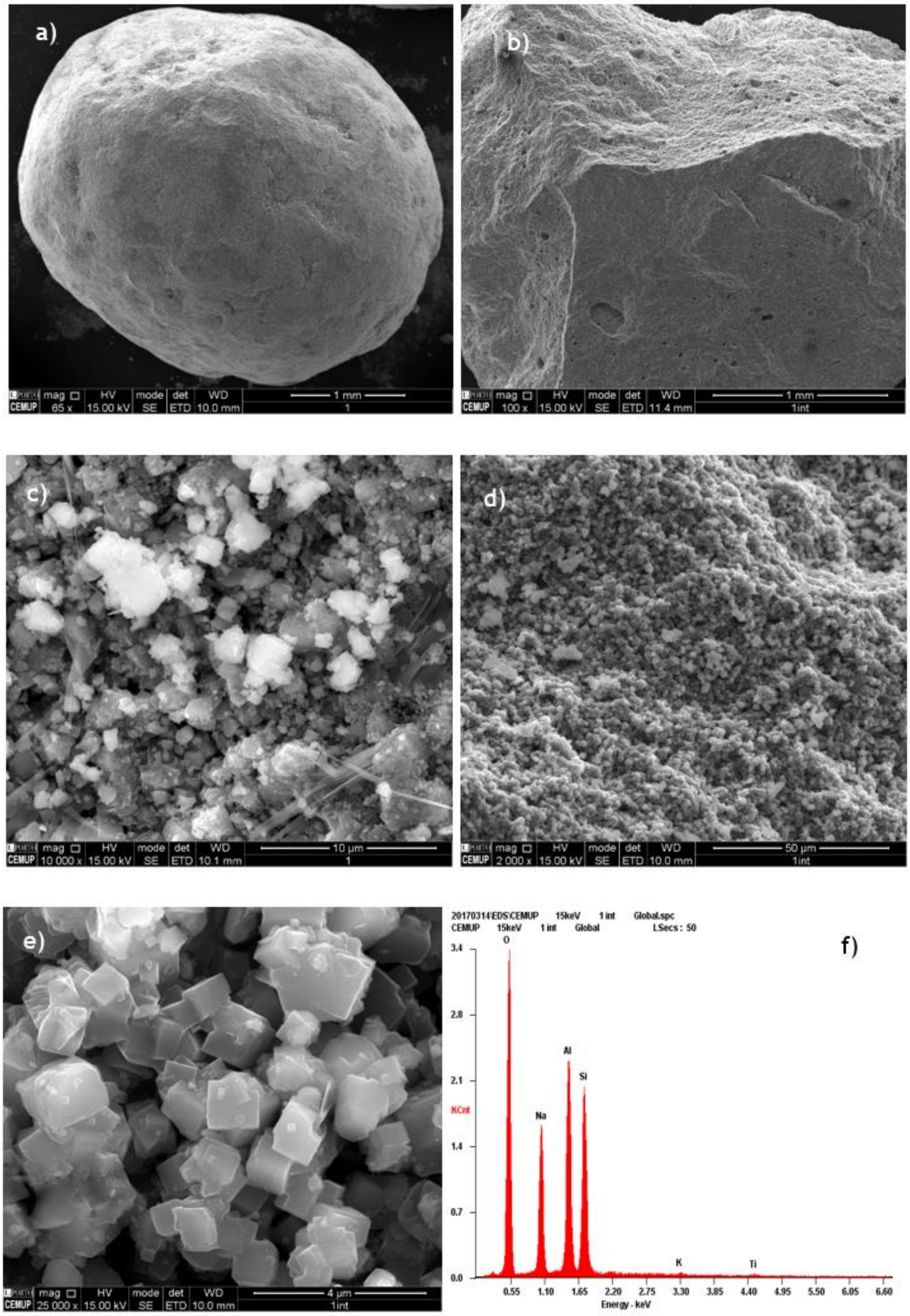

Figure A3. 1- SEM images of zeolite 4A BFK 2.5-5.0 mm: a) pellet, b) surface interface, c) surface exterior, d) surface interior, e) crystals, f) EDS spectra.

4A BFK 1.6-2.5 mm

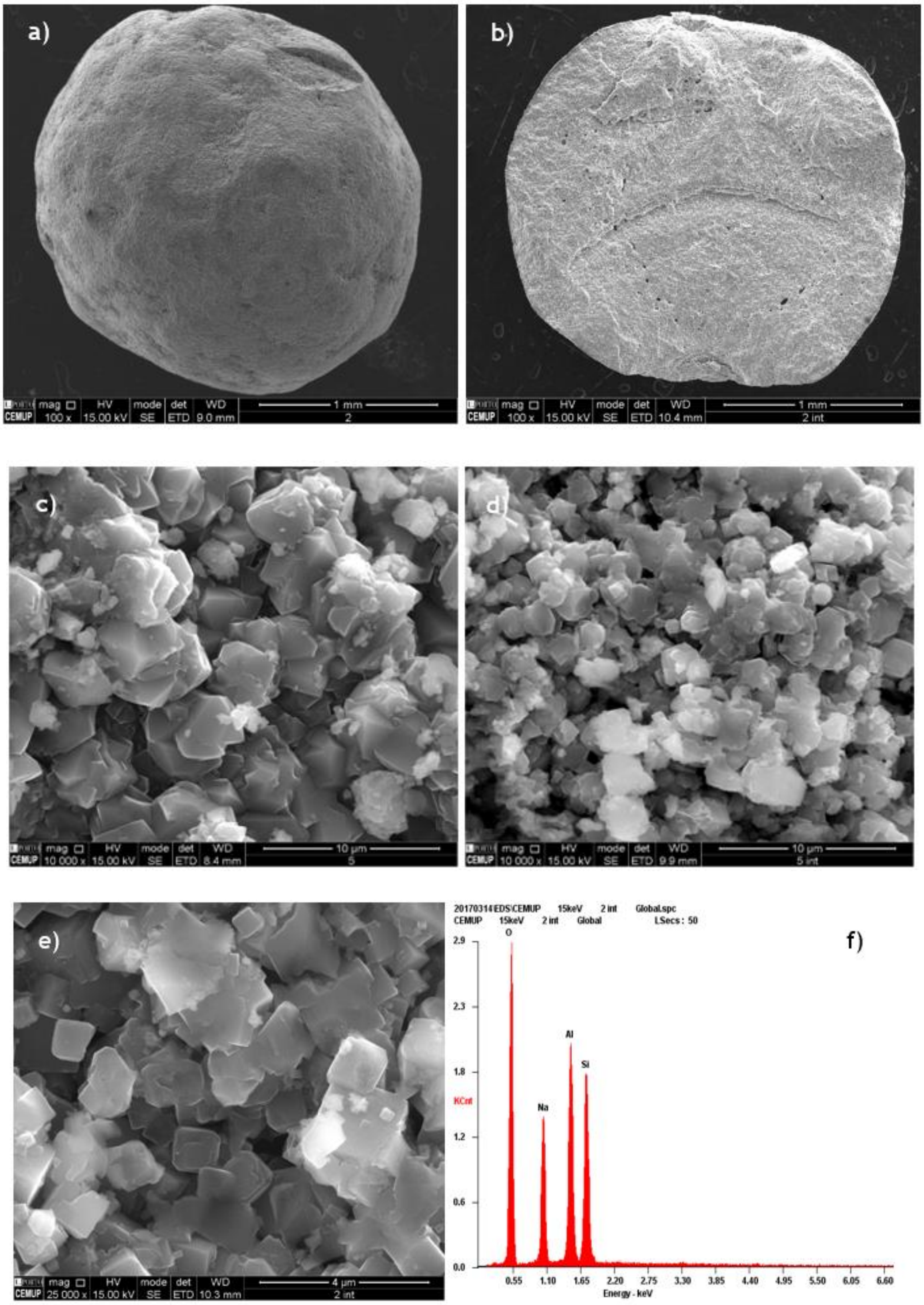

Figure A3.2- SEM images of zeolite 4A BFK 1.6-2.5 mm: a) pellet, b) surface interface, c) surface exterior, d) surface interior, e) crystals, f) EDS spectra.

4A BFK 1.6-2.5 mm HSD

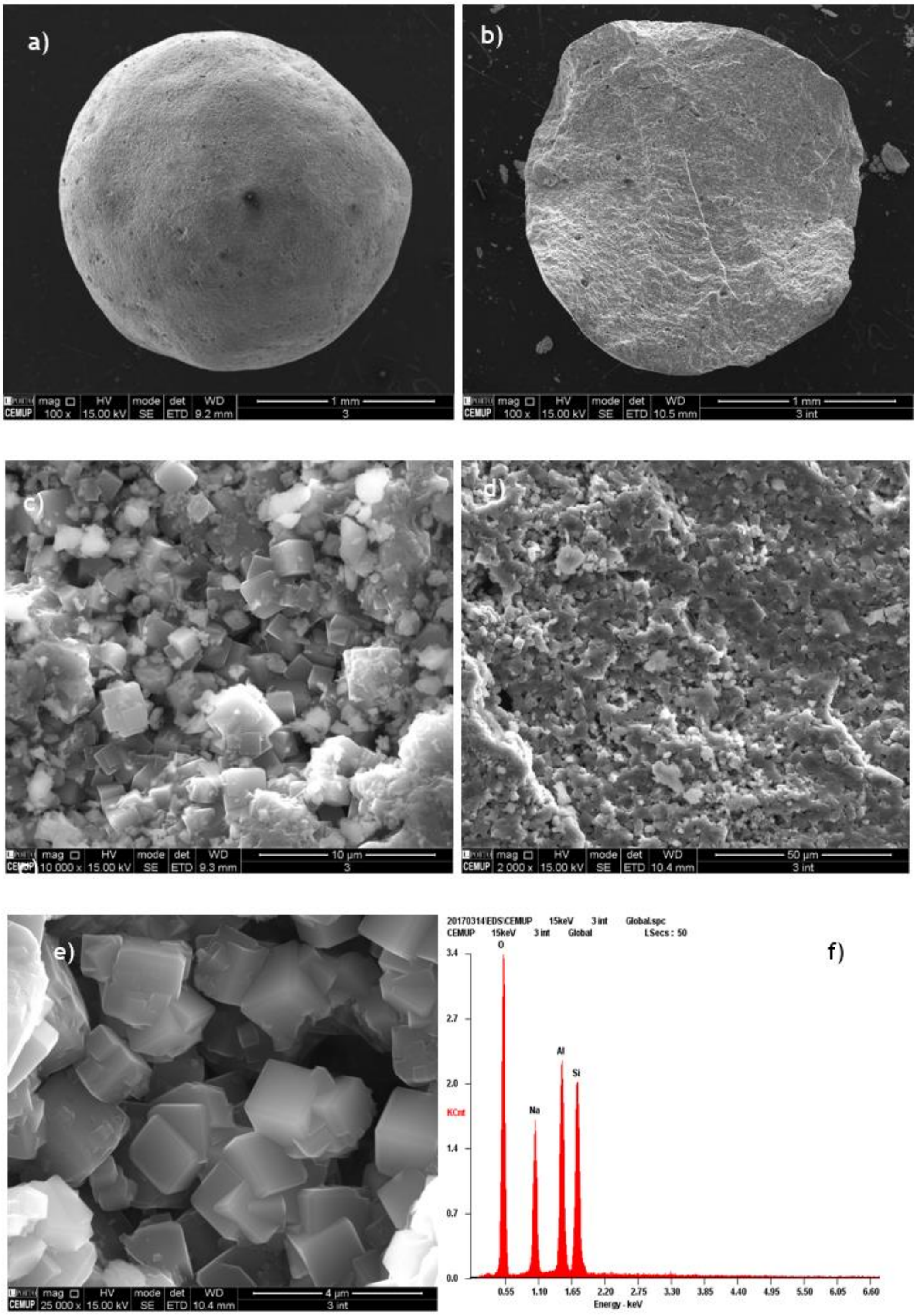

Figure A3.3- SEM images of zeolite 4A BFK 1.6-2.5 mm HSD: a) pellet, b) surface interface, c) surface exterior, d) surface interior, e) crystals, f) EDS spectra.

13X BFK 1.2-2.0 mm

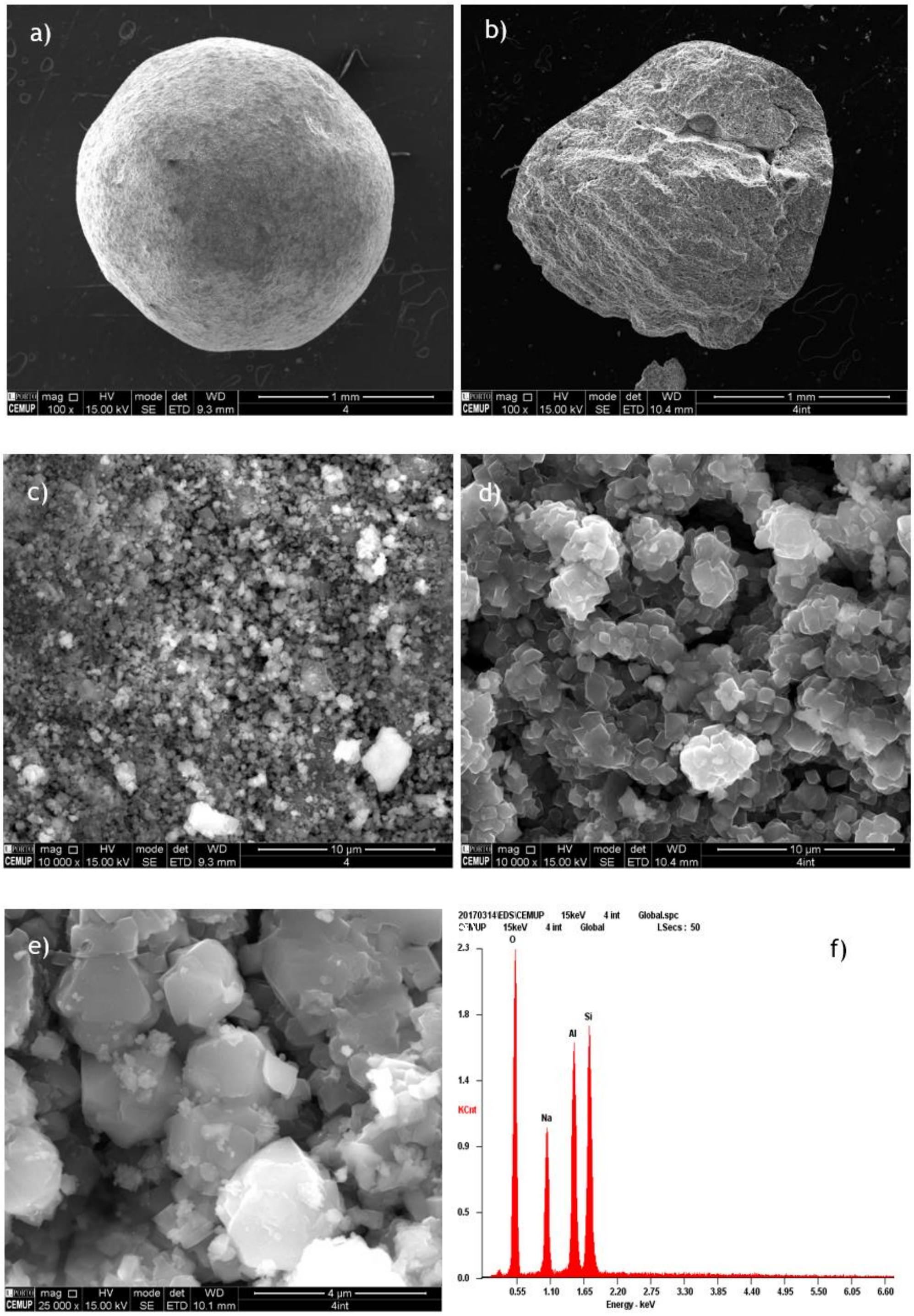

Figure A3.4- SEM images of zeolite 13X BFK 1.2-2.0 mm: a) pellet, b) surface interface, c) surface exterior, d) surface interior, e) crystals, f) EDS spectra.

13X BFK 6x8 mesh

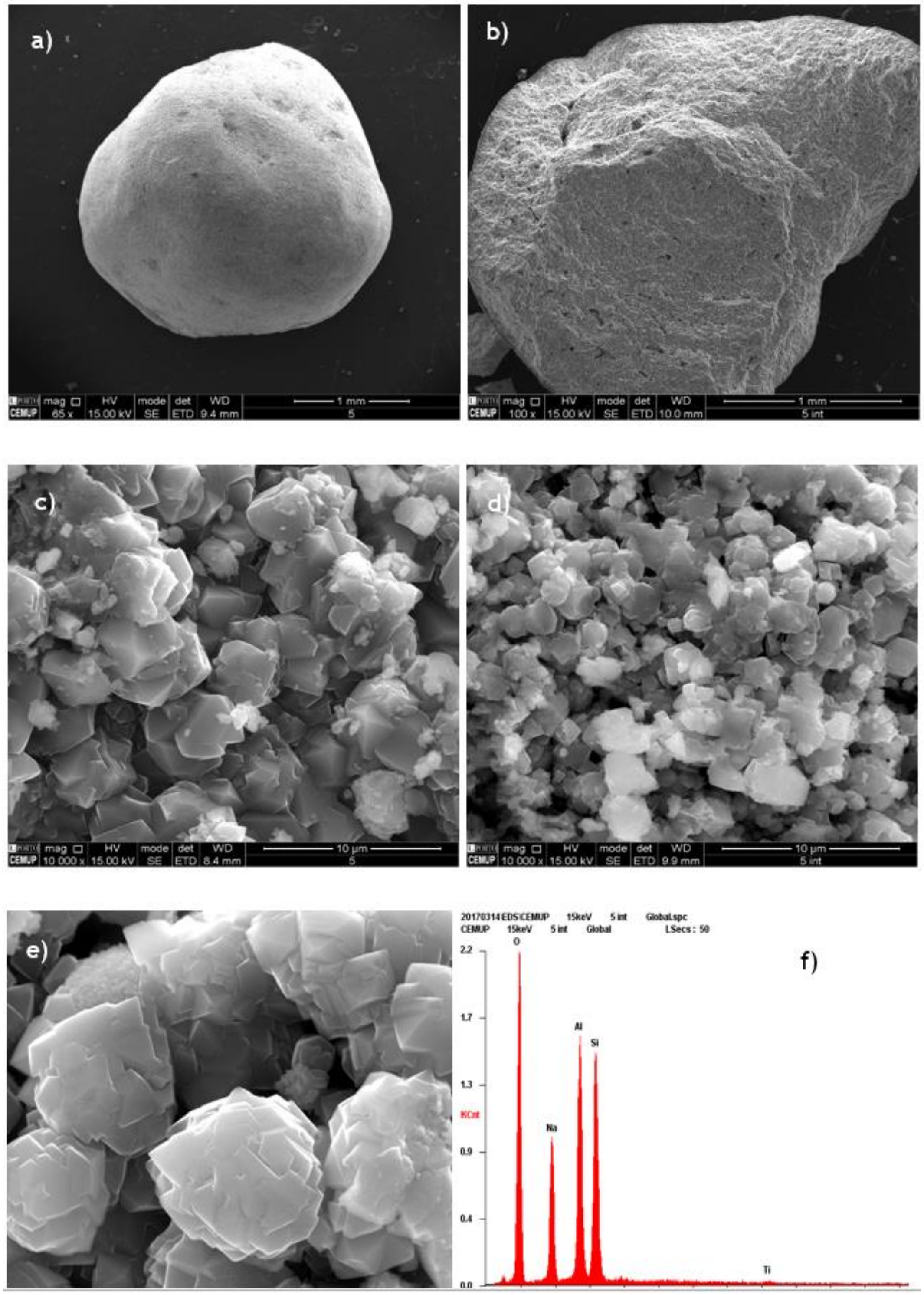

Figure A3.5- SEM images of zeolite 13X BFK 6x8 mesh: a) pellet, b) surface interface, c) surface exterior, d) surface interior, e) crystals, f) EDS spectra.

Appendix 4 Isotherms of 4A and 13X zeolites

Isotherms of zeolites 4A BFK 1.6-2.5 mm HSD, 4A BFK 2.5-5.0 mm

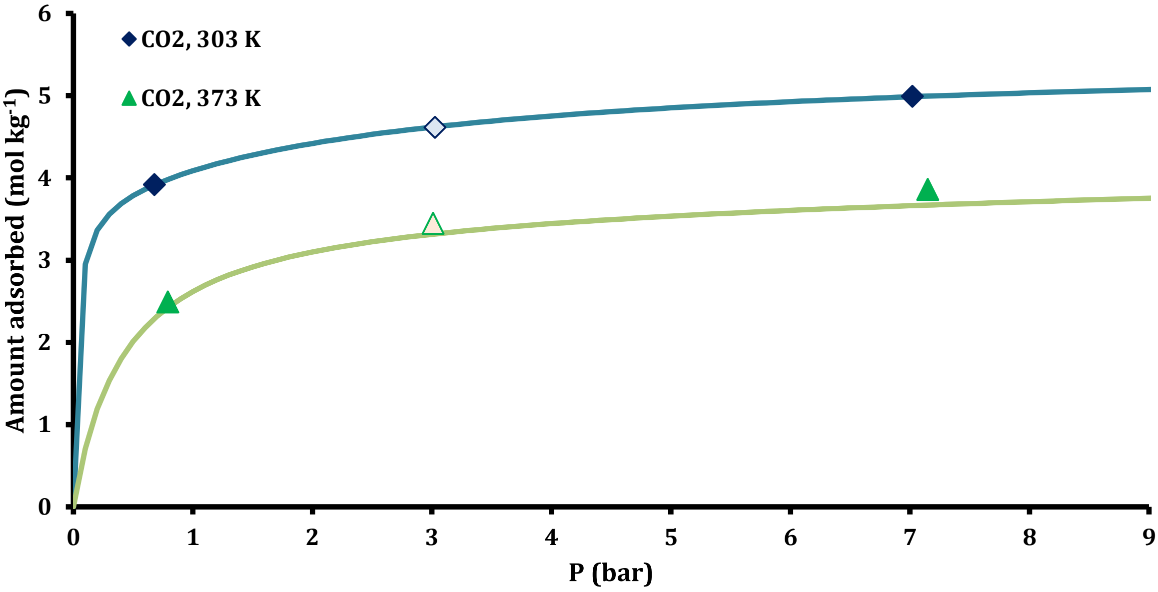

Figure A4.1- Amount of CO_2 adsorbed on 4A BFK 1.6-2.5 mm HSD zeolite: experimental points (closed adsorption, open desorption) at 303, 373 K and Langmuir Dual-site fitting for CO_2 in 4A BFK 1.6-2.5 mm zeolite. An agreement between the data is observed.

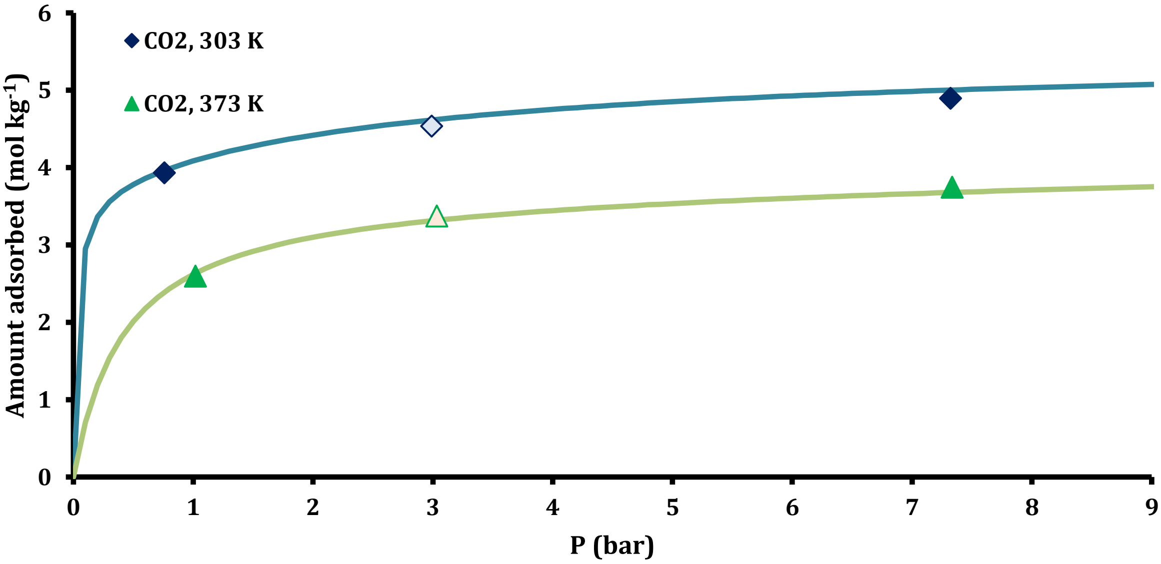

Figure A4.2- Amount of CO_2 adsorbed on 4A BFK 2.5-5.0 mm zeolite: experimental points (closed adsorption, open desorption) at 303, 373 K and Langmuir Dual-site fiiting for CO_2 in 4A BFK 1.6-2.5 mm zeolite. An agreement between the data is observed.

Isotherms of 13X BFK 6x8 mesh and 13X BFK 1.2 – 2.0 mm

A previous study [19] performed in LSRE on the zeolite 13X BFK 1.2-2.0 mm was performed. The zeolite properties are shown in Table A4.1.

Table A4.1- Properties of the 13X BFK 1.2-2.0 mm zeolite.

Adsorbent properties		Units
Shape	Beads	-
Particle diameter	1.2-2.0	mm
Average crystal diameter	2	μm
Apparent particle density	1072	kg m^{-3}
Particle porosity	0.39	-

According to the study, the experimental adsorption equilibrium results were best fitted with Dual site Langmuir model and given the large temperature range, a temperature dependence of the equilibrium parameters was required (Equations A4.1- A4.3).

$$q_i = q_{sat,1}\frac{b_1 P}{1+b_1 P} + q_{sat,2}\frac{b_2 P}{1+b_2 P} \qquad \text{(Equation A4.1)}$$

$$b = b_0 exp\left(\frac{-\Delta H}{R_g T}\right) \qquad \text{(Equation A4.2)}$$

$$q_{sat} = q_0 exp\left[\chi\left(1-\frac{T}{T_0}\right)\right] \qquad \text{(Equation A4.3)}$$

Where q_i is the adsorbed phase concentration, q_{sat} the saturation capacity, b the affinity constant, P the partial pressure, b_0 the affinity at infinite temperature, T_0 the reference temperature and χ is a constant parameter.

The equilibrium parameters of the Dual-site Langmuir are given in Table A4.2.

Table A4.2- Parameters of the Dual-Site Langmuir isotherm for binderless zeolite 13X beads

Parameter	CH_4	CO_2	Units
$\boldsymbol{b_{1,0}}$	2.9 x 10^{-4}	4.1 x 10^{-4}	bar^{-1}
$\boldsymbol{b_{2,0}}$	1.4 x 10^{-5}	1.3 x 10^{-5}	bar^{-1}
$-\Delta \boldsymbol{H_1}$	15.8	23.0	kJ/mol
$-\Delta \boldsymbol{H_2}$	1.9	19.0	kJ/mol
$\boldsymbol{q_{1,0}}$	3.47	5.78	mmol/g
$\boldsymbol{q_{2,0}}$	23.6	1.16	mmol/g

χ_1	0.90	0.51	-
χ_2	0.002	0.23	-
T_0	473		K

The experimental points obtained in this work for 13X BFK 6x8 mesh zeolite and the model of the Dual-site Langmuir are presented in Figure A4.3.

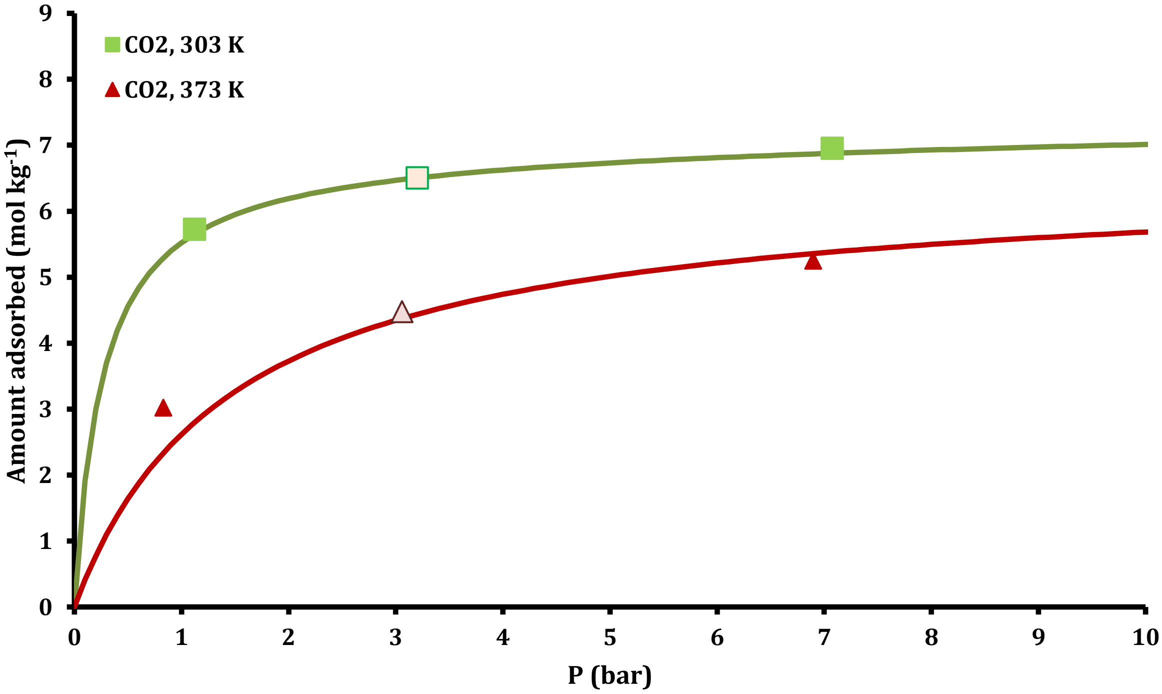

Figure A4.3- Amount of CO_2 adsorbed on 13X BFK 6x8 mesh zeolite: experimental points (closed adsorption, open desorption) at 303, 373 K and Dual-site Langmuir fiiting for CO_2 in 13X BFK 1.2-2.0 mm zeolite. An agreement between the data is observed.

Isotherms of CO_2, CH_4 and N_2 at 303, 343 and 373 K in 4A and 13X zeolite samples in terms of amount adsorved per volume of adsorbent.

According to the previous equilibrium and kinetics studies the main difference between the 4A zeolites is that the high density 4A achieves the same results with less volume of adsorbate. The amount adsorbed per volume as function of pressure is presented in the following figures.

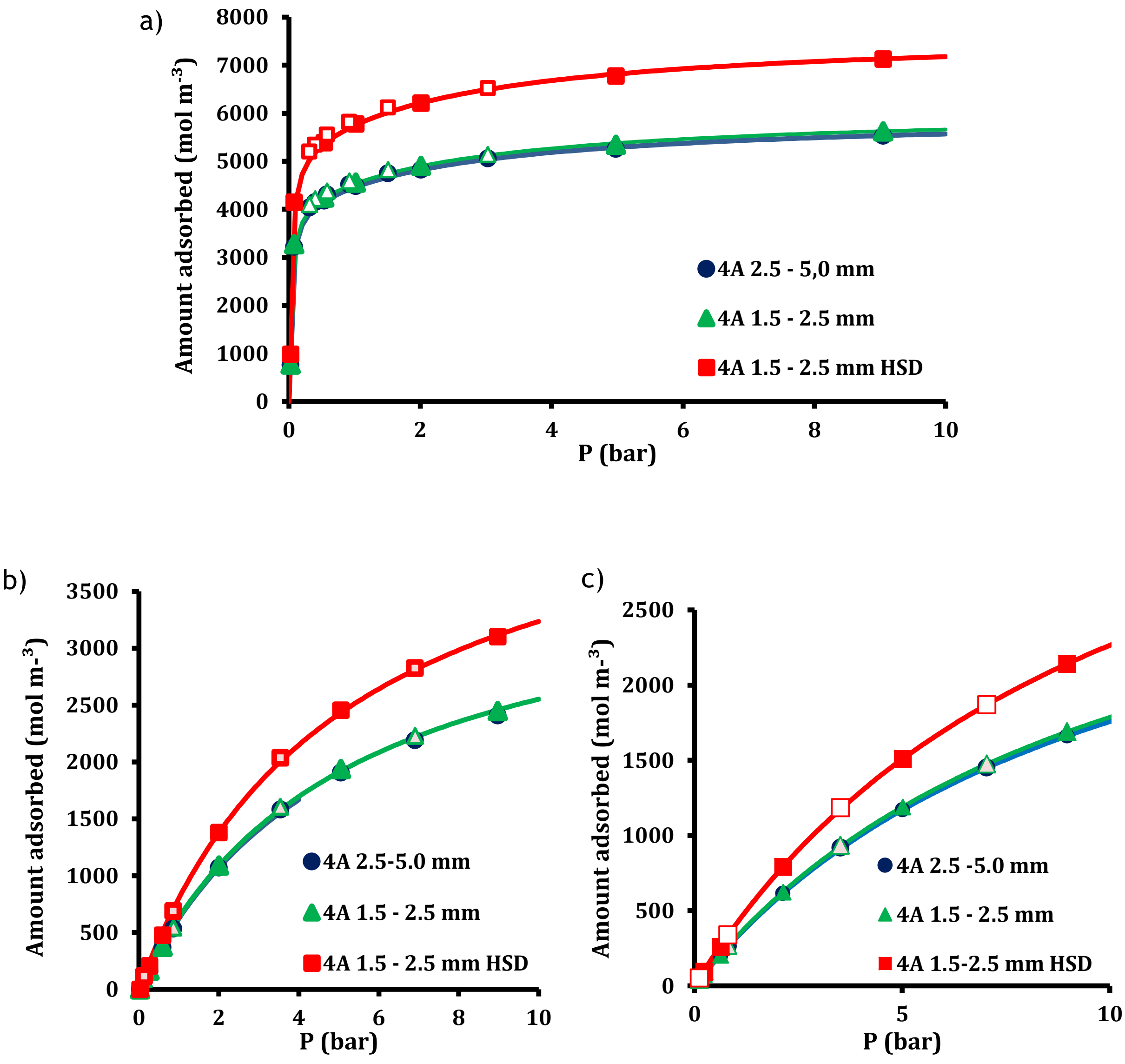

Figure A4.4- Amount of a) CO_2, b) CH_4 and c) N_2 adsorbed per volume of adsorbant on 4A zeolites: experimental points (closed adsorption, open desorption) at 303 K and Dual-site or Single site Langmuir fitting in 4A BFK 1.6-2.5 mm zeolite.

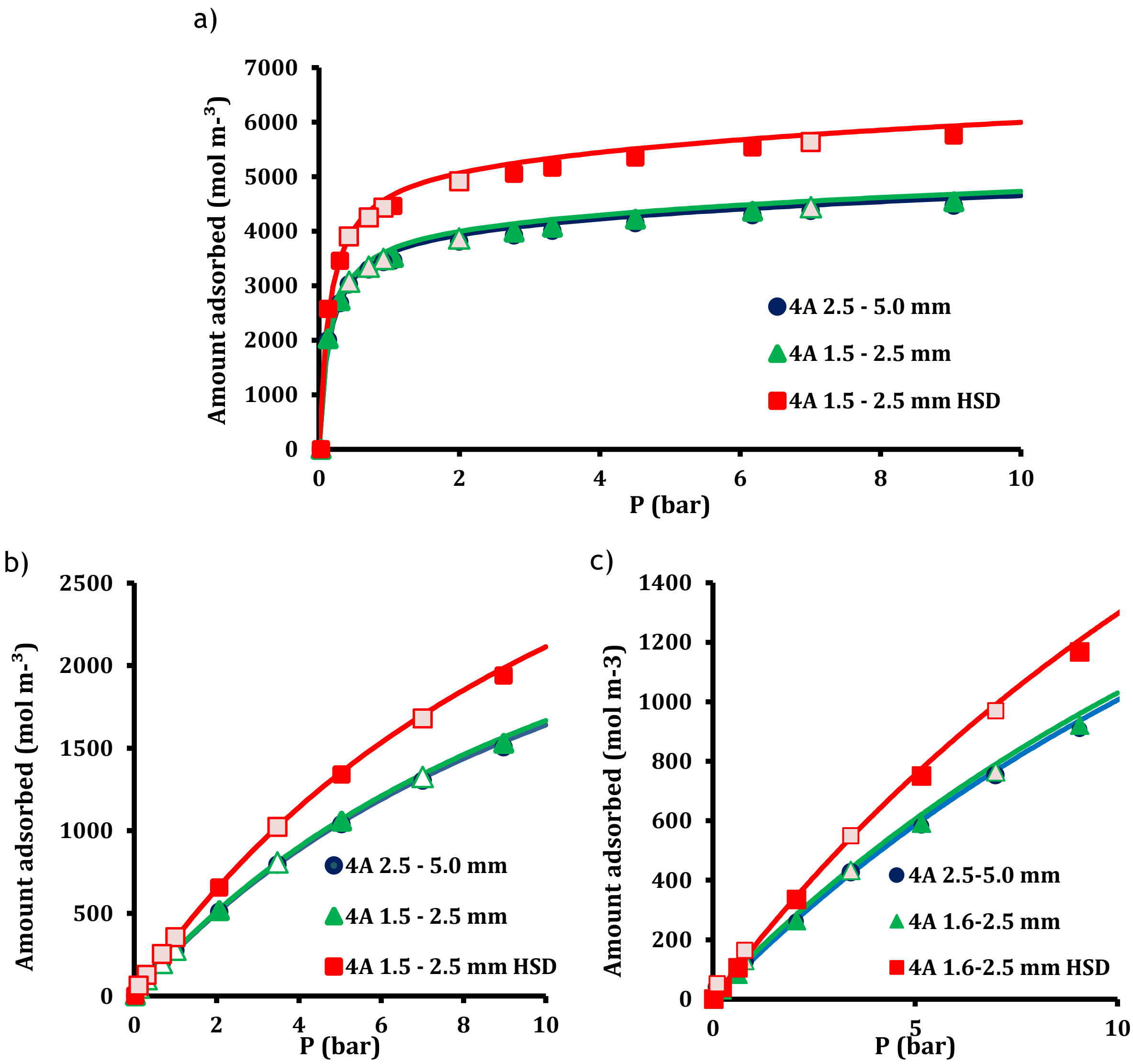

Figure A4.5- Amount of a) CO_2, b) CH_4 and c) N_2 adsorbed per volume of adsorbant on 4A zeolites: experimental points (closed adsorption, open desorption) at 343 K and Dual-site Langmuir fiiting for CO_2 in 4A BFK 1.6-2.5 mm zeolite.

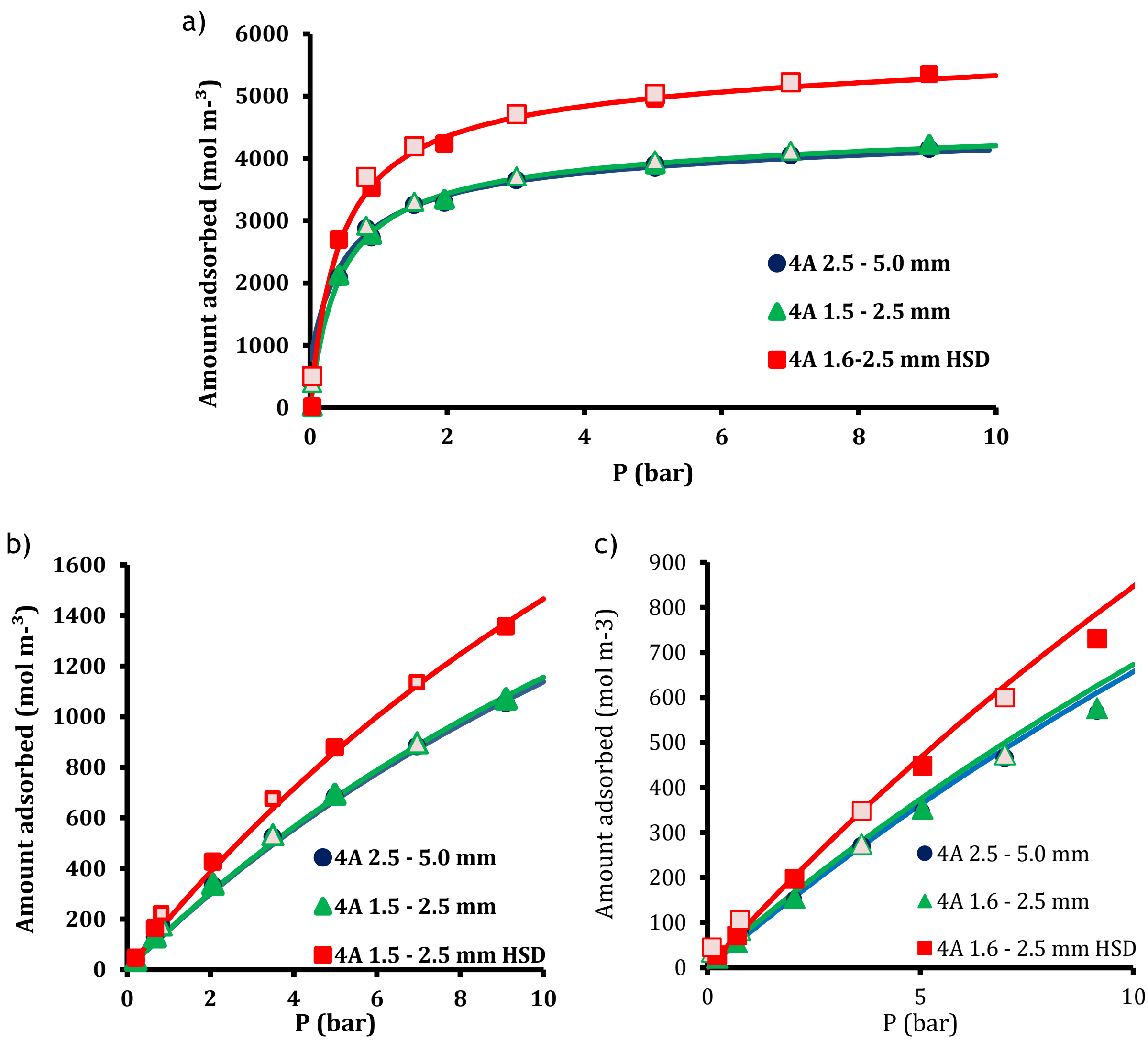

Figure A4.6- Amount of a) CO_2, b) CH_4 and c) N_2 adsorbed per volume of adsorbant on 4A zeolites: experimental points (closed adsorption, open desorption) at 373 K and Dual-site Langmuir fiiting for CO_2 in 4A BFK 1.6-2.5 mm zeolite.

Appendix 5 Calibration of the volumetric flow rate of the Gas Chromatographer

In order to convert the arbitrary units of the gas chromatographer flow rate indicator to cubic centimeters per second a calibration was made. The volumetric flow rate at 1 bar and 273 K is presented in Figure A5.1.

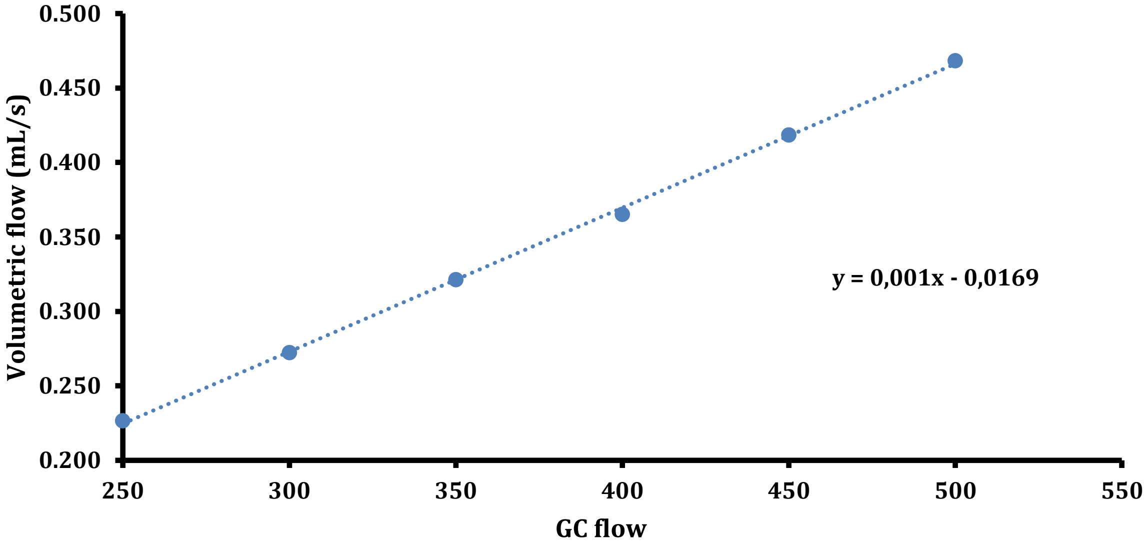

Figure A5.1- Calibration of the flow of the gas chromatographer in PTN conditions.

Appendix 6 ZLC columns

The zero length columns were prepared using swagelok connections. Fiber glass wool was included in each end of the column in order to properly hold the pellets and prevent release of fines to the GC detectors. In each column all the pellets have the same diameter carefully measured previously.

Table A6.1- Caracteristics of the ZLC columns.

	Units	**Column 1**	**Column 2**	**Column 3**	**Column 4**	**Column 5**
Zelite		4A BFK 2.5 – 5.0 mm	4A BFK 1.6 – 2.5 mm	4A BFK HSD 1.6-2.5 mm	13X BFK 1.2-2.0 mm	13X BFK 6x8 mesh
Number of pellets		2	9	9	10	3
Pellet diameter	cm	0.4	0.2	0.2	0.2	0.3
Column volume	cm^3	0.118	0.114	0.092	0.079	0.095
Porosity		0.43	0.67	0.59	0.47	0.55
Dry Zeolite mass in ZLC column	g	0.0685	0.0442	0.0510	0.0338	0.0353

Appendix 7 ZLC results

Experimental results in each ZLC column

ZLC experiments with zeolites: 4A BFK 2.5 – 5.0 mm, 4A BFK 1.6 -3.5 mm, 4A BFK 1.6 – 2.5 mm HSD, 13X BFK 1.2 – 2.0 mm and 13X BFK 6x8 mesh; with CO_2 and CH_4 as adsorbates at 308, 323, 343 and 373 K at different flow rates.

- **Experimental results in zeolite 4A BFK 2.5 – 5.0 mm**

Table A7.1- Long time response and the complete ZLC model parameters for CO_2 in 4A BFK 2.5 - 5.0 mm zeolite at 308, 323, 343 and 373 K.

T (K)	$Q \times 10^7$ ($m^3 s^{-1}$)	$Dap\, l^{-2} \times 10^{-4}$ (s^{-1})		K^*		L		β
		LTR	TS	LTR	TS	LTR	TS	LTR
308	5.28	4.21	1.07	232	470	27	52	3.03
323	5.54	3.42	3.17	353	332	23	26	3.00
343	5.88	6.96	6.47	266	255	16	18	2.95
373	6.39	19.1	17.3	147	143	11	13	2.87

Table A7.2- Long time response and the complete ZLC model parameters for CH_4 in 4A BFK 2.5 - 5.0 mm zeolite 308, 323, 343 and 373 K.

T (K)	$Q \times 10^7$ ($m^3 s^{-1}$)	$Dap\, l^{-2} \times 10^{-3}$ (s^{-1})		K^*		L		β
		LTR	TS	LTR	TS	LTR	TS	LTR
308	5.28	9.25	6.44	1	1	262	423	3.13
	6.58	9.50	6.14	1	1	242	416	3.13
323	6.90	8.98	5.14	2	2	217	411	3.13
	9.26	9.64	5.00	2	2	195	413	3.13
343	7.33	9.77	5.94	1	1	261	487	3.13
	9.84	9.55	6.27	2	2	245	420	3.13
373	10.70	10.3	6.06	3	2	197	380	3.13
	7.97	12.2	8.08	2	1	209	354	3.13

- **Experimental results in zeolite 4A BFK 1.6 – 2.5 mm**

Table A7.3 - Long time response and the complete ZLC model parameters for CO_2 *in 4A BFK 1.6 – 2.5 mm zeolite at 308, 323, 343 and 373 K.*

T (K)	***Q* x 10^{7} (m^{3} s^{-1})**	**Dap l^{-2} x 10^{-4} (s^{-1})**		**K^{*}**		**L**		***β***
		LTR	**TS**	**LTR**	**TS**	**LTR**	**TS**	**LTR**
308	4.72	3.95	3.95	1654	1654	6	6	2.68
	5.28	3.30	3.37	2222	2256	6	6	2.68
323	5.54	6.81	6.24	257	244	28	32	3.03
	6.90	5.35	5.08	323	311	35	39	3.05
343	5.88	31.0	27.2	93	87	18	22	2.97
373	6.39	54.3	49.8	78	74	13	15	2.91
	7.97	19.7	15.8	156	147	23	30	3.01

Table A7.4- Long time response and the complete ZLC model parameters for CH_4 *in 4A BFK 1.6 – 2.5 mm zeolite at 308, 323, 343 and 373 K.*

T (K)	***Q* x 10^{7} (m^{3} s^{-1})**	**Dap l^{-2} x 10^{-2} (s^{-1})**		**K^{*}**		**L**		***β***
		LTR	**TS**	**LTR**	**TS**	**LTR**	**TS**	**LTR**
308	5.28	1.23	1.06	2	2	170	218	3.12
	6.58	1.21	1.01	3	2	174	232	3.12
323	5.54	1.20	0.995	2	2	198	269	3.13
	6.90	1.24	1.04	3	3	170	222	3.12
343	7.33	1.18	0.886	3	3	186	284	3.12
	9.84	1.24	0.971	4	4	169	247	3.12
373	7.97	1.15	0.871	3	3	200	299	3.13
	10.70	1.24	0994	4	4	176	248	3.12

- **Experimental results in zeolite 4A BFK 1.6 – 2.5 mm HSD**

Table A7.5- Long time response and the complete ZLC model parameters for CO_2 in 4A BFK 1.6 – 2.5 mm HSD zeolite at 308, 323, 343 and 373 K.

T (K)	Q x 10^7 (m^3 s^{-1})	$Dap\ l^{-2}$ x 10^{-4} (s^{-1})		K^*		L		B
		LTR	TS	LTR	TS	LTR	TS	LTR
308	5.28	1.30	1.19	3144	3067	11	13	2.87
	6.58	1.28	1.23	2204	2121	21	22	2.99
323	6.90	2.51	0.80	342	387	71	197	3.10
343	4.03	48.5	41.3	43	39	17	22	2.96
	5.88	69.2	52.8	44	44	17	22	2.96
	7.33	4.74	35.3	50	46	27	40	3.03
373	7.97	14.9	12.7	129	119	37	47	3.06
	6.39	90.1	72.7	38	35	16	22	2.95

Table A7.6- Long time response and the complete ZLC model parameters for CH_4 in 4A BFK 1.6 – 2.5 mm HSD zeolite at 308, 323, 343 and 373 K.

T (K)	Q x 10^7 (m^3 s^{-1})	$Dap\ l^{-2}$ x 10^{-3} (s^{-1})		K^*		L		B
		LTR	TS	LTR	TS	LTR	TS	LTR
308	5.28	1.06	1.22	22	22	196	174	3.13
	6.58	1.03	1.11	31	30	183	178	3.12
	8.83	1.10	1.19	45	44	158	150	3.12
323	6.90	1.19	1.53	14	15	371	270	3.13
	5.54	1.34	1.90	10	10	366	248	3.13
343	9.84	3.32	4.83	6	9	430	204	3.13
	9.84	3.00	3.59	6	8	447	296	3.13
373	7.97	13.2	11.8	3	2	195	245	3.13
	10.70	13.8	12.6	6	5	123	145	3.12

- **Experimental results in zeolite 13X BFK 1.2 – 2.0 mm**

Table A7.7- Long time response and the complete ZLC model parameters for CO_2 in 13X BFK 1.2 – 2.0 mm zeolite at 308, 323, 343 and 373 K.

T (K)	*Q* x 10^7 (m^3 s^{-1})	*Dap* l^{-2} x 10^{-4} (s^{-1})		*K**		*L*		*β*
		LTR	TS	LTR	TS	LTR	TS	LTR
308	5.28	2.65	2.79	2693	2760	6	5	2.64
	6.58	3.04	3.07	2268	2317	8	7	2.75
323	5.54	3.30	5.97	286	316	47	23	3.07
	6.90	5.24	6.27	1102	1210	9	7	2.82
343	5.88	16.4	16.9	209	214	14	13	2.91
	7.33	7.55	7.75	328	334	23	22	3.01
373	6.39	62.8	61.4	136	135	6	6	2.65
	7.97	30.2	27.5	160	158	13	15	2.91
	7.97	68.4	66.5	133	131	7	7	2.71

Table A7.8- Long time response and the complete ZLC model parameters for CH_4 in 13X BFK 1.2 – 2.0 mm zeolite 308, 323, 343 and 373 K.

T (K)	*Q* x 10^7 (m^3 s^{-1})	*Dap* l^{-2} x 10^{-2} (s^{-1})		*K**		*L*		*β*
		LTR	TS	LTR	TS	LTR	TS	LTR
308	4.72	1.54	1.55	1	1	194	186	3.13
	6.58	1.49	1.53	2	2	218	208	3.13
	7.71	1.40	1.57	2	2	213	160	3.13
323	6.90	1.37	1.45	2	2	240	214	3.13
	8.08	1.44	1.45	2	2	223	214	3.13
343	5.88	1.72	1.71	2	2	164	154	3.12
	7.33	1.50	1.57	2	2	216	196	3.13
	8.58	1.62	1.64	2	2	188	179	3.12
373	7.97	1.45	1.46	2	2	248	241	3.13
	9.33	1.43	1.42	2	2	266	269	3.13
	10.70	1.48	1.47	2	2	238	240	3.13

- **Experimental results in zeolite 13X BFK 6x8 mesh**

Table A7.9- Long time response and the complete ZLC model parameters for CO_2 in 13X BFK 6x8 mesh zeolite at 308, 323, 343 and 373 K.

T (K)	$Q \times 10^7$ ($m^3\ s^{-1}$)	$Dap\ l^{-2} \times 10^{-4}$ (s^{-1})		K^*		L		β
		LTR	TS	LTR	TS	LTR	TS	LTR
308	6.58	1.57	1.64	4172	4765	8	7	2.76
	7.71	2.06	2.14	3059	3544	10	9	2.82
323	6.90	5.16	4.69	1786	1937	6	7	2.65
	8.08	5.15	4.65	1629	1744	8	9	2.75
343	7.33	4.97	7.17	213	289	54	31	3.08
	8.58	5.37	7.31	222	291	57	36	3.09
	9.84	7.50	10.3	211	291	49	29	3.08
373	7.97	16.9	19.4	172	206	22	18	3.00
	9.33	20.4	21.7	168	197	21	19	3.00
	10.70	13.6	15.5	171	209	36	29	3.06

Table A7.10- Long time response and the complete ZLC model parameters for CH_4 in 13X BFK 6x8 mesh zeolite at 308, 323, 343 and 373 K.

T (K)	$Q \times 10^7$ ($m^3\ s^{-1}$)	$Dap\ l^{-2} \times 10^{-2}$ (s^{-1})		K^*		L		β
		LTR	TS	LTR	TS	LTR	TS	LTR
308	4.72	1.09	0.958	1	1	309	407	3.13
	8.83	1.06	0.973	2	2	318	362	3.13
	9.96	1.01	1.01	2	2	335	306	3.13
323	9.26	0.981	1.14	2	2	376	303	3.13
	8.08	0.965	1.25	2	2	408	266	3.13
	10.45	0.949	1.06	2	3	367	307	3.13
343	5.88	1.00	1.11	1	1	404	340	3.13
	7.33	1.01	1.11	2	2	357	303	3.13
	8.58	1.09	1.07	2	2	306	318	3.13
	9.84	1.06	1.22	2	3	303	253	3.13
373	7.97	1.03	1.02	2	2	273	298	3.13
	9.33	1.21	1.13	2	3	249	284	3.13
	10.70	1.49	1.45	3	3	221	235	3.13
	12.06	1.17	1.16	3	4	238	249	3.13

Comparison of experiments with the same flow rate and temperature but different zeolite

- CO_2 in 4A zeolites

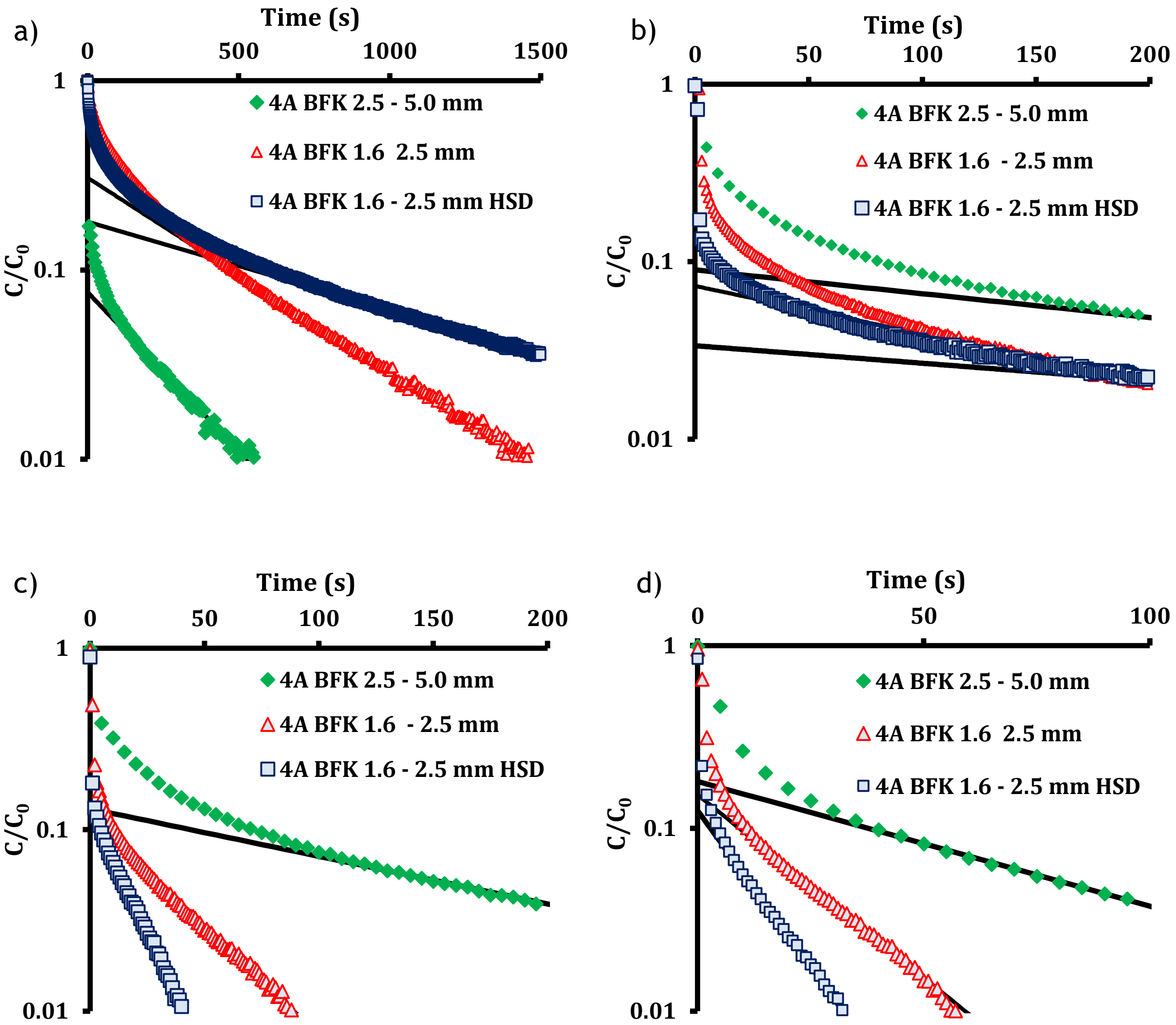

Figure A7.1- Experimental results and long-time response for CO_2 in different 4A BFK zeolites, at: a) 303 K and 5.28 x 10^{-7} m^3 s^{-1}, b) 323 K and 5.54 x 10^{-7} m^3 s^{-1}, c) 343 K and 5.88 x 10^{-7} m^3 s^{-1} and d) 373 K and 6.39 x 10^{-7} m^3 s^{-1}.

- CO_2 in 13X zeolites

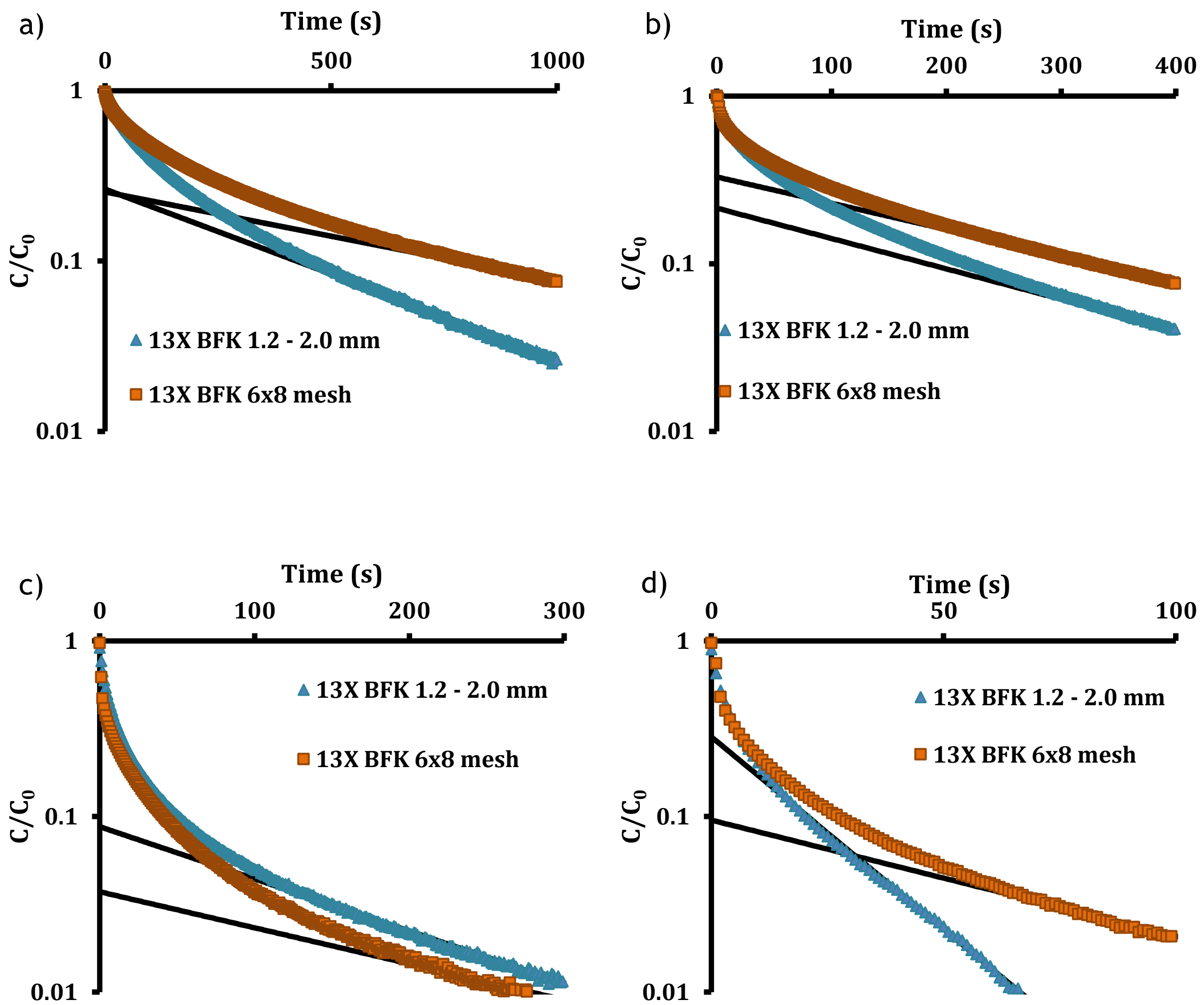

Figure A7.2- Experimental results and long-time response for CO_2 in different 13X BFK zeolites, at: a) 303 K and 5.28 x 10^{-7} m^3 s^{-1}, b) 323 K and 6.90 x 10^{-7} m^3 s^{-1}, c) 343 K and 7.33 x 10^{-7} m^3 s^{-1} and d) 373 K and 7.97 x 10^{-7} m^3 s^{-1}.

- Adsorbate: CH_4 in 4A zeolites

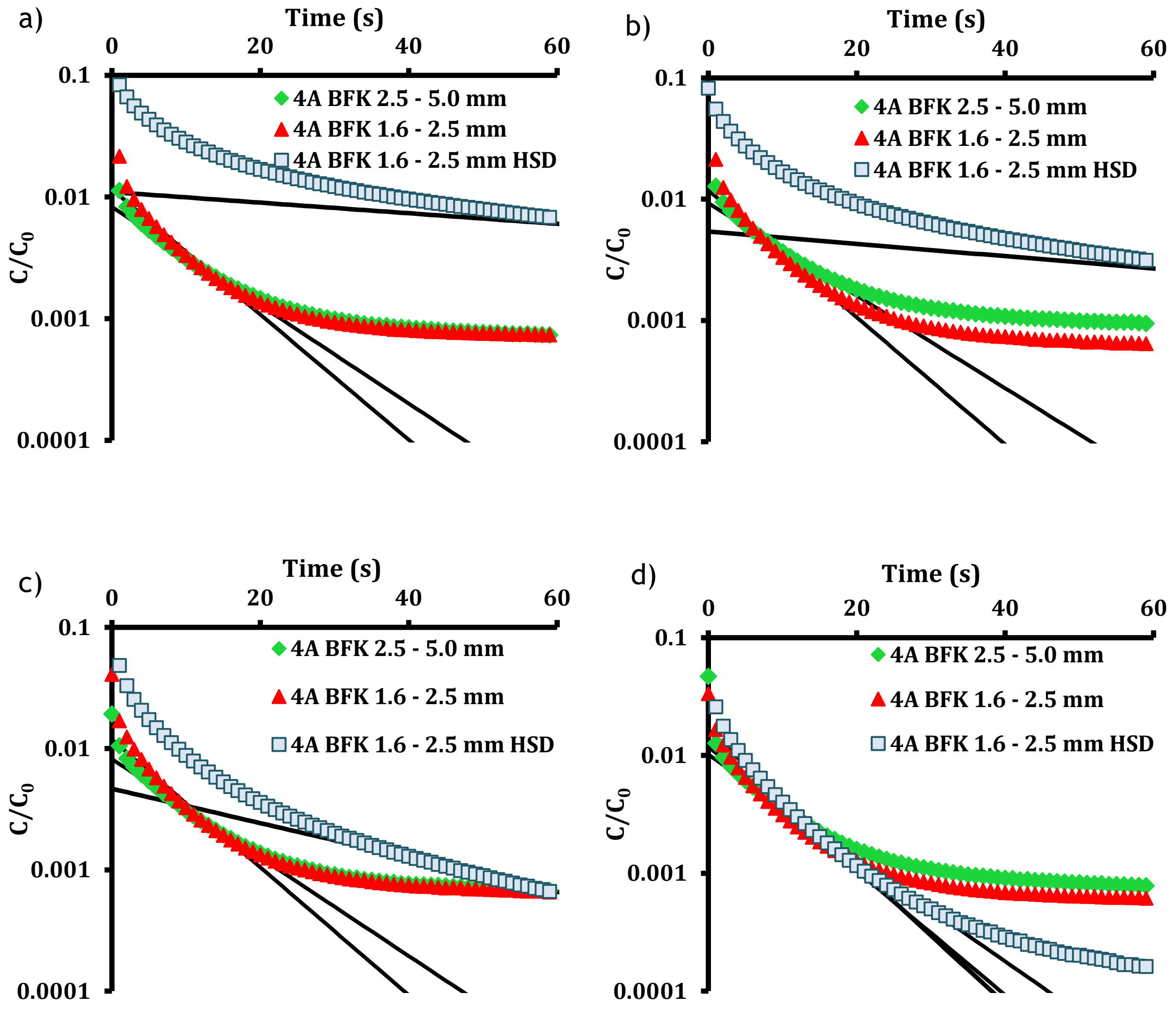

Figure A7.3- Experimental results and long-time response for CH_4 in different 4A BFK zeolites, at: a) 303 K and 6.58 x 10^{-7} m^3 s^{-1}, b) 323 K and 6.90 x 10^{-7} m^3 s^{-1}, c) 343 K and 9.83 x 10^{-7} m^3 s^{-1} and d) 373 K and 10.7 x 10^{-7} m^3 s^{-1}.

- Adsorbate: CH_4 in 13X zeolites

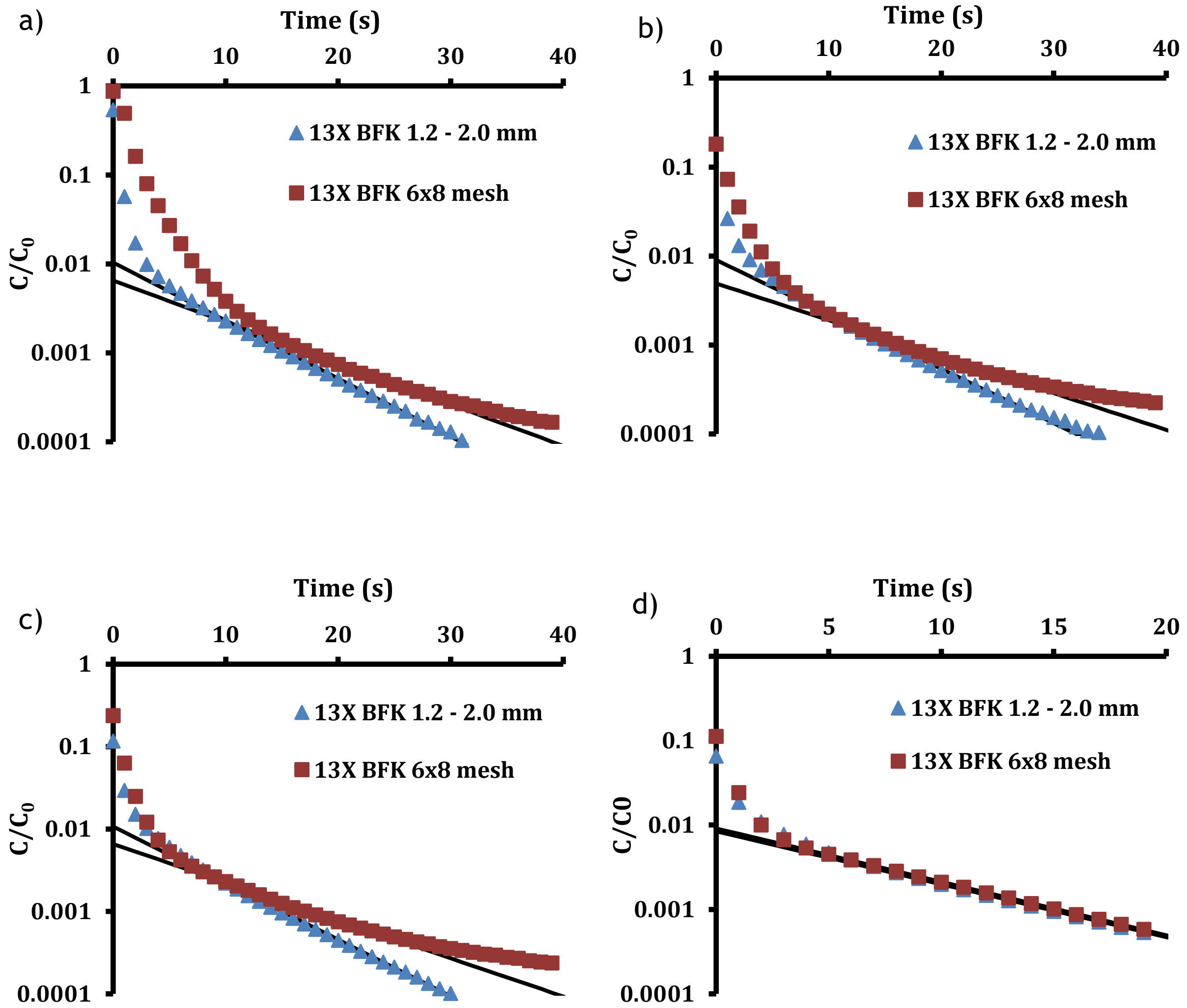

Figure A7.4 - Experimental results and long-time response for CH_4 in different 13X BFK zeolites, at: a) 303 K and 4.71 x 10^{-7} m^3 s^{-1}, b) 323 K and 8.08 x 10^{-7} m^3 s^{-1}, c) 343 K and 8.58 x 10^{-7} m^3 s^{-1} and d) 373 K and 10.7 x 10^{-7} m^3 s^{-1}.

Appendix 8 Henry constant determination

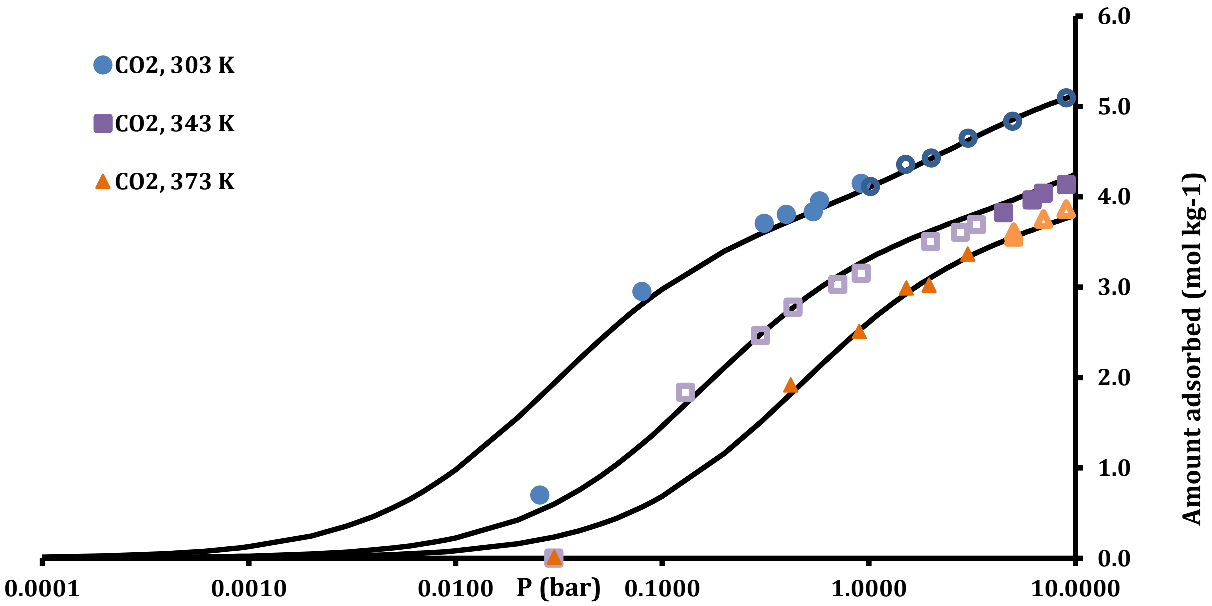

Figure A8.1- Amount of CO_2 adsorbed on 4A BFK 1.6-2.5 mm zeolite: experimental points (closed adsorption, open desorption) at 303, 343 and 373 K and the Langmuir Dual-site fiiting.

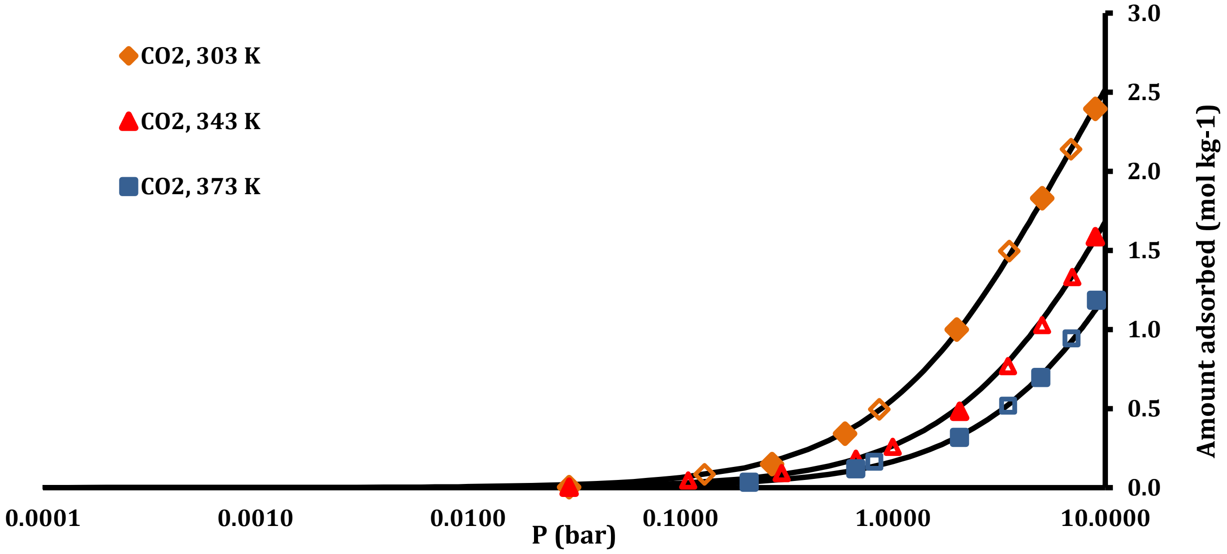

Figure A8.2- Amount of CH_4 adsorbed on 4A BFK 1.6-2.5 mm zeolite: experimental points (closed adsorption, open desorption) at 303, 343 and 373 K and the Langmuir fiiting.